ON THE THERMOELECTRIC EFFICIENCY OF WARPED ELECTRONIC BAND STRUCTURES: A COMPARISON OF THE PREDICTIONS OF COMMON SCATTERING APPROXIMATIONS

by

Cameron Rudderham

Submitted in partial fulfillment of the requirements
for the degree of Master of Science

at

Dalhousie University
Halifax, Nova Scotia
December 2019

This work is dedicated to my parents, Lori and Keith.

Table of Contents

List of Tables

List of Figures

Abstract

Within the linear response regime, calculation of a material's thermoelectric transport parameters requires detailed knowledge of both the electronic band structure and the electronic scattering rates. While it is possible to calculate both from first-principles using density-functional theory, rigorous scattering rate calculations can be orders of magnitude more intensive than band structure calculations, and so in practice it is common to make use of a simplified scattering model instead. The two most common such scattering models are the constant-mean-free-path model, the constant-relaxation-time model. However, recent studies in which the electronic scattering rates have been rigorously calculated have motivated the use of a third scattering approximation known as the DOS-scattering model, wherein the electronic scattering rates are assumed to have the same energy dependence as the density-of-states. While the latter approximation is believed to be the most physical of the three, it is also the least commonly used, despite being no more difficult to implement. The overall goal of this thesis is to understand the extent to which the predictions of the more commonly used scattering approximations differ from those of the more physical DOS-scattering model when applied to different classes of electronic band structure.

This work begins by comparing the predictions of these scattering models when applied to common analytic models of electronic dispersion. It is found that these models can differ significantly in their predictions, and can even disagree about whether a particular electronic dispersion feature should improve or degrade performance. In particular, we find that in the case of the so-called quartic-band model (a simple analytic model commonly used to describe warped bands), DOS scattering predicts the existence of a second local maximum in the thermoelectric power factor, a feature completely missed by both the constant-mean-free-path and constant-relaxation-time approximations. Motivated by these findings, we use first-principles calculations of electronic structure to investigate the thermoelectric properties of 2D quintuple-layered systems of Bi_2Te_3, Bi_2Se_3 and Sb_2Te_3 using the DOS scattering approximation. These materials display warped band structures qualitatively similar to those described by the quartic-band model, but have to date only been studied using the MFP and TAU approximations. To assist with the interpretation of our results, we introduce a new analytic model of electronic dispersion that qualitatively captures the main features of the band structures of these materials. It is found that while the presence of ring-like critical surfaces in the electronic dispersion can lead to excellent thermoelectric performance, such benefits are highly sensitive to the anistropy and energetic alignment of these features. Our findings suggest that these quintuple-layer systems may be even better thermoelectrics than was previously believed, and suggests the possibility of a new approach for designing band structures that lead to highly efficient thermoelectric conversion.

List of Abbreviations and Symbols Used

$D(E)$	Density-of-States Distribution.
$E[n]$	Ground State Energy Density-Functional.
E	Energy Level.
G	Reciprocal Lattice Vector.
I_j	j-th order Thermoelectric Moment Integral.
K_0	DOS-scattering parameter.
L	Length of sample (along transport direction).
$M(E)$	distribution-of-modes Distribution.
$S(E)$	Constant Energy Surface.
$S^+(E)$	Positive Velocity Surface.
S	Seebeck Coefficient.
T_C	Temperature of Cold Contact.
T_H	Temperature of Hot Contact.
T_i	Temperature of ith Contact.
T	Temperature.
$V_\lambda(E)$	Effective Electron Velocity.
W_j	j-th order Fermi Window Function.
ZT	Thermoelectric Figure of Merit.
Ω	Volume of Unit Cell.
Π	Peltier Coefficient.
$\Sigma(E)$	Transport Distribution.
$\Sigma_{DOS}(E)$	DOS-Scattering Transport Distribution.
$\Sigma_{MFP}(E)$	Constant-Mean-Free-Path Transport Distribution.
$\Sigma_{TAU}(E)$	Constant-Relaxation-Time Transport Distribution.
$\epsilon(k)$	Electronic Dispersion/Band Structure.
κ_0	Electrical Thermal Conductivity.

κ_e	Open-circuit Electrical Thermal Conductivity.
κ_l	Lattice Thermal Conductivity.
$\lambda(E)$	Mean Free Path Distribution.
λ_0	Constant mean-free-path parameter.
μ_i	Chemical Potential/Fermi Level at i-th Contact.
μ	Chemical Potential/Fermi Level.
σS^2	Thermoelectric Power Factor.
σ	Electrical Conductivity.
$\tau(E)$	Energy-dependent Relaxation Time.
$\tau(k)$	Wavevector-dependent Relaxation Time.
τ_0	Constant-relaxation-time parameter.
f_0	Fermi Dirac Distribution.
k_B	Boltzmann Constant.
m^*	Effective Mass Parameter.
m_0	Free Electron Mass.
$n(r)$	Charge Density Distribution.
q	Elementary Charge.
v_x	Electronic Group Velocity (along x-direction).
ADP	Acoustic Deformation Potential Scattering.
CBM	Conduction Band Minimum.
DFT	Density Functional Theory.
DOM	Distribution-of-Modes.
DOS	Density-of-States.
FDD	Fermi-Dirac Distribution.
GGA	Generalized Gradient Approximation.
LDA	Local Density Approximation.
MFP-model	Constant-Mean-Free-Path Scattering Approximation.
PBE	Perdew-Burke-Erzenhof Exchange-Correlation Functional.

QL	Quintuple-Layer.
TAU-model	Constant-Relaxation-Time Scattering Approximation.
VBM	Valence Band Maximum.

Acknowledgements

First and foremost, I would like to thank my supervisor Prof. Jesse Maassen for all the guidance he has provided to me over the last three years. From the day I started working on my honours research project with him, through to the end of my Masters program, Jesse has seemingly always been able to make time for any and all of my questions. His patience and continued support were absolutely invaluable to me over the course of my time at Dalhousie, and I am truly lucky to have been given the opportunity to learn from a researcher that prioritizes his students to the extent that Jesse does. I would also like to thank my fellow group members Vahid Askarpour and Patrick Strongman for answering so many of my questions (usually about Quantum Espresso), as well as Prof. Theodore Monchesky and Prof. Josef Zwanziger for agreeing to sit on my supervisory committee. Their suggestions and comments have been extremely helpful to me, and have significantly improved the quality of this thesis. I also acknowledge the financial support of the government of Nova Scotia and the National Science and Engineering Research Council, as well as Compute Canada for providing me with access to their computational resources.

For their roles outside of my research, I would also like to thank Prof. Kimberley Hall, Prof. Theodore Monchesky, Prof. Jesse Maassen and Dr. Stephen Payne for providing me with the opportunities to work for them as a teaching assistant. The experience I gained working for them, particularly the opportunities to give lectures and run tutorial sessions, have been invaluable to my development as a physicist. I have also benefitted greatly from the opportunity to participate in Stephen Payne's many outreach programs, especially the liquid nitrogen shows. I would be remiss to not thank our graduate coordinator Tanya Timmins as well, without whom I would almost certainly have missed numerous important deadlines or pieces of info. I do not think it is an exaggeration to say that Tanya has made the lives of every single physics student at Dalhousie significantly easier.

I am also indebted to the numerous occupants of Room 207 over the course of my time at Dalhousie, including (but not limited to) Patrick Strongman, Fouad

Kaadou, Chris Peacock, Karan Chowdhry, Andrey Zelenskiy, and David Kalliecharan. Whether it was acting as a sounding board for my less-than-fleshed-out ideas, or listening to me vent about whatever was stressing me out at the time, it cannot be overstated just how helpful it was (for both my research and my sanity) to have a group of friends to talk to over the course of my Masters program.

Lastly, and most importantly, I would like to thank my parents Lori and Keith, without whose unwavering love and support I could never have completed this project. Thank you for all that you have done, and continue to do for me. (I promise to visit the farm sometime soon...)

Chapter 1

Introduction

There has been a significant increase in the world-wide demand for energy in recent decades due to the ever-increasing human population, as well as increasing levels of industrialization, particularly in developing countries. This is problematic, as the majority of the world's energy still comes from the combustion of fossil fuels, which is well-known to have a massively detrimental impact on the environment. This problem is compounded by the inherent inefficiencies in our current energy production methods. For example, more than 60 percent of the energy produced in the United States is lost as waste heat [2], *i.e.* a significant portion of the energy produced is wasted heating things that do not require heating, such as the combustion engine of a car or electrical transformers. If even a fraction of this wasted heat could be recouped, we could significantly reduce the amount of fossil fuel combustion needed to meet the world's energy demands, and hence reduce the amount of greenhouse gas being produced.

Thermoelectric materials, which are materials capable of converting heat into useful electrical power, represent a promising method of recovering a portion of this wasted heat [3]. However, despite their success in numerous small-scale applications, the best thermoelectrics currently available are either too expensive, or too inefficient for widespread adoption to be economically viable. As such, the search for new, highly-efficient thermoelectric materials is an active field of research.

1.1 Thermoelectric Effects

1.1.1 Seebeck Effect

In 1794, Alessandro Volta discovered that when a temperature difference is applied across a junction of two dissimilar materials, a voltage difference is generated at the

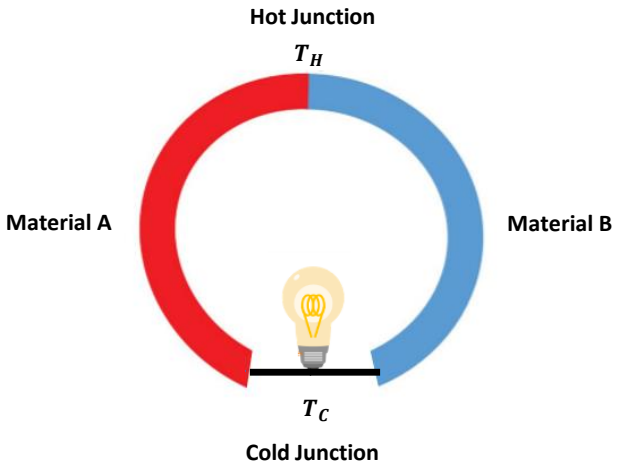

Figure 1.1: Schematic view of the Seebeck effect. Figure adapted from reference [1].

junctions. This effect is known as the Seebeck effect, after Thomas Johann Seebeck, who discovered the same effect independently in 1826 [4]. The strength of this effect is quantified by a quantity known as the Seebeck coefficient, S, which relates the magnitude of the applied temperature difference to the magnitude of the resulting voltage difference:

$$S = -\frac{\Delta V}{\Delta T}. \tag{1.1}$$

One can show that the Seebeck effect allows for the conversion of heat into electrical power. As such, solid-state materials exhibiting the Seebeck effect can be used in thermoelectric power generators, converting wasted heat from other systems back into useful electrical power (although there are numerous other factors that must be taken into account).

1.1.2 Peltier Effect

If one takes the same junction of two dissimilar materials, but instead applies a voltage difference, a temperature difference will be generated across the junction. This related effect is known as the Peltier effect, after its discoverer Jean Charles Athanase Peltier.

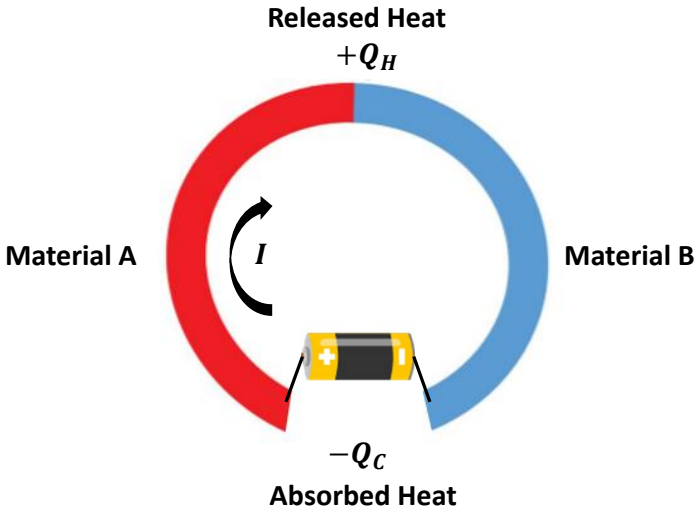

Figure 1.2: Schematic view of the Peltier effect. Figure adapted from reference [1].

It is most commonly quantified using the so-called Peltier coefficient, Π, which relates the electrical current, I to the resultant heat current, I_Q.

$$\frac{I_Q}{I} = \Pi \tag{1.2}$$

While the same electrical current, I flows through the entire circuit, the two dissimilar materials will in general have different Peltier coefficients, and hence there will a net release of heat ($+Q_H$) at one junction, and a net absorption of heat ($-Q_C$) at the other. Changing the direction of the electrical current will swap the behavior of the junctions, i.e will change heating to cooling and vice-versa. The Peltier effect can be thought of as the counterpart to the Seebeck effect, and the close relationship between these two effects is exemplified by the especially simple relationship between their respective coefficients,

$$\Pi = TS, \tag{1.3}$$

where the above identity is a special case of the more general Onsager reciprocal relations [5, 6].

1.2 Thermoelectric Figure-of-Merit

When exploiting the thermoelectric effects to generate electrical power from heat, it is desirable for the thermo-electric conversion taking place to be as efficient as possible. The maximum efficiency of a thermoelectric generator is given by [7]

$$\eta_{max} = \frac{\Delta T}{T_H} \frac{\sqrt{1+ZT}-1}{\sqrt{1+ZT}+\frac{T_C}{T_H}}, \tag{1.4}$$

where T_C and T_H are the temperatures at the cold and hot contacts respectively. It can be seen that this expression increases monotonically with the quantity ZT, approaching the Carnot limit as $ZT \to \infty$. This quantity, ZT, is known as the thermoelectric figure-of-merit, and is defined thusly:

$$ZT = \frac{\sigma S^2 T}{\kappa_e + \kappa_l}, \tag{1.5}$$

where σ is the electronic conductivity, S is the Seebeck coefficient, κ_e is the electronic contribution to the thermal conductivity (under open-circuit conditions), κ_l is the contribution to the thermal conductivity from the crystal lattice (*i.e.* phonons), and T is the temperature. The expression σS^2 that appears in the numerator of the expression for ZT is known as the thermoelectric power factor, and is commonly used as a metric for assessing the electronic properties of thermoelectric materials. All of the quantities defininining ZT are material specific (except for T), and as such ZT is a material property, and will take on different values in different materials. As more efficient thermoelectrics can recoup larger amounts of waste heat, discovering new materials with record high-ZT values is arguably the top priority for reseachers in the field.

1.3 Theoretical Calculations of Thermoelectric Properties

The thermoelectric parameters defining the figure-of-merit, ZT, are complicated functions of microscopic material properties, namely the electronic structure and the electronic scattering rates. These quantities are challenging to resolve experimentally, and even more challenging to tune, *e.g.* via alloying or nano-structuring of candidate thermoelectric materials. Furthermore, even when it is possible to successfully

engineer particular changes in the microscopic properties (*e.g.* in the band gap or effective masses), actually obtaining superior ZT values is highly non-trivial due to the complex interdependence of the quantities defining ZT. For example, while a high electrical conductivity, σ, is desirable for thermoelectric performance, enhancements to σ are typically accompanied by similar increases in the electrical thermal conductivity, κ_e, which degrades thermoelectric performance. A similar trade-off occurs when attempting to optimize the dopant concentration: changes that improve conductivity also tend to decrease the magnitude of the Seebeck coefficient, and vice-versa.

These challenges are further compounded by the difficulty (and cost) of producing high-quality material samples. Furthermore, since the thermoelectric performance of a material is also a function of the chemical potential level (which is controlled experimentally via the concentration of dopants), one must in principle prepare many samples with a range of different dopant concentrations in order to fully determine the potential thermoelectric performance of a particular material. For new materials, it may not even be obvious what the best dopant choices would be. In light of these challenges, experimental trial-and-error is a relatively inefficient means of searching for new thermoelectric materials with high figures-of-merit.

To combat the many challenges associated with experimental investigations of thermoelectric efficiency, it is common to make use of theoretical techniques to guide investigations. One such technique is the use of analytical models of electronic dispersion [8–11]. These analytical models allow one to directly explore the consequences of varying particular dispersion features (*e.g.* band gap, effective mass values, deviations from parabolicity, etc.) without the need to prepare samples that exhibit the desired features. The effect of dopant concentration can also be investigated (at least within the rigid band approximation), by simply changing the value of the chemical potential, μ. As such, analytical models allow one to quickly investigate the consequences of changing the values of various material parameters, something that if performed experimentally, would require a new sample to be prepared for each value being tested. These analytical models are commonly used to analyze experimental

results, or to provide design strategies [9, 10]

In addition to the benefits provided by analytic models of electronic dispersion, it is also possible to use density-functional theory calculations to rigorously resolve the electronic band structure [12–17] and electronic scattering rates [13,18–28] of a material, using only its crystal structure as input. This is particularly useful for materials with complex electronic dispersions not well-described by simple analytic models. While computationally intensive (particularly the scattering rate calculations), these first-principles investigations can nevertheless be performed much more quickly than most experimental investigations. As such, these first-principles techniques are commonly used to assess the viability of a particular thermoelectric material of interest, or to rapidly explore the thermoelectric properties of large numbers of candidate materials. The latter approach is particularly useful when searching for materials exhibiting dispersion features that analytical calculations have shown to be desirable for thermoelectric performance. The relative ease with which one is able to determine the thermoelectric properties of a material of interest, or to search for new materials exhibiting desirable features, makes theoretical calculations of thermoelectric properties an invaluable tool to researchers in the field of thermoelectrics.

1.4 Present Research and Motivation

As outlined above, first-principles calculations of electronic band structure and the electron-phonon scattering rates allow researchers to accurately determine the values of the material parameters defining ZT, making it possible to determine the viability of a particular material without the need for expensive and time-consuming experimentation. However, as rigorous scattering calculations can be extremely computationally intensive, a much more common approach is to pair rigorous calculations of electronic band structure with simplified models of carrier scattering, most often the constant-relaxation-time or constant-mean-free path approximations. As such, in recent years the focus has been primarily on researching the viability of particular electronic band structures, with less emphasis being placed on accurate descriptions of carrier scattering.

However, recent rigorous scattering-rate calculations have shown that the so-called DOS-scattering approximation, wherein the electron-phonon scattering rates are assumed to be proportional to the electronic density-of-states, describes the true scattering properties of many thermoelectric materials better than either the constant-mean-free-path or the constant-relaxation-time approximation [22, 27, 28]. As calculations of the electronic DOS are no more intensive than the calculations of electronic band structure that are commonly performed, the DOS-scattering model provides a means of obtaining a more accurate description of carrier scattering than either the constant-mean-free path or constant-relaxation-time approximations can provide, at essentially no additional computational cost. As such, this work sets out to understand the extent to which the predictions of the DOS-scattering model can differ from those of simpler scattering models. We note that the DOS-scattering model has been implemented in previous studies, and even compared against the predictions of simpler scattering approximations before [29], but such studies have until now been limited to relatively simple band structures. This work extends these previous investigations in two ways: firstly by providing the most detailed comparison of the predictions of common scattering approximations when applied to various common classes of band structure, and secondly by performing the first study that considers the consequences of DOS-scattering when applied to materials with highly-warped electronic band structures.

This work begins with a comparison of the predictions of these three scattering models when applied to analytic models of electronic dispersion, to determine to what extent the predictions of the more commonly used MFP and TAU approximations differ from those of the more physical DOS-scattering approximation. We find that even in relatively simple models of electronic dispersion, the predictions of the various scattering models can differ significantly, and the models may even disagree about whether a particular electronic dispersion feature will improve or degrade thermoelectric performance. This qualitative disagreement is found to be especially pronounced in the case of warped valence bands, such as those described by the quartic-band model. These warped band structures possess a large number of so-called *critical points*, *i.e.* points where the gradient of the electronic dispersion vanishes, and been

proposed as candidates for highly efficient thermoelectric conversion. Our analysis revisits the thermoelectric properties of such dispersions, with a focus on the impact that a more accurate scattering approximation (i.e the DOS-scattering model) has on the predicted properties.

In light of our finding that the more common constant-mean-free path and constant-relaxation time approximations fail to accurately describe the impact that warped bands have on the scattering rate distributions, we proceed to investigate the thermoelectric properties of 2D quintuple-layered systems of the semiconductors Bi_2Se_3, Bi_2Te_3 and Sb_2Te_3. These materials have been shown by previous studies to possess highly warped valence band structures, which contain large numbers of critical points. However, all previous theoretical studies of the thermoelectric properties of these materials have limited themselves to either the constant-mean-free-path or constant-relaxation-time approximations, and as such have failed to properly account for the impact that their warped band structure has on the electronic scattering rates.

To this end, we perform the first investigation of these quintuple-layered systems that makes use of the DOS-scattering approximation. It is found that the warped valence bands of these materials possess critical surfaces (*i.e.* constant-energy surfaces containing large numbers of critical points) that cannot be described by existing analytic models of electronic dispersion, so we introduce a new simple model of dispersion capable of describing the impact of such features. It is found that when the impact that such features have on scattering rates is taken into account (via the DOS-scattering model), the ZT values of these materials can be even higher than what researchers making use of the more common scattering approximations have found. However, it is also found that the performance enhancements predicted by the DOS scattering model are highly sensitive to the level of anisotropy in the electronic dispersions, as well as to the alignment of the critical surfaces.

Chapter 2

Theory and Methods

In this chapter, we outline the theory needed to understand the analysis performed in the following chapters. After a brief review of the basics of electronic band structure, thermoelectric transport, and density-functional theory, we outline the methodology we use to calculate quantities of interest from electronic dispersion data, both analytically and numerically.

2.1 Electronic Band Structure

Thermoelectric materials are typically crystalline, meaning that they are solid-state materials that possess discrete translational symmetry. As such, electrons in these thermoelectric materials experience a periodic potential that arises from the crystalline arrangment of the atomic nuclei. As proved by Felix Bloch [30], the wavefunction of any such electron must be of the form

$$\psi_k^\alpha(r) = e^{ik\cdot r} u_k^\alpha(r) \tag{2.1}$$

where k is a point in reciprocal space, α is the band index and $u_k^\alpha(r)$ is a function with the same perodicity as the unit cell of the material in question [31]. It can be shown that $\psi_k^\alpha(r)$ and $\psi_{k+G}^\alpha(r)$ (where G is a reciprocal lattice vector) are equivalent states, and so we can limit our calculations to k-points within the first Brillouin zone without loss of generality. In light of this, determining the allowed electronic energies of a solid-state system amounts to calculating the Bloch wavefunctions $\psi_k^\alpha(r)$ and the corresponding eigen-energies, E_k^α for each point k within the first Brillouin zone. Once calculated, one can define the dispersion relation of the material:

$$\epsilon(k) = \{E_k^\alpha\}. \tag{2.2}$$

This dispersion relation, also known as the band structure, is a multi-valued function which maps each point k in the Brillouin zone to the allowed eigenenergies of the corresponding Bloch wavefunctions. As we shall shortly see, the band structure is arguably *the* fundamental quantity for understanding the transport properties of thermoelectric materials.

2.2 Thermoelectric Transport

For a solid-state thermoelectric material in thermodynamic equilibrium, the probability of a state with energy E being occupied by an electron is given by the Fermi-Dirac distribution (FDD), which we denote with the symbol f_0,

$$f_0(E, \mu, T) = \frac{1}{e^{\frac{E-\mu}{k_B T}} + 1}, \tag{2.3}$$

where k_B is the Boltzmann constant, μ is the chemical potential of the system and T is the temperature. If there exists a small temperature or potential difference across the material, then the populations of electronic energy levels may vary across the material. Let f_1 be the FDD of injected carriers from the left contact, and let f_2 be the FDD of carriers at the right contact. Any difference between these two distributions describes a population imbalance, which will cause electrons to diffuse from the more populated side of the material to the other, as described by the following current equations [7] (valid in the linear response regime):

$$I = \frac{q}{L} \int_{-\infty}^{\infty} \Sigma(E)\big(f_1(E) - f_2(E)\big) dE, \tag{2.4}$$

$$I_Q = \frac{1}{L} \int_{-\infty}^{\infty} (E - \mu)\Sigma(E)\big(f_1(E) - f_2(E)\big) dE. \tag{2.5}$$

In the above equations, L is the length of the system along the transport direction. The quantity $\Sigma(E)$ is known as the *transport distribution*, and it quantifies the extent to which a particular energy level is able to contribute to electron transport. In the linear response regime, *i.e.* when the temperature and chemical potential differences are small, we can expand our current equations to first order in $\Delta T = T_1 - T_2$ and $\Delta\mu = \mu_1 - \mu_2$ (or equivalently, $\Delta V = \Delta\mu/q$, where q is the magnitude of the elementary charge), where T_i and μ_i are the temperature and chemical potential appearing in f_i.

$$I = \sigma \Delta V + \sigma S \Delta T \tag{2.6}$$

$$I_Q = \sigma S T \Delta V + \kappa_0 \Delta T \tag{2.7}$$

where we have introduced the electrical conductivity, σ, the Seebeck coefficient, S, and the electronic thermal conductivity, κ_0. Their definitions are as follows [32]:

$$\sigma = \big(\frac{2q^2}{h}\big) I_0, \tag{2.8}$$

$$S = -\big(\frac{k_B}{q}\big) \frac{I_1}{I_0}, \tag{2.9}$$

$$\kappa_0 = \big(\frac{2k_B^2 T}{h}\big) I_2, \tag{2.10}$$

where we have introduction the thermoelectric moment integral I_j:

$$I_j = \frac{h}{2L} \int_{-\infty}^{\infty} \Sigma(E) \big(\frac{E-\mu}{k_B T}\big)^j \big[-\frac{\partial f_0}{\partial E} \big] dE. \tag{2.11}$$

Note that the expression for ZT provided in the Introduction depends not on κ_0, but on the related *open-circuit* electronic thermal conductivity, κ_e. The definition for the latter is obtained by expressing ΔV in terms of ΔT using Equation 2.6, inserting that expression into Equation 2.7, then imposing the open-circuit condition $I = 0$.

$$\kappa_e = \kappa_0 - T\sigma S^2 = \big(\frac{2k_B^2 T}{h}\big)\big(I_2 - \frac{I_1^2}{I_0}\big) \tag{2.12}$$

As such, if one has an expression for the transport distribution of a given material, one can calculate all quantities of interest, and hence determine the thermoelectric efficiency of the material.

When implementing the relaxation time approximation within the Boltzmann transport formalism, and assuming transport along the $\hat{x}$ direction, the transport distribution is defined as [32]

$$\Sigma(E) = \frac{1}{\Omega} \sum_{k,\sigma,n} v_x^2(k) \tau(k) \delta(E - \epsilon(k)), \tag{2.13}$$

where Ω is the volume of the unit cell, $v_x = \frac{1}{\hbar}\frac{\partial \epsilon}{\partial k_x}$ is the x-component of the electronic group velocity, $\tau(k)$ is the relaxation time, and n is the band index. (In what follows, all sums over k should be understood to implicitly include a sum over band index as well) Although this form is not especially easy to interpret, there exists an alternative (but equivalent) transport formalism known as the Landauer formalism, within which the transport distribution takes on a more physically transparent form.

2.3 Landauer Formalism

Within the Landauer formalism, the transport distribution is commonly expressed as the product of two functions [7], as shown in the following expression:

$$\Sigma(E) = \frac{2}{h} M(E)\lambda(E) \tag{2.14}$$

The first quantity, $M(E)$, is known as the distribution-of-modes (or DOM), and is defined thusly [33]

$$M(E) = \frac{h}{4} \sum_{k,s} |v_x(k)|\, \delta(E - \epsilon(k)) \,/\, \Omega, \tag{2.15}$$

where the sum is performed over all spin states, s, and points in the Brillouin zone, k. As a consequence of this, the dimensions of $M(E)$ are a function of the dimension of the Brillouin zone, *i.e.* the units of $M(E)$ are different for 1D, 2D and 3D materials. In 1D, the DOM is a unitless quantity, whereas in 2D and 3D it is defined per unit length and per unit area, respectively.

Although not evident from the above definition, $M(E)$ can be shown to be equal to the number of states with energy E for which the component of the group velocity along the transport direction is positive. As such, it can be interpreted physically as the number of 'channels' available for electrons to travel in, and takes on integer values. This concept is illustrated for a one-dimensional band structure in Figure 2.1, although this interpretation holds for 2D and 3D materials as well, as shown in Appendix 6.2.

The second quantity, $\lambda(E)$, is known as the mean-free-path for backscattering, and is defined as the average distance that an electron with energy E will travel before a

scattering event changes the sign of its v_x component, *i.e.* before it scatters backwards. The mean-free-path for backscattering is defined in the following manner [33],

$$\lambda(E) = 2\,\frac{\sum_{k,s} v_x^2(k)\,\tau(k)\,\delta(E-\epsilon(k))}{\sum_{k,s} |v_x(k)|\,\delta(E-\epsilon(k))}, \tag{2.16}$$

where the above definition is chosen so that the Landauer formalism reproduces the results of the Boltzmann Transport Equation when implementing a constant relaxation time approximation [32].

In cases where the relaxation time $\tau(k)$ is only a function of energy, *i.e.* $\tau(k) = \tau(\epsilon(k))$, we can write the mean-free-path for backscttering as the product of an energy-dependent relaxation time and an averaged velocity, $\lambda(E) = V_\lambda(E)\tau(E)$. The averaged velocity is defined as

$$V_\lambda(E) = 2\,\frac{\sum_{k,s} v_x^2(k)\,\delta(E-\epsilon(k))}{\sum_{k,s} |v_x(k)|\,\delta(E-\epsilon(k))}. \tag{2.17}$$

In such cases, the transport distribution can be expressed thusly:

$$\Sigma(E) = \frac{2}{h} M(E) V_\lambda(E) \tau(E). \tag{2.18}$$

This form provides a physically transparent interpretation of the transport distribution. The ability of an energy level to transport charge is determined by how many channels are available for transport, $M(E)$, the average velocity of electrons in these channels $V_\lambda(E)$, and the average time between backscattering events, $\tau(E)$. Since the group velocity is defined in terms of the electronic dispersion, $v_x(k) = \frac{1}{\hbar}\frac{\partial \epsilon}{\partial k_x}$, both $M(E)$ and $V_\lambda(E)$ are entirely determined by the band structure of the material in question.

The relaxation time distribution, however, requires additional information (*e.g.* phonon dispersions) to be calculated rigorously. Whereas essentially all first-principles calculations of thermoelectric properties will make use of density-functional theory to accurately resolve the electronic band structure of the material being investigated,

it is relatively rare for researchers to perform a rigorous calculation of the electron-phonon scattering rates, as these calculations can be more computationally intensive than band structure calculations by orders of magnitude. In place of a rigorous scattering rate calculation, it is typical to instead make use of a simplified scattering rate approximation. The two most common such approximations are the constant-mean-free-path approximation, and the constant-relaxation-time approximation.

In the constant-mean-free-path approximation, one makes the simplifying assumption that the mean-free-paths of all electronic energy levels lying within the Fermi window are constant. Although used much more broadly, this approximation can be justified physically in the special case of 3D parabolic bands with acoustic deformation potential scattering (ADP) [34]. Phonon scattering is often the dominant scattering process for materials at room temperature. When this approximation is made, the transport distribution $\Sigma_{MFP}(E)$ takes on the following simplified form,

$$\Sigma_{\mathrm{MFP}}(E) = \frac{2}{h} M(E) \cdot \lambda_0, \tag{2.19}$$

where we have introduced the MFP-model scattering constant λ_0. Analogously, in the constant-relaxation-time approximation, one assumes that the electronic scattering rates of the states lying within the Fermi window are constant. This approximation is in some sense less crude than the constant MFP approximation, as it incorporates information about the average electronic velocities into the transport distribution, but materials in which a constant relaxation-time can be justified physically (*e.g.* 2D parabolic band materials with ADP) are relatively rare compared to those in which a constant MFP assumption is reasonable. When the constant relaxation time approximation is made, the transport distribution $\Sigma_{TAU}(E)$ takes on the following form,

$$\Sigma_{\mathrm{TAU}}(E) = \frac{2}{h} M(E) \cdot V_\lambda(E) \cdot \tau_0, \tag{2.20}$$

where we have introduced the TAU-model scattering constant τ_0. While these two scattering rate approximations make up the bulk of first-principles thermoelectric calculations, there exists another less-common scattering rate approximation, known

as the DOS scattering approximation, that is arguably more physical than either the constant-MFP or constant relaxation-time models.

When implementing the DOS scattering approximation, one assumes that the scattering rate of electrons at a given energy level is proportional to the total electronic DOS at the same energy level. Equivalently, one assumes that the electronic relaxation time distribution is inversely proportional to the electronic DOS, $D(E)$, defined below.

$$D(E) = \frac{1}{\Omega} \sum_{k,s} \delta(E - \epsilon(k)). \tag{2.21}$$

DOS scattering can be justified in a number of different scenarios. In parabolic band materials, if one assumes that ADP scattering is the dominant scattering process, it can be shown that one obtains a scattering rate distribution proportional to the electronic DOS [34]. Furthermore, rigorous electron-phonon scattering rate calculations have shown that a DOS scattering approximation should better reproduce the true scattering rates than either the MFP or TAU approximations [22, 27]. DOS scattering can be thought of as the least crude of the three scattering approximations considered here, as in addition to incorporating information about the average electronic velocities, it also incorporates the effect that changes in the density-of-states have on the electronic scattering rates, something that the other two approximations are blind to. When this approximation is made, the transport distribution $\Sigma_{DOS}(E)$ takes on the following form (note that we choose to place our scattering constant K_0 in the numerator of our expression, whereas previous papers have placed it in the denominator):

$$\Sigma_{\mathrm{DOS}}(E) = \frac{2}{h} M(E) \cdot V_\lambda(E) \cdot [K_0 / D(E)]. \tag{2.22}$$

In each of these three scattering approximations, there remains a single undetermined constant. In practice, these could be determined via experimental measurements of σ, as outlined in Appendix B.

2.4 Analytical Models of Dispersion

When calculating the thermoelectric properties of a material using one of the three simple scattering approximations outlined above, all quantities of interest are purely functions of the electronic dispersion, $\epsilon(k)$, of the material in question. As such, by specifying an analytic expression for the band structure, it is possible to explicitly calculate all quantities of interest, namely $M(E)$, $V_\lambda(E)$ and $D(E)$.

To do so, it is useful to rewrite Equations 2.15, 2.17 and 2.21 in an alternative form more practical for analytical calculations. The basic idea is to rewrite the sums of delta functions as an integral over the constant energy surface(s) of $\epsilon(k)$, using the following delta function identity,

$$\sum_k f(k)\delta(E-\epsilon(k)) = \frac{1}{(2\pi)^d}\int_{S(E)} \frac{f(k)}{|\nabla\epsilon(k)|}dS, \tag{2.23}$$

where d is the dimension of the band structure, and $S(E)$ is the set of all points in reciprocal space for which $\epsilon(k) = E$. In this form, it is clear that points at which $\nabla\epsilon(\vec{k}) = 0$, the so-called *critical points*, will have a disproportionately large impact on the electronic properties of the material. In particular, when there exist constant energy surfaces consisting entirely of critical points, one can expect to see very sharp features in quantities like $M(E), D(E)$ and $V_\lambda(E)$.

For simple models of band structure, it is possible to explicitly parameterize these constant energy surfaces, allowing for a direct evaluation of the integrals. For example, the constant energy surfaces of 3D isotropic bandstructures are spheres in reciprocal space, and can thus be parameterized by spherical polar coordinates. In two-dimensional (2D) materials, which will make up the bulk of our analysis, the constant energy surfaces form 1D curves in reciprocal space. Such curves can be parameterized by a single parameter, and two smooth functions thereof, as shown below:

$$\begin{cases} k_x = x(\phi) \\ k_y = y(\phi) \\ \phi \in [a, b] \end{cases}$$

We choose to use the symbol ϕ as our parameter, as the circular constant energy surfaces that arise from 2D isotropic dispersions are naturally parameterized by the polar angle, but for more general constant energy surfaces the parameter need not have any direct physical significance. Once a suitable parameterization has been chosen, we can rewrite our surface integrals as integrals over our parameter domain thusly:

$$\frac{1}{(2\pi)^2}\int_{S(E)} \frac{f(k_x,k_y)}{|\nabla\epsilon(k_x,k_y)|}dS = \frac{1}{(2\pi)^2}\int_a^b \frac{f(x(\phi),y(\phi))}{|\nabla\epsilon(x(\phi),y(\phi))|}\sqrt{(\frac{dx}{d\phi})^2+(\frac{dy}{d\phi})^2}d\phi. \quad (2.24)$$

For ease of notation later on, we define the following function

$$Q(\phi) = \frac{1}{4\pi^2}\frac{\sqrt{(\frac{dx}{d\phi})^2+(\frac{dy}{d\phi})^2}}{|\nabla_k\epsilon(x(\phi),y(\phi))|}, \quad (2.25)$$

which allows us to rewrite our sums over delta functions in the following manner:

$$\sum_k f(k)\delta(E-\epsilon(k)) = \int_a^b f(x(\phi),y(\phi))Q(\phi)d\phi. \quad (2.26)$$

Note that Q is implicitly a function of energy level, as different values of E will result in different constant energy surfaces, and hence different parameterizations. In terms of this function, the total density-of-states is then given by

$$D(E) = \frac{2}{\Omega}\sum_k \delta(E-\epsilon(k)) = \frac{2}{\Omega}\int_a^b Q(\phi)d\phi. \quad (2.27)$$

$M(E)$ and $V_\lambda(E)$ can be expressed in a similar manner:

$$M(E) = \frac{2}{\Omega}\cdot\frac{h}{2}\sum_{k,v_x>0}|v_x(k)|\delta(E-\epsilon(k)) = \frac{2\pi\hbar}{\Omega}\int_{a'}^{b'} v_x(\phi)Q(\phi)d\phi, \quad (2.28)$$

$$V_\lambda(E) = 2\frac{\int_{a'}^{b'} v_x^2(\phi)Q(\phi)d\phi}{\int_{a'}^{b'} v_x(\phi)Q(\phi)d\phi}. \tag{2.29}$$

Note that in general the bounds of the integrals in the latter two expressions will be different than those in the density-of-states expression, as in these cases the integration should only include the points on the constant energy surface which correspond to positive velocity states, *i.e.* the integration should be performed over the positive velocity surface $S^+(E)$ (See Appendix A).

For the most commonly used simple models of electronic dispersion, the positive velocity surfaces are easily described in Cartesian coordinates. For example, the positive velocity surface of an isotropic parabolic band is simply the set of all points for which $k_x > 0$. The same is true for the special case of an anisotropic parabolic band whose ellipsoidal axes are exactly aligned with the standard Cartesian axes [28]. In special cases such as these, it is possible to calculate the quantities of interest without invoking the full mathematical machinery of the surface integral formulation outlined above.

The power of our approach is in its ability to handle more general cases, wherein the positive velocity surfaces are not so cleanly expressed, *e.g.* for an anisotropic parabolic band whose ellipsoidal axes are *arbitrarily* oriented. In Appendix D, we apply a 3D version of the above surface integral formalism to such a band, and derive an expression for $M(E)$ with explicit transport direction dependence, something that until now has been lacking from the Landauer literature.

2.5 Density Functional Theory

As shown in the previous sections, calculation of the thermoelectric properties of a material requires, at a minimum, detailed knowledge of the material's electronic dispersion. In theory, this can be obtained from first-principles by solving the Schrodinger equation for the material in question. Suppose that our solid state system consists of N electrons that reside in the electric potential field due to M atomic nuclei. The Hamiltonian for such a system is commonly expressed as the sum of two different

terms. The first is due to the Coulombic interaction between the electrons and the atomic nuclei. (Note that we are assuming atomic units). The so-called external potential, *i.e.* the potential due to the charges of the atomic nuclei, is given by

$$V_{ext}(r) = -\sum_{\alpha}^{M} \frac{Z_\alpha}{|r - r_\alpha|}, \tag{2.30}$$

where Z_α is the atomic number of the α-th nucleus, and r_α the corresponding location.

The second term, $\hat{F}$ is a combination of the kinetic energy and electron-electron interaction terms,

$$\hat{F} = -\frac{1}{2}\sum_{i}^{N} \nabla_i^2 + \frac{1}{2}\sum_{i}^{N}\sum_{j\neq i}^{N} \frac{1}{|r_i - r_j|}, \tag{2.31}$$

where r_i is the position of the i-th electron. The full Hamiltonian for our system is then given by

$$\hat{H} = \hat{F} + \sum_{i}^{N} V_{ext}(r_i) = -\frac{1}{2}\sum_{i}^{N} \nabla_i^2 + \frac{1}{2}\sum_{i}^{N}\sum_{j\neq i}^{N} \frac{1}{|r_i - r_j|} + \sum_{i}^{N} V_{ext}(r_i). \tag{2.32}$$

Note that the Hamiltonian is entirely determined by the external potential and the number of electrons, N. However, as this Hamiltonian describes a $3N$-dimensional partial-differential equation, actually solving for the wavefunctions is fiendishly difficult for all but the simplest of systems.

An alternative approach was provided by Hohenberg and Kohn in their seminal 1964 paper [35]. In it, the authors prove two extremely powerful theorems. The first states that *the external potential is a unique functional of the ground state electronic density*, $n(r)$. Since the density also determines the number of electrons in the system ($N = \int n(r) d^3r$), it therefore uniquely determines the entire Hamiltonian, and with it all properties of the system, including the ground-state many-body wavefunction, $|\Psi\rangle$. This means that it is possible to uniquely define the so-called universal functional $F[n] = \langle\Psi|\hat{F}|\Psi\rangle$ (though obtaining an explicit expression for it is another matter entirely). In terms of this universal functional $F[n]$, we can write down an expression for the ground state energy density-functional, $E[n]$:

$$E[n] = F[n] + \int V_{ext}(r) n(r) d^3r \tag{2.33}$$

The second HK-theorem shows that this functional is variational in $n(r)$, *i.e.* that $E[n]$ *takes on its minimum value when* n *is the ground state density corresponding to the external potential* $V_{ext}(r)$.

Combined, these theorems reduce the problem of determining the many-body wavefunction to the considerably simpler problem of minimizing a three-dimensional functional, which represents a massive reduction of the complexity of the problem. The remaining challenge is obtaining an explicit form for $E[n]$, as the HK theorems only prove that such a functional *exists*.

As a first step, we can express our ground state energy functional thusly (note that we have switched from chemical to physical units):

$$\begin{aligned} E[n] = \underbrace{T[n]}_{\text{kinetic energy}} &+ \underbrace{\frac{e^2}{2 \cdot 4\pi\epsilon_0} \int d^3r \; d^3r' \; \frac{n(r)n(r')}{|r - r'|}}_{\text{el-el electrostatic PE}} \\ &+ \underbrace{\int d^3r \; n(r) V_{ext}(r)}_{\text{el-ion electrostatic PE}} + \underbrace{E_{XC}[n]}_{\text{exchange-correlation energy}} \end{aligned} \tag{2.34}$$

However, in the absence of an explicit universal expression for either the kinetic energy of a system of interacting electrons, $T[n]$, or the exchange-correlation energy, $E_{XC}[n]$, we are at an impasse. The most common method of dealing with this uncertainty is Kohn-Sham theory [36], wherein we instead opt to describe a ficticious system of non-interacting electrons that generates the same charge density as the true system. If the (orthogonal) single-particle wavefunctions of the non-interacting Kohn-Sham electrons are given by $\phi_i(r)$, then the non-interacting density is given by

$$n(r) = \sum_i^N |\phi_i(r)|^2. \tag{2.35}$$

The kinetic energy of these ficticious non-interacting electrons is then given by

$$T_{KS} = -\frac{\hbar^2}{2m}\sum_i^N \langle\phi_i|\nabla^2|\phi_i\rangle\,. \tag{2.36}$$

Although typically a good approximation to the kinetic energy of the true, interacting electron system, the Kohn-Sham kinetic energy is not exact. In practice, the difference between the two kinetic energy expressions is swept into the definition of the exchange-correlation potential, *i.e.* we redefine our exchange-correlation term such that

$$E_{XC}[n] = T[n] - T_{KS}[n] + E_X[n] + E_C[n], \tag{2.37}$$

where $E_X[n]$ and $E_C[n]$ are the *true* exchange and correlation energy functionals respectively. Thus, we have swept all uncertainty about the functional form of our ground state energy functional $E[n]$ into our $E_{XC}[n]$ term. This term describes the impact of all many-body effects, but its exact form is not known. Since our energy functional is stationary with respect to variations of the Kohn-Sham orbitals, we have that

$$\frac{\delta E[n]}{\delta\phi_i(r)} - E_i\phi_i(r) = 0, \tag{2.38}$$

where we have inserted a Lagrange multiplier so that the orthonormality of the Kohn-Sham wavefunctions is preserved. Evaluating the functional derivatives on the LHS, we obtain the effective Schrodinger equation for our Kohn-Sham system, known as the Kohn-Sham equation:

$$\left(-\frac{\hbar^2\nabla^2}{2m} + \int d^3r'\ \frac{n(r)}{|r-r'|} + V_{ext}(r) + \frac{\delta E_{XC}[n]}{\delta n(r)}\right)\phi_i(r) = E_i\phi_i(r). \tag{2.39}$$

Thus, the interacting electron problem has been reduced to solving a single-particle Schrodinger equation. If the exact form of $E_{XC}[n]$ were known, we could obtain the exact ground state density of the interacting system. In practice, approximate forms such as the local-density approximation (LDA) or generalized-gradient-approximation functional (GGA) must be used, but these are usually good enough to calculate quantities of interest to the desired degree of accuracy. In our case, the Kohn-Sham equations make it possible for us to solve for the band structure, $\epsilon(k)$ of our system,

i.e. to calculate the Bloch eigenenergies for each k-point in our Brillouin zone. As with any numerical calculation, this results in a band structure that is resolved discretely (*i.e.* on a grid of finitely many k-points) rather than continuously, which necessitates a different approach for calculating quantites like $D(E)$, $M(E)$ and $V_\lambda(E)$.

2.6 Numerical Methods

When one can only resolve the electronic band structure discretely, *e.g.* when one performs a density-functional theory (DFT) calculation to obtain the electronic structure of a material, a different calculational approach must be used to obtain $D(E)$, $M(E)$ and $V_\lambda(E)$. The simplest of these to obtain is typically the density-of-states: most DFT packages are capable of calculating $D(E)$ directly, often by using a tetrahedron integration technique to integrate over the Brillouin zone [37]. For the latter two quantities, a slightly more sophisticated technique must be used.

If the electronic dispersion of a material is resolved on a uniform Cartesian grid, there exists an elegant numerical algorithm for the calculation of $M(E)$ and $V_\lambda(E)$ known as *band-counting* [38]. It can be shown that the distribution-of-modes, $M(E)$, is simply equal to the number of states at energy E for which $v_x > 0$, as illustrated in Figure 2.1. Similarily, $V_\lambda(E)$ is simply (twice) the average velocity of these same states. As such, both quantities can quickly be calculated from the electronic dispersion data output by a DFT calculation [38].

While the majority of materials do not possess the rectangular Brillouin zones necessary for band-counting, it is always possible to 'fold' the primitive Brillouin zone into a smaller, rectangular Brillouin zone, such that the band-counting algorithm can be applied. This technique is equivalent to performing the electronic structure calculation using a larger, rectangular super-cell (which would result in a smaller, rectangular Brillouin zone), but one can avoid the additional computational cost associated with super-cell calculations by instead performing the calculations on the primitive cell, then 'folding' points that lie outside of the rectangular BZ. Figure 2.2 illustrates how this folding would be performed for a 2D hexagonal material.

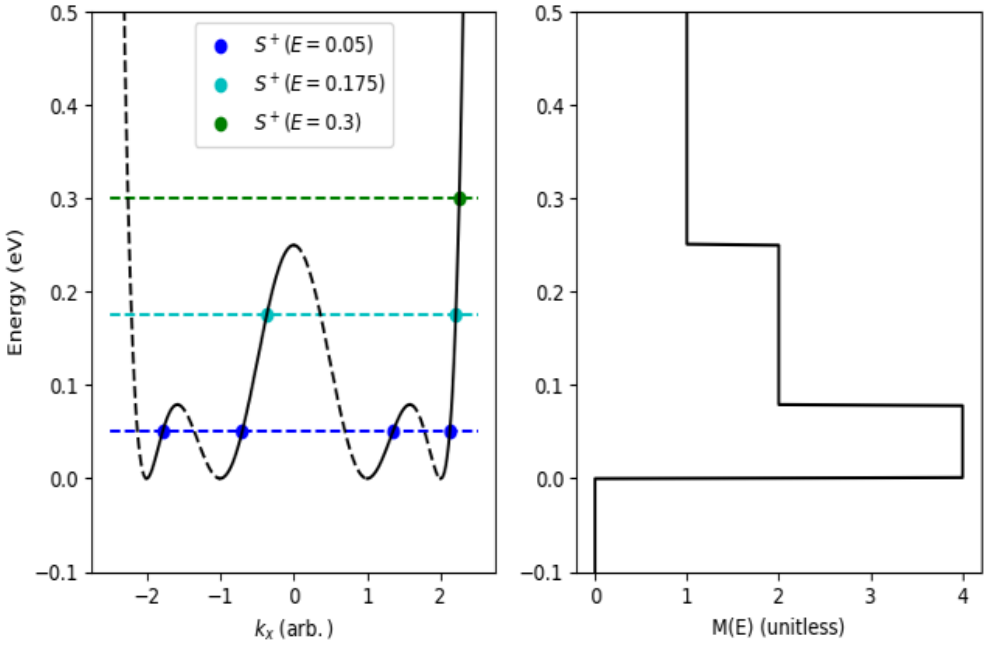

Figure 2.1: Illustration of the Landauer band-counting algorithm for a 1D bandstructure. Positive velocity branches are plotted as solid black lines, negative velocity branches as dotted black lines. The expression $S^+(E)$ refers to the positive velocity surface, i.e the set of all k-points with energy E and positive velocity.

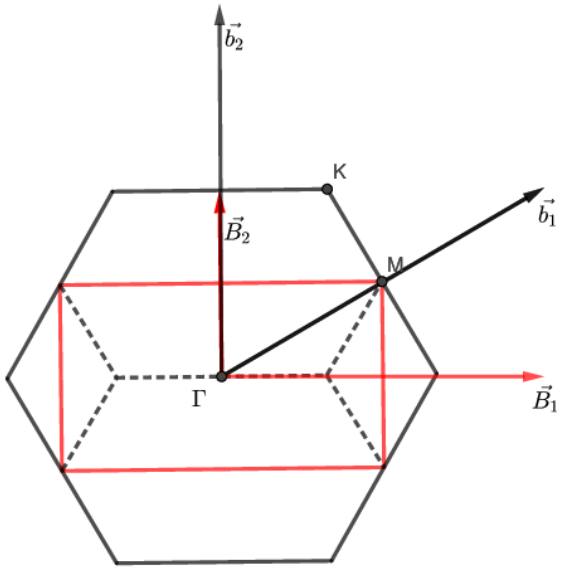

Figure 2.2: Diagram illustrating the implementation of the band-folding technique, as applied to the Brillouin zone of a 2D hexagonal material.

Using the reciprocal lattice vectors of the rectangular super-cell, it is possible to map each k-point in the primitive hexagonal BZ into a corresponding point within the rectangular BZ. This has the effect of turning a single band resolved over the hexagonal BZ to *two* bands resolved over the smaller recangular BZ. The continuity of the gradient of the electronic dispersion is preserved in the folded bands, as the folded regions are stitched together along the boundaries of the primitive BZ, with respect to which the gradient of the electronic dispersion must be normal [31]. The same general procedure can be applied to Brillouin zones with more complicated geometries, but the number of 'extra' bands may vary. For example, folding a rhombohedral BZ into a rectangular BZ results in six times as many bands.

We make use of a custom script to perform this folding procedure, and a software package by the name of LanTraP [38] to perform the calculations of $M(E)$ and $V_\lambda(E)$. As the number of k-points needed to accurately resolve transport properties can be very large, we do not resolve the entire Brillouin zone in a single calculation, instead opting to break up our non-self consistent calculations into hundreds of seperate jobs, each resolving a the electronic dispersion of a small portion of the Brillouin zone. The band-counting algorithm is well-known and widely used, particularily by researchers making use of the Landauer formalism of thermoelectric transport. However, it is difficult to track down a reference where this result is derived in full generality. To this end, we present in Appendix A what (to our knowledge) is the most rigorous and general derivation of the band counting algorithm in the literature.

Chapter 3

On the Thermoelectric Performance of Analytic Band Structure Models

In this chapter, we investigate how the thermoelectric parameters (particularily the power factor $PF = \sigma S^2$) calculated with the DOS-scattering compare to the predictions of the more commonly used constant-MFP and constant-relaxation time approximations, when applied to simple analytical models of electronic dispersion. The dispersions we consider are those of parabolic bands (1D/2D/3D), Kane bands (1D/2D/3D) and ring shaped bands (2D).

3.1 Parabolic Bands

We begin with perhaps the most familiar electron dispersion model – a single isotropic parabolic, effective mass band (see for example Refs. [8–11, 27]). The electron dispersion has the form:

$$E = \frac{\hbar^2 k^2}{2m^*}, \tag{3.1}$$

where m^* is the effective mass. The corresponding quantities $M(E)$, $V_\lambda(E)$ and $D(E)$ are shown in Figure 3.1. Using Eqns. (2.8)-(2.16), we calculate the TE properties. Figure 3.2 illustrates the power factors ($PF = S^2\sigma$) of parabolic band with $m^* = m_0$ (the free electron mass), calculated using all three scattering approximations in 1D, 2D and 3D. The results for the MFP model were previously shown in Ref. [39]. Note that the units of PF vary across dimensions – a direct comparison requires introducing an "effective cross-sectional area" for the low-dimensional materials. This effective area is a function of how densely the low-dimensional materials can be packed without distorting the electronic dispersion, which is highly material-dependent, so we do not attempt to define one for the models considered in this work. As discussed in the previous chapter, each of our three scattering models contains a free parameter. We set these parameters (namely λ_0, τ_0, and K_0) such that all three models predict

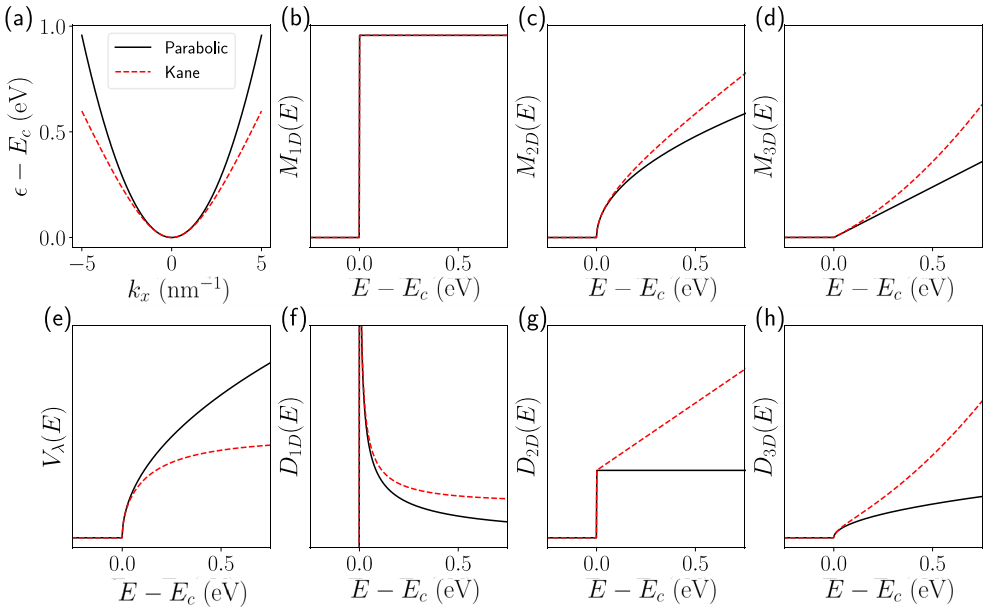

Figure 3.1: Parabolic and Kane bands in 1D, 2D and 3D ($m^* = m_0$, $\alpha = 1$ eV^{-1}). Sketches of (a) electron dispersion $E(k)$, (b,c,d) distribution-of-modes $M(E)$, (f,g,h) density-of-states $D(E)$, and (e) average velocity $V_\lambda(E)$ (see main text for definition). Parabolic band and Kane band results appear as black solid and dashed red lines, respectively.

the same electrical conductivity when the Fermi level lies at the conduction band edge, E_C. This is equivalent to fixing the average mean-free-path for backscattering, $\langle\langle\lambda\rangle\rangle_{\mu=E_C}$, which is defined thusly:

$$\langle\langle\lambda\rangle\rangle_{\mu=E_C} = \frac{\int \lambda(E) M(E) \left(-\frac{\partial f_0}{\partial E}\right)_{\mu=E_C} dE}{\int M(E) \left(-\frac{\partial f_0}{\partial E}\right)_{\mu=E_C} dE}. \tag{3.2}$$

For all three scattering models, we set our free parameters such that $\langle\langle\lambda\rangle\rangle_{\mu=E_C} = 10$ nm, a typical value.

We focus first on the one-dimensional case. It is noteworthy that despite being made to agree about the electronic conductivity (when $\mu = E_C$), the DOS model predicts a power factor more than 50% higher than that of the TAU model, which in turn is larger than that of the MFP model. As shown in Figure 3.3, we can see that the DOS scattering model predicts a larger electrical conductivity for all Fermi levels lying within the band, as well as a larger Seebeck coefficient.

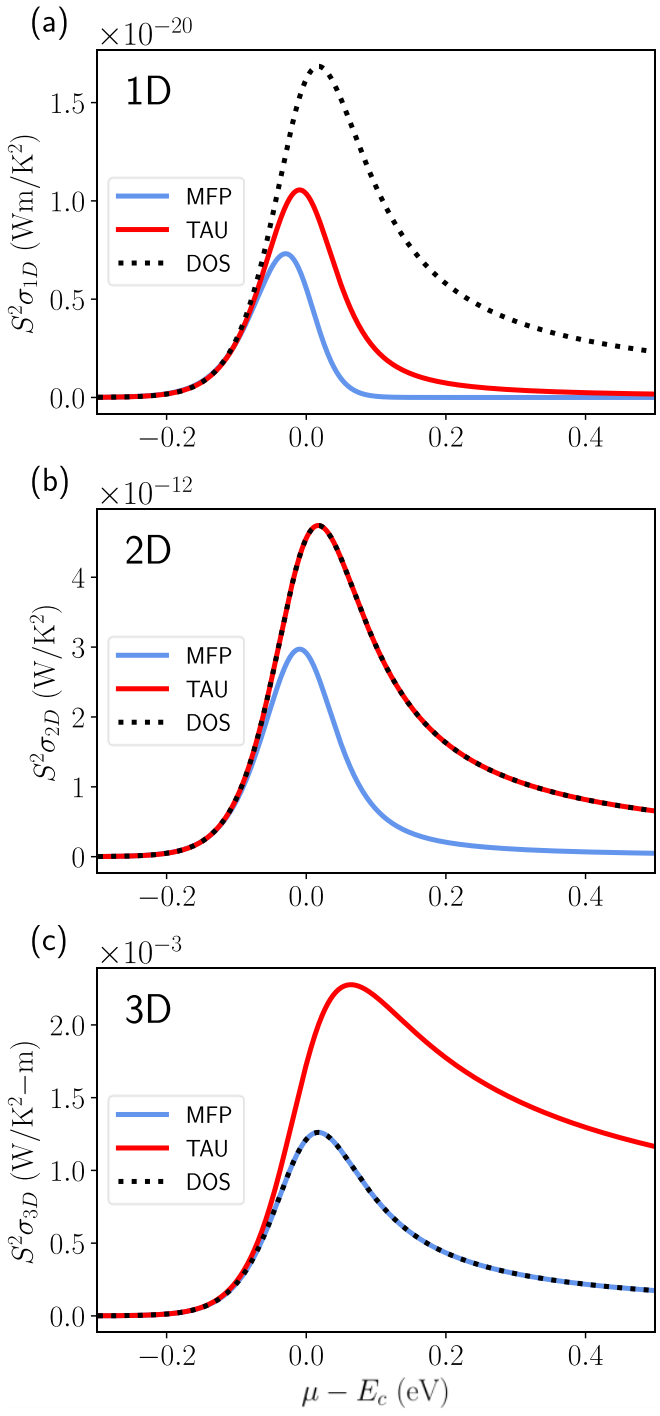

Figure 3.2: Isotropic parabolic band. Power factor PF versus Fermi level μ in (a) 1D, (b) 2D, and (c) 3D, using the MFP, TAU and DOS scattering models. For these calculations, $m^* = m_0$, $T = 300$ K, and $\langle\langle\lambda\rangle\rangle_{\mu=E_C} = 10$ nm.

Dimension/Quantity	$M(E)$	$V_\lambda(E)$	$D(E)$	$\Sigma_{\text{MFP}}(E)$	$\Sigma_{\text{TAU}}(E)$	$\Sigma_{\text{DOS}}(E)$
1D	1	$\sqrt{E}$	$1/\sqrt{E}$	1	$\sqrt{E}$	E
2D	$\sqrt{E}$	$\sqrt{E}$	1	$\sqrt{E}$	E	E
3D	E	$\sqrt{E}$	$\sqrt{E}$	E	$E^{3/2}$	E

Table 3.1: Isotropic parabolic band in 1D, 2D and 3D. Energy dependence of distribution-of-modes $M(E)$, average velocity $V_\lambda(E)$, density-of-states $D(E)$, and transport distribution $\Sigma(E)$ (within the MFP, TAU and DOS scattering models). For full expressions, refer to Appendix E.1.

This increased performance comes from the fact that the DOS for a 1D parabolic band is a decreasing function with respect to energy ($1/\sqrt{E}$). This results in the DOS model predicting a lower scattering rate for high-energy electrons, which results in improved performance. In the two-dimensional case, the predictions of the DOS model and the TAU model are identical. This is because the DOS of a 2D parabolic band is constant, which results in a constant scattering time in the DOS model. The MFP model again predicts the worst performance of the three. In the three-dimensional case, it is now the MFP model that agrees with the DOS model. This occurs because in 3D, $V_\lambda(E)$ and $D(E)$ have the same energy dependence, namely $\sqrt{E}$, so their contributions to $\lambda_{\text{DOS}}(E) = K_0 V_\lambda(E)/D(E)$ cancel out leaving a constant.

When comparing the magnitude of the power factors to the energy dependence of the corresponding transport distributions (shown in Table 3.1), it is clear that both are correlated: a $\Sigma(E)$ with stronger energy dependence results in a larger maximum PF. To illustrate why this happens, we introduce the Fermi window function. From Eqns. (2.8)-(2.9), we see that $\sigma \propto I_0$ and $S \propto I_1$, thus it is convenient to define the following function, W_j:

$$W_j(E,\mu) = \left(\frac{E-\mu}{k_B T}\right)^j \left[-\frac{\partial f_0(E,\mu)}{\partial E}\right], \tag{3.3}$$

referred to as the Fermi window function of j^{th} order, which appears in the integrand of I_j (Eq. 2.11). One can show that $\int_{-\infty}^{\infty} W_0\, dE = 1$ and $\int_{-\infty}^{\infty} W_1\, dE = 0$. Since the Fermi window functions are not material specific, the TE quantities are determined by the transport distribution, $\Sigma(E) = \frac{2}{h} M(E)\lambda(E)$.

Figure 3.4 presents $\lambda(E)$ versus energy for the MFP and DOS scattering models,

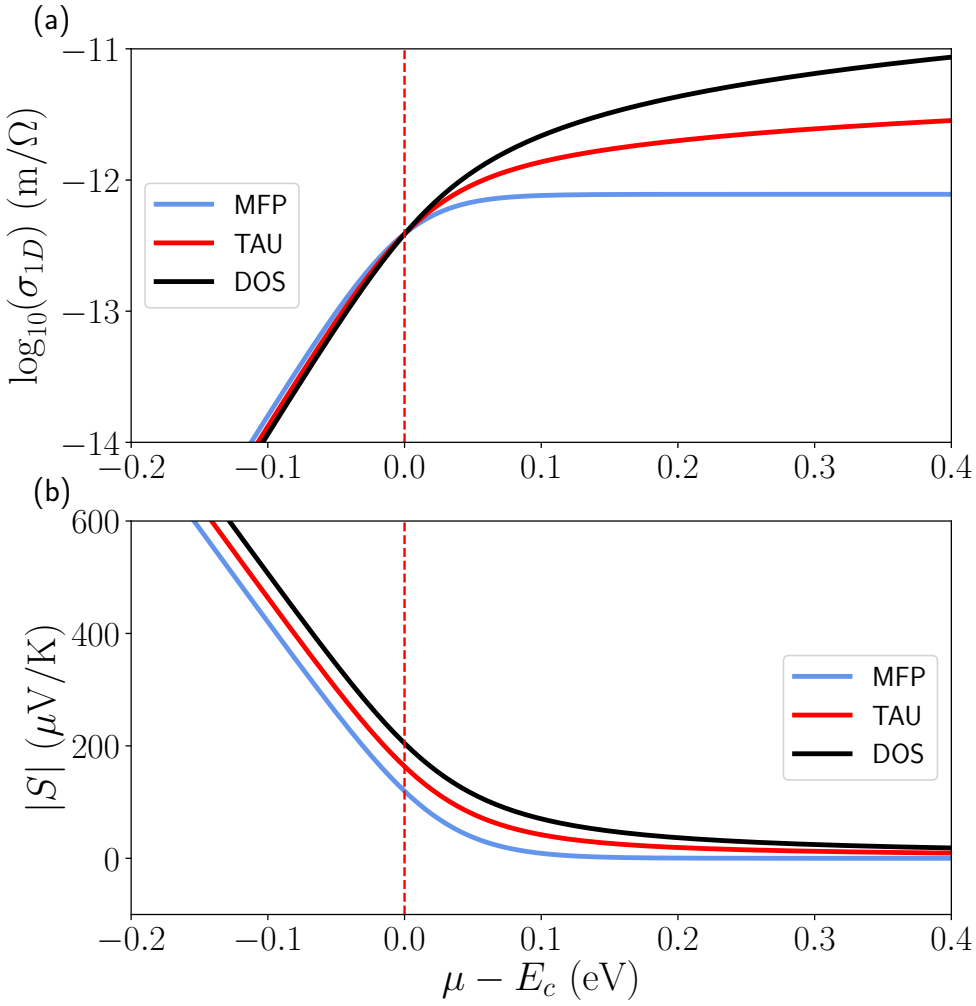

Figure 3.3: Isotropic parabolic band. (a) Electrical conductivity and (b) Seebeck coefficient for a 1D parabolic band, using the MFP, TAU and DOS scattering models. For these calculations, $m^* = m_0$, $T = 300$ K, and $\langle\langle\lambda\rangle\rangle_{\mu=E_C} = 10$ nm. The band edge, E_C, is indicated with a vertical red line.

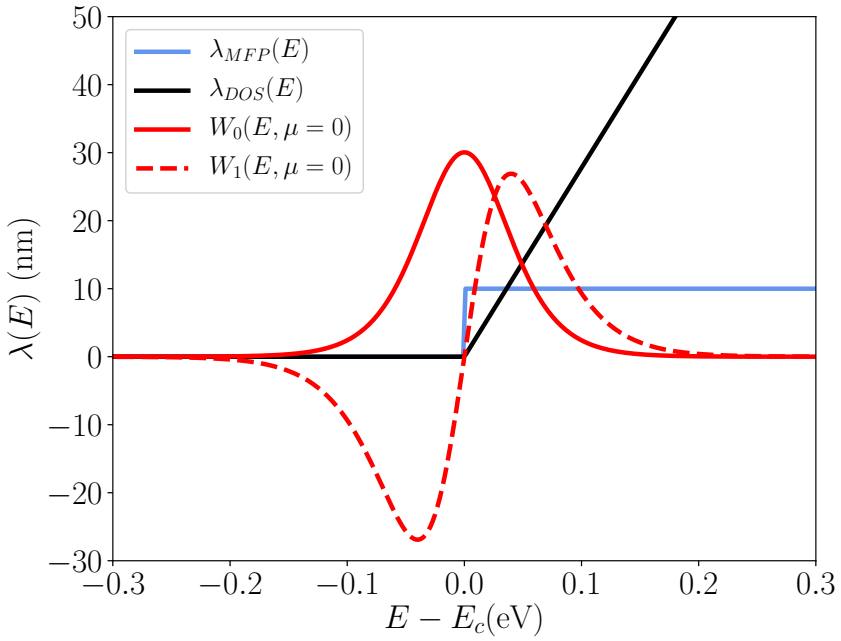

Figure 3.4: 1D isotropic parabolic band. Mean-free-path for backscattering versus energy for the MFP and DOS models. Also shown are the 0^{th}- and 1^{st}-order Fermi windows (see text for their definition). For these calculations, $\mu = E_C$, $m^* = m_0$, $T = 300$ K, and $\langle\langle\lambda\rangle\rangle = 10$ nm.

in the case of 1D parabolic band. When comparing different scattering models only $\lambda(E)$ is altered while $M(E)$ remains constant. Also plotted are the 0^{th}- and 1^{st}-order Fermi windows, $W_{0,1}(E)$ (not to scale). Both models have the same average mean-free-path for backscattering (and σ), which is related to the product of $\lambda(E)$ and $W_0(E)$. Note, however, that the Seebeck coefficient depends on $\lambda(E)$ times $W_1(E)$ – compared to $W_0(E)$, $W_1(E)$ extends further in energy. Thus, the $\lambda(E)$, or $\Sigma(E)$, with larger energy dependence will yield a larger Seebeck coefficient and power factor. In this case, $\lambda_{\text{MFP}} \propto E^0$ and $\lambda_{\text{DOS}} \propto E^1$, leading to $S_{\text{DOS}} > S_{\text{MFP}}$ which explains the trend in Fig. 3.2. From this observation follows a noteworthy corollary: when made to agree about $\langle\langle\lambda\rangle\rangle$ in a semiconducting material, *a TAU scattering model will always be more optimistic about thermoelectric performance than an MFP scattering model*.

While $\Sigma_{\text{MFP}}(E)$ is simply proportional to $M(E)$, $\Sigma_{\text{TAU}}(E)$ is proportional to $M(E)\,V_\lambda(E)$ (see Eqns. (2.19)-(2.20)). The latter will *always* go to zero at the band edge of a semiconductor, since the band edge corresponds to a local minimum in the electronic dispersion in k-space, and hence has vanishing velocity. As such, $V_\lambda(E)$ will always be an increasing quantity, at least for low energies. (This may not be the case for metals, or materials with linear bands such as graphene or topological insulators, which have been proposed as good thermoelectrics [40].) This means that, with semiconductors, $\Sigma_{\text{TAU}}(E)$ is generally expected to exhibit a larger energy-dependence than $\Sigma_{\text{MFP}}(E)$, and hence predict better TE performance.

This observation has important consequences when comparing the predictions based on the constant relaxation-time approximation (*i.e.* TAU model), often adopted with a Boltzmann approach, versus those based on the a constant mean-free-path approximation (*i.e.* MFP model), commonly adopted with a Landauer approach. Even when in complete agreement about the electronic dispersion and electrical conductivity of a particular material, the TAU scattering model will inevitably draw more optimistic conclusions than the MFP model. No such general trend exists when comparing to a DOS scattering model, whose predicted performance can vary from being the greatest of the three models to being the worst depending on the details of the

Dimension	$M(E)$	$V_\lambda(E)$	$D(E)$	$\Sigma_{\text{MFP}}(E)$	$\Sigma_{\text{TAU}}(E)$	$\Sigma_{\text{DOS}}(E)$
1D	1	$\frac{\sqrt{E(1+\alpha E)}}{1+2\alpha E}$	$\frac{1+2\alpha E}{\sqrt{E(1+\alpha E)}}$	1	$\frac{\sqrt{E(1+\alpha E)}}{1+2\alpha E}$	$\frac{E(1+\alpha E)}{(1+2\alpha E)^2}$
2D	$\sqrt{E(1+\alpha E)}$	$\frac{\sqrt{E(1+\alpha E)}}{1+2\alpha E}$	$1+2\alpha E$	$\sqrt{E(1+\alpha E)}$	$\frac{E(1+\alpha E)}{1+2\alpha E}$	$\frac{E(1+\alpha E)}{(1+2\alpha E)^2}$
3D	$E(1+\alpha E)$	$\frac{\sqrt{E(1+\alpha E)}}{1+2\alpha E}$	$\sqrt{E(1+\alpha E)}(1+2\alpha E)$	$E(1+\alpha E)$	$\frac{[E(1+\alpha E)]^{3/2}}{1+2\alpha E}$	$\frac{E(1+\alpha E)}{(1+2\alpha E)^2}$

Table 3.2: Kane band in 1D, 2D and 3D. Energy dependence of distribution-of-modes $M(E)$, average velocity $V_\lambda(E)$, density-of-states $D(E)$, and transport distribution $\Sigma(E)$ (within the MFP, TAU and DOS scattering models). For the full expressions, refer to Appendix E.2.

dispersion, as shown for a parabolic band and to be confirmed with other dispersions below.

Our expressions for isotropic bands can be generalized to describe anisotropic parabolic bands as well, as shown in Appendix E.1. It is interesting to note that in the anisotropic case, the transport distributions of the three scattering models each have a different dependence on the components of the effective mass tensor: $\Sigma_{\text{MFP}} \propto \sqrt{m_y m_z}$, $\Sigma_{\text{TAU}} \propto \sqrt{m_y m_z / m_x}$, $\Sigma_{\text{DOS}} \propto 1/m_x$ (with transport assumed along x).

3.2 Kane Bands

In the previous section we showed that, with one of the simplest dispersion models, the predictions of the MFP and TAU models can differ appreciably from those of the DOS model. Next, we set out to investigate what each scattering model concludes about the effect of deviations from parabolicity. A widely applicable generalization of the parabolic band model is the Kane model, in which the electronic dispersion is modelled as

$$E(1+\alpha E) = \frac{\hbar^2 k^2}{2m^*}, \tag{3.4}$$

where in addition to the effective mass m^* there is the non-parabolicity parameter α. As illustrated in Fig. 3.1, the Kane model gives an electronic dispersion that is parabolic near the band edge, but approaches linearity at higher energies – α is a measure of how "linearized" the band is. This simple model can be derived from $k \cdot p$ theory, and in many cases is found to represent actual electronic band structures (*e.g.*

those obtained from DFT) more accurately than a pure parabolic band model [41].

Figure 3.5 compares the power factors of a Kane dispersion (in 1D, 2D and 3D) for the three scattering models. The parabolic band results (dashed lines) as also plotted to serve as a reference ($m^* = m_0$, and $\alpha = 1.0$ eV^{-1} for the Kane band, which is a typical value of α [41]). The changes in PF can be understood in terms of the effect that the "linearization" of dispersion has on $M(E)$, $D(E)$, and $V_\lambda(E)$, which are shown as dashed lines in Fig. 3.1.

Firstly, the MFP model consistently predicts improved performance when the parabolic band is 'linearized', meaning the PF increases with the Kane parameter α. This is because, at a given energy, a Kane band will have a larger $M(E)$ than a parabolic band with the same effective mass. (One exception is the 1D case, where $M(E)$ is a unit step function for both parabolic and Kane bands.) However, the TAU model predicts that linearization will result in worse thermoelectric performance in in 1D and 2D, but predicts improved performance in 3D. This difference comes from the fact that a Kane band is slower than its parabolic band equivalent (*i.e.* same m^*), thus reducing $V_\lambda(E)$ – a fact that the MFP model is blind to. In 3D, $M(E)$ increases by enough to offset the detrimental effects of lower velocity electrons, but in lower dimensions this is no longer the case.

DOS scattering, however, is consistent in its prediction that linearization results in decreased performance. This occurs since, in addition to the lower velocity, the increased DOS results in more scattering – something that the other two scattering models are blind to. This combination of slower states and increased scattering is enough to outweigh the performance benefits of an increased number of conducting channels, regardless of spatial dimension.

While none of the scattering models predict especially favorable TE performance from a Kane band, it is nonetheless noteworthy that the simplified MFP and TAU model approximations can occasionally draw the exact opposite conclusion of the more physical DOS scattering model, namely that deviations from parabolicity can

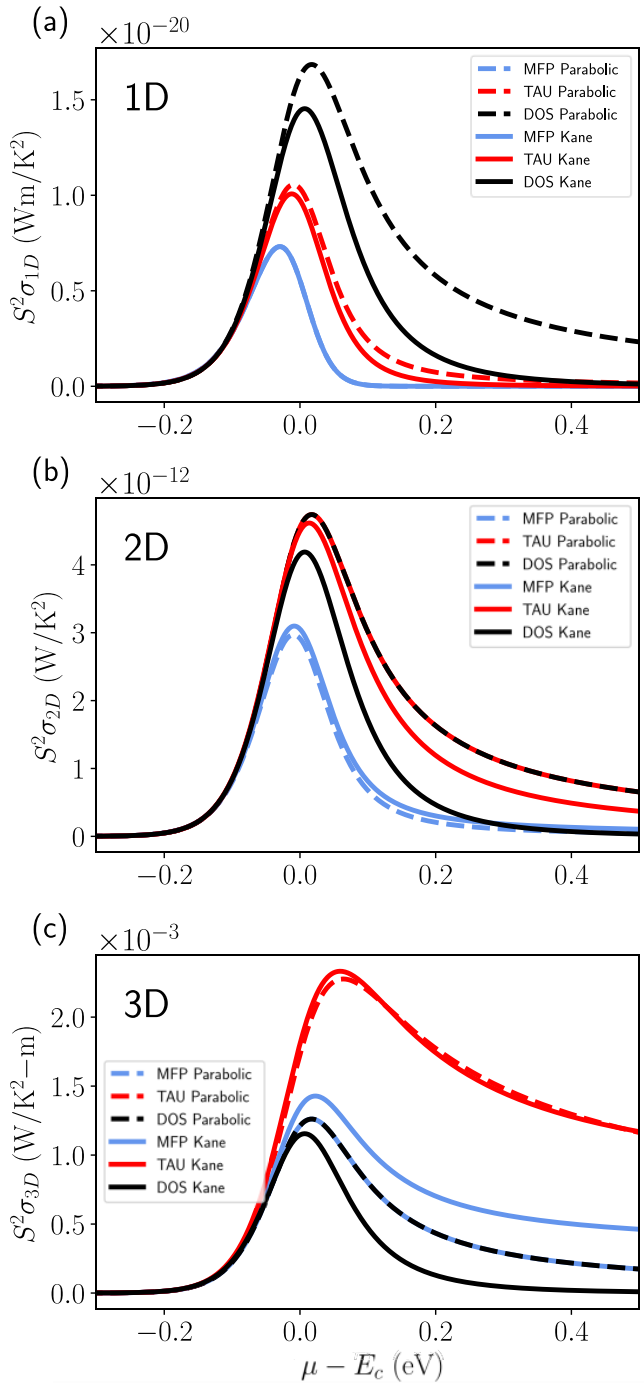

Figure 3.5: Kane band. Power factor PF versus Fermi level μ in (a) 1D, (b) 2D, and (c) 3D, using the MFP, TAU and DOS scattering models. The results of a single isotropic band are presented as dashed lines. For these calculations, $m^* = m_0$, $\alpha = 1.0$ eV^{-1}, $T = 300$ K, and $\langle\langle\lambda\rangle\rangle_{\mu=E_C} = 10$ nm.

result in improved performance. DOS scattering is consistent across all dimensions in its prediction that a Kane band will perform worse than a pure parabolic band.

3.3 Quartic Bands (Mexican Hat Model)

Next, we consider a more exotic class of band structure, sometimes referred to as "ring-shaped", "warped" or "Mexican-hat" bands [42], that arise in few-layer 2D materials. This type of $E(k)$ is qualitatively different from more common parabolic/Kane dispersions, in that the band edge doesn't correspond to a *point* in k-space but rather a *line* (a ring) in k-space, which gives rise to distinct properties. Previous studies have proposed that the TE characteristics of such ring-shaped band materials (*e.g.* monolayer Bi, bilayer graphene, few-layer Bi_2Te_3) would outperform those of standard dispersions [16,17,42] – with the benefits coming from a rapid, discrete increase in the DOM at the band edge. However, the previous analyses relied on either the MFP or TAU scattering models, which we have shown can differ significantly from the more physical DOS model. Here, we revisit the performance of this type of dispersion by comparing all three scattering models, using approximate analytical descriptions for the $E(k)$.

There are a couple of proposed dispersion models that resemble the more rigorous first-principles computed ring-shaped dispersions, including the Rashba band model and the quartic band model [42] – expressions for both are provided in Appendix E, but our analysis we will focus mainly on the latter. The dispersion of the quartic model contains a k^4 contribution and is given by

$$E(k) = \epsilon_0 - \frac{\hbar^2 k^2}{2m^*} + \frac{1}{4\epsilon_0}\left(\frac{\hbar^2 k^2}{2m^*}\right)^2, \tag{3.5}$$

where ϵ_0 is the energy at the Γ-point, and m^* the corresponding effective mass (see Fig. 3.6). Note that Eq. (3.5) is for a 2D band structure, with k residing in the k_x-k_y plane. This functional form can be derived explicitly by applying a tight-binding model to group-VA elements forming 2D hexagonal lattices, which have been confirmed by DFT calculations [43]. This electronic dispersion has two key features. Firstly, as mentioned above, the band edge consists of a ring of critical points of radius $k_0 = 2\sqrt{m^*\epsilon_0}/\hbar$, rather than a single critical point at Γ, as in the cases of

Energy Range	$M(E)$	$V_\lambda(E)$	$D(E)$	$\Sigma_{\text{MFP}}(E)$	$\Sigma_{\text{TAU}}(E)$	$\Sigma_{\text{DOS}}(E)$
$E < \epsilon_0$	$\sqrt{1+\sqrt{\frac{E}{\epsilon_0}}+\sqrt{1-\sqrt{\frac{E}{\epsilon_0}}}}$	$\frac{2\sqrt{E}}{\sqrt{1+\sqrt{\frac{E}{\epsilon_0}}}+\sqrt{1-\sqrt{\frac{E}{\epsilon_0}}}}$	$2\sqrt{\frac{\epsilon_0}{E}}$	$\sqrt{1+\sqrt{\frac{E}{\epsilon_0}}+\sqrt{1-\sqrt{\frac{E}{\epsilon_0}}}}$	$2\sqrt{E}$	E
$E > \epsilon_0$	$\sqrt{1+\sqrt{\frac{E}{\epsilon_0}}}$	$\sqrt{E}\sqrt{1+\sqrt{\frac{E}{\epsilon_0}}}$	$\sqrt{\frac{\epsilon_0}{E}}$	$\sqrt{1+\sqrt{\frac{E}{\epsilon_0}}}$	$\sqrt{E}(1+\sqrt{\frac{E}{\epsilon_0}})$	$E(1+\sqrt{\frac{E}{\epsilon_0}})$

Table 3.3: Quartic band. Energy dependence of distribution-of-modes $M(E)$, average velocity $V_\lambda(E)$, density-of-states $D(E)$, and transport distribution $\Sigma(E)$ (within the MFP, TAU and DOS scattering models). When present, the factors of 2 serve to enforce the continuity (or lack thereof) of the distributions. For full expressions, refer to Appendix E.3.

parabolic or Kane bands. Secondly, the inner ring of states vanishes for energies above ϵ_0. These features are key to understanding the functional forms of the electronic quantities of interest, as discussed next.

The $D(E)$, $M(E)$, and $V_\lambda(E)$ are shown in Fig. 3.7, with their respective expressions provided in Appendix E.3. The ring of states at the band edge results in a DOM that turns on like a step function. This large number of modes near the band edge is the main reason that materials with ring-shaped dispersions were investigated as potential high-performance thermoelectrics – this feature is shared with both quartic and Rashba bands. However, there is a second important electronic feature when considering ring-shaped $E(k)$ materials, and that is the discontinuity in the DOS. Near the Γ point, the inner section of the band is roughly that of an inverted 2D parabolic band. Since the DOS of such a band is constant, the "turning off" of this portion of the band results in a discontinuous drop in the DOS, as shown in Fig. 3.7. No such discontinuity exists with the Rashba band model; see Appendix E.4.

This discontinuity has important consequences for the transport distribution of ring-shaped band materials, as shown in Fig. 3.8. Whereas the MFP and TAU models are blind to any changes in the DOS, the DOS scattering model predicts a significant decrease in scattering rate for electrons with energies greater than ϵ_0. This abrupt decrease in scattering rate has been explicitly calculated for the case of charged impurity scattering in warped band materials [44]. The reduced scattering leads to a step-like increase in the transport distribution, not at the band edge, but at $E = \epsilon_0$. We observed enhancements in both the conductivity and the Seebeck coefficient when the Fermi level is near this feature, and the combined effect of these enhancements is

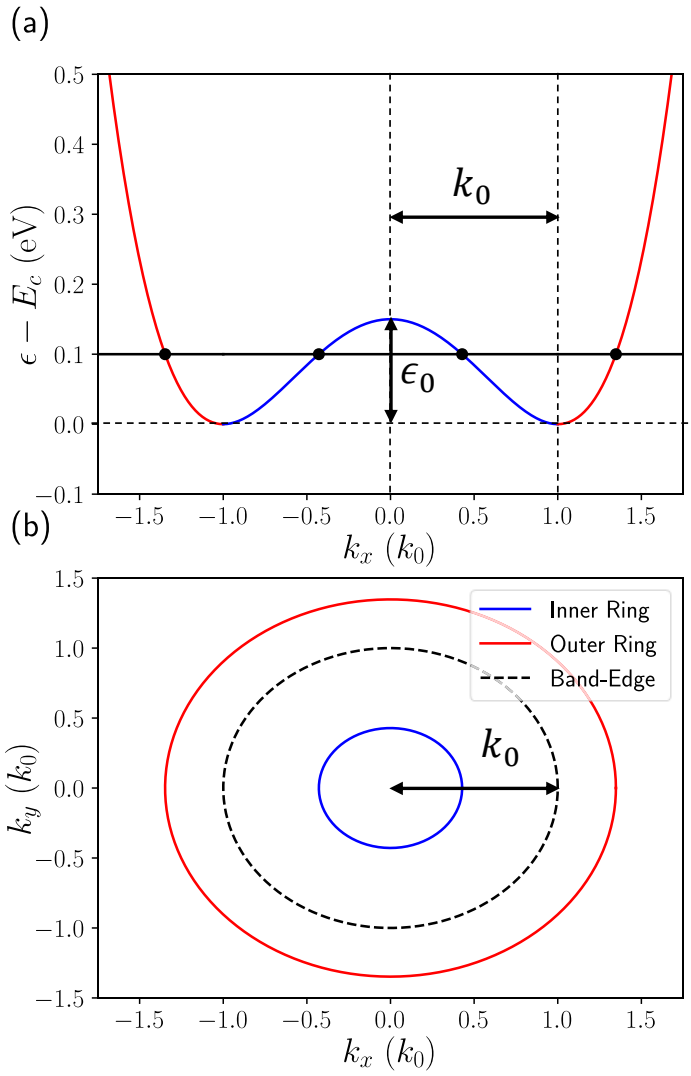

Figure 3.6: Electron dispersion of a quartic band ($m^* = m_0$ and $\epsilon_0 = 0.15$ eV). (a) shows $E(k)$ versus k_x for $k_y = 0$, and (b) presents the constant energy surface at $E(k) = 0.1$ eV. Note the existence of two distinct surfaces of constant energy (when $E(k) < \epsilon_0$) – the band edge appears as a dashed line.

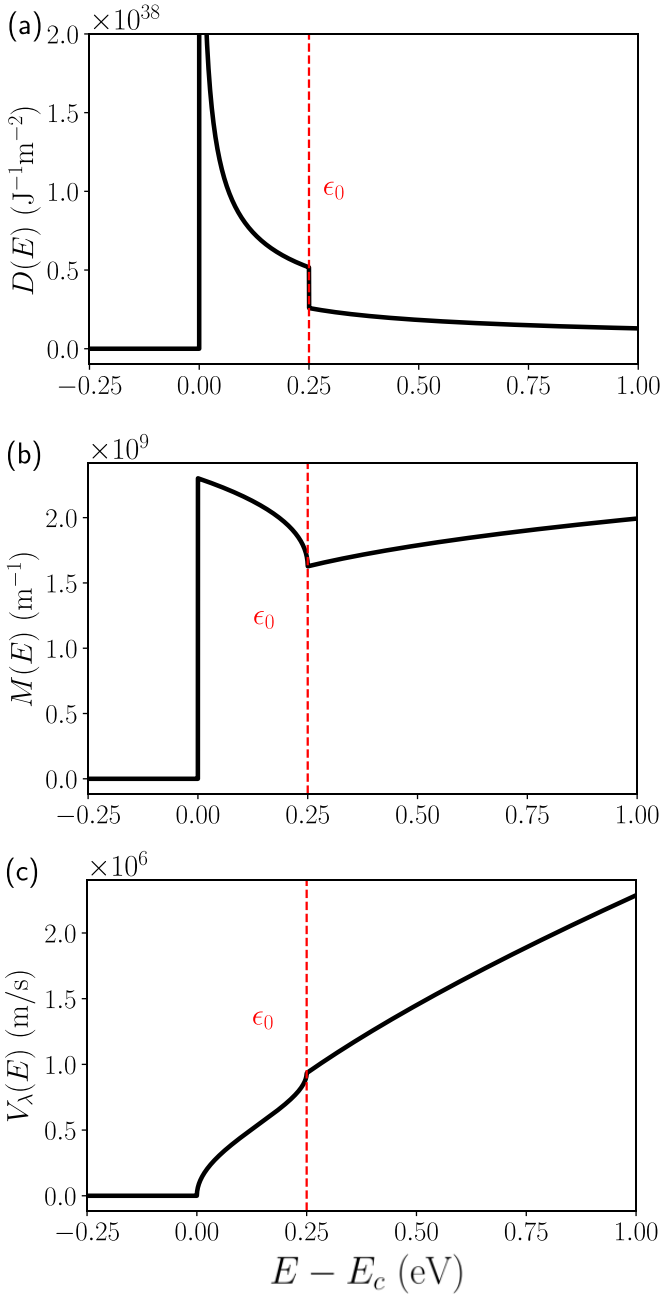

Figure 3.7: (a) Density-of-states $D(E)$, (b) distribution-of-modes $M(E)$, and (c) average velocity $V_\lambda(E)$ versus energy for a quartic band. For these calculations, $m^* = m_0$ and $\epsilon_0 = 0.25$ eV (indicated with vertical red lines).

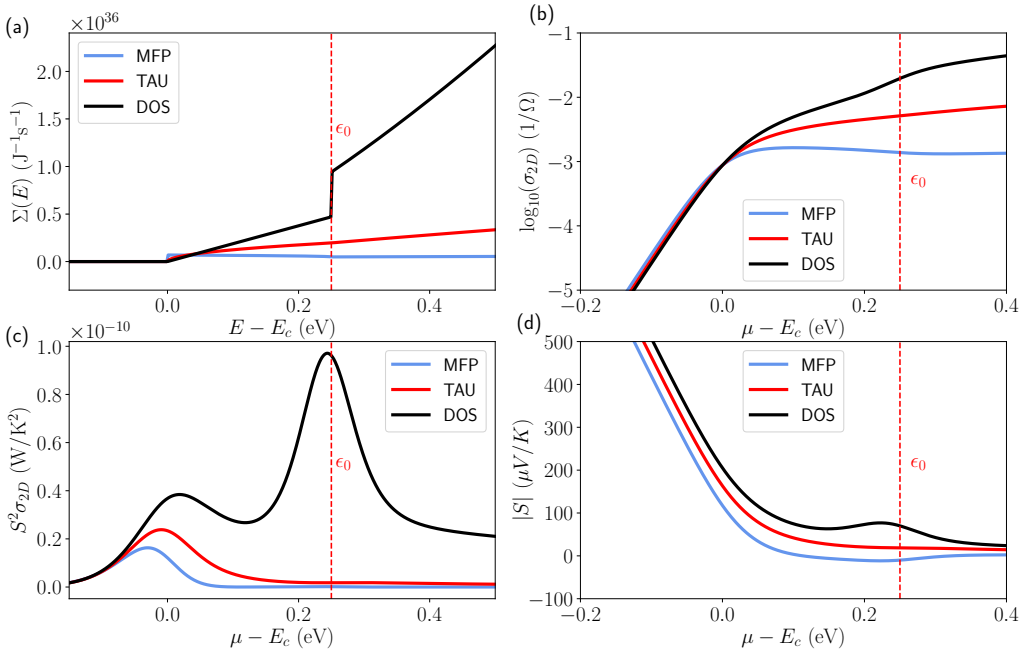

Figure 3.8: Thermoelectric transport properties for a single quartic band. (a) Log plot of electrical conductivity σ_{2D} versus Fermi level μ, (b) Transport distribution $\Sigma(E)$ versus energy with $\mu = E_C$, (c) magnitude of Seebeck coefficient $|S|$ versus Fermi level and (d) power factor PF versus Fermi level, using MFP, TAU and DOS scattering models. For these calculations, $m^* = m_0$, $\epsilon_0 = 0.25$ eV, $T = 300$ K, and $\langle\langle\lambda\rangle\rangle_{\mu=E_C} = 10$ nm.

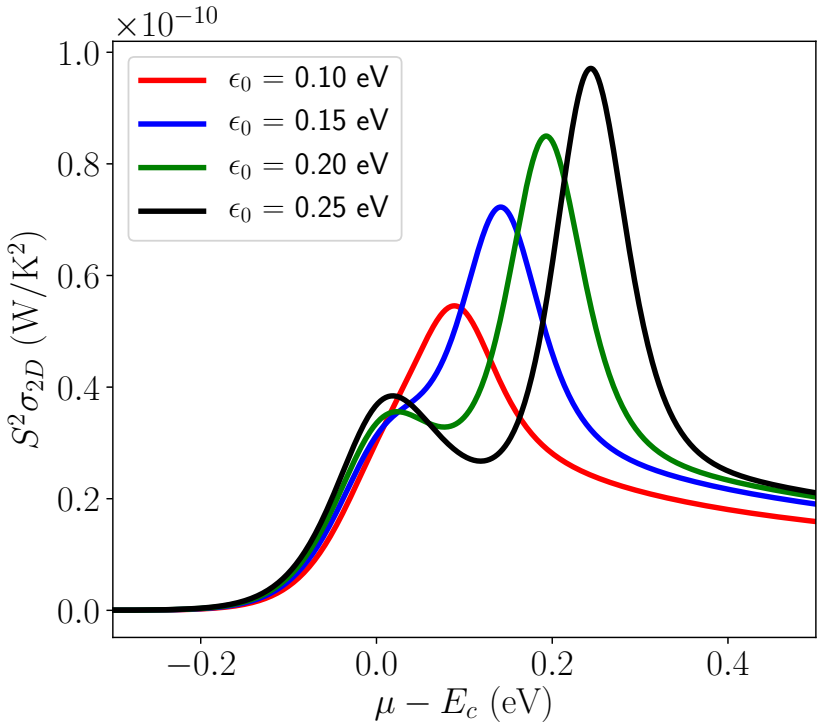

Figure 3.9: Quartic band. Power factor PF versus Fermi level μ, within the DOS scattering model, for varying $\epsilon = 0.1$, 0.15, 0.20 and 0.25 eV. For this plot, $m^* = m_0$, $T = 300$ K, and $\langle\langle\lambda\rangle\rangle_{\mu=E_C} = 10$ nm.

to produce a second local maximum in the power factor, a feature completely overlooked by the the MFP and TAU scattering models. This suggests that materials with ring-shaped dispersions may be even better thermoelectric materials than previously believed.

The observation of a second peak in PF, with the DOS model, raises the following question: What is the optimal value of ϵ_0, if our goal is to maximize the power factor? Figure 3.9 shows the power factor versus Fermi level, in the case of DOS scattering, for varying ϵ_0. We can see that for sufficiently small ϵ_0, there is only a single PF peak, which splits into two maxima (one near the band edge and one near ϵ_0) as ϵ_0 increases. It is easily seen that the maximum power factor increases with ϵ_0, so in principle, a larger ϵ_0 should bring about better thermoelectric performance. However, in reality, this will be limited by how far the Fermi level can be pushed into the band, via electrostatic gating or doping. Excessive doping may also begin to alter the electronic structure, which could limit projected performance.

In this chapter, we have compared the predictions of the commonly used constant-relaxation-time and constant-mean-free-path approximations to those of the more physical DOS-scattering approximation, when applied to analytical models of electronic dispersion. We find that the predictions of the DOS-scattering model can differ significantly, and even qualitatively from those of the simpler scattering approximations. The differences between the predictions scattering models are most pronounced when there are discontinuities in the density-of-states distribution, as shown using the quartic-band model. Our findings motivate a revisitation of previous studies of thermoelectric performance that made use of either the constant-MFP or constant-TAU scattering approximations, as a more careful treatment of carrier scattering may significantly impact the results obtained, particularly in the case of highly-warped bands.

Chapter 4

On the Thermoelectric Performance of Quintuple-Layered Semiconductor Systems

For room temperature applications, the most commonly used bulk thermoelectric materials are Sb_2Te_3, Bi_2Se_3, and Bi_2Te_3 (as well as alloys of these materials) [45–47]. These three materials each posess a rhombohedral crystal structure, which is shown in Figure 4.1. Due to the relatively large atomic masses of their constituent atoms, the allowed phonon modes in these materials take on very low energies, limiting the amount of thermal energy that can be transported via phonon transport. Futhermore, the phonon dispersions in these materials are highly anharmonic, resulting in large amounts of phonon scattering [48]. These properties result in extremely low lattice thermal conductivity values, a highly desirable feature for a thermoelectric material.

These materials have become the standard choices for room temperature thermoelectrics due to their combination of low lattice thermal conductivities on the order of 1 W/m-K [49], and respectable thermoelectric power factors on the order of 30 μW/cm-K^2 [50]. These material properties, namely the electronic power factor and the lattice thermal conductivity, are the two main quantities that researchers seek to improve in the search for better thermoelectric materials. Although there has been great progress in reducing the thermal conductivity values of thermoelectric materials [47, 51, 52], obtaining similar improvements in the electronic power factor has proved more difficult. Nevertheless, it is believed that major enhancements of the electronic properties will be needed to ensure future progress, as significant further reductions in κ_l are unlikely.

To this end, interest has been taken in the thermoelectric properties of another class of materials closely related to the bulk materials, known as quintuple-layers (QL). [53–55]. The bonding between every fifth atomic layer of the bulk structures of

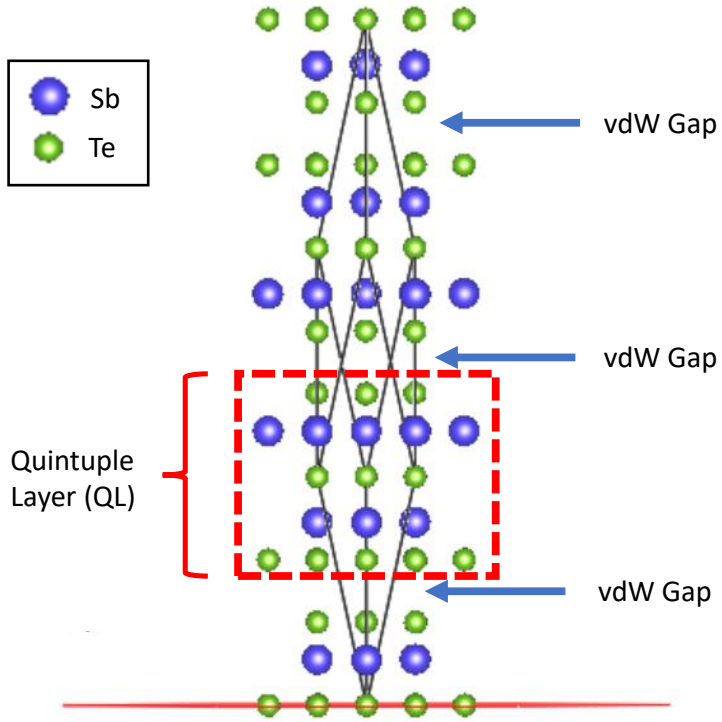

Figure 4.1: Rhombohedral crystal structure of bulk Sb_2Te_3, with the quintuple-layer sub-structure indicated with a red box.

Bi_2Te_3, Bi_2Se_3 and Sb_2Te_3 is predominantly due to van der Waals interactions [56], and is therefore relatively weak compared to the covalent bonds throughout the rest of the structure. As such, it is possible to mechanically cleave the bulk structure [57,58], obtaining a 2D structure only five atomic layers thick. Such structures can also be grown using molecular beam epitaxy [59, 60]. The resulting electronic structures of these QL systems are dramatically different from those of their bulk counterparts.

The most significant change is the emergence of ring-like structures in the uppermost valence states, which are qualitatively similar to the quartic-band model discussed in Chapter 3. Much like the quartic model, the ring-like valence bands of these quintuple-layer systems lead to a large number of available states at energies very near the valence band edge. This results in a step-like feature in the distribution-of-modes at the valence band edge, as will be shown explicitly in the following sections. This feature has been the focus of most theoretical investigations of these quasi-2D materials, and is believed to be highly desirable for thermoelectric performance [17, 42, 61]. However, all of these investigations have limited themselves to either the constant-MFP or constant-relaxation-time scattering approximations. In light of what was found for the quartic-model in Chapter 3, we have reason to expect that these models may fail to accurately describe potential performance enhancements due to sharp transport distribution features arising from atypical features in the density-of-states distributions. This motivates a new investigation of these materials using the more physical DOS-scattering model, to explore the TE properties and how they compare to the predictions of the other scattering models. We will begin with a brief discussion of the thermoelectric properties of the bulk state, focusing on the representative case of Sb_2Te_3, but our analysis will focus primarily on the thermoelectric properties of the related single-QL and double-QL systems.

4.1 Numerical Details

All DFT calculations were performed with the Quantum Espresso package [62], using a projector-augmented wave [63] implementation of the Perdew-Burke-Erzenhof (PBE) functional [64]. Spin-orbit interactions were included, as well as Grimme-D2 van der Waals corrections [65]. The plane-wave cutoff energy was set to 110 Rydberg

for all systems studied. Bulk calculations made use of the rhomohedral primitive cell, while thin film calculations were performed using the primitive hexagonal cells. The self-consistent calculations were performed using a k-mesh of (11x11x1: films, 11x11x11: bulk) generated using the Monkhorst-Pack scheme [66]. For the non-self-consistent calculations used to resolve the band structure for the calculation of $M(E)$ and $V_\lambda(E)$, Cartesian grids of 115x85x1 k-points were used for the thin films, and Cartesian grids of 75x45x19 were used for the bulk structures. These rectangular Brillouin zones are dual to the rectangular supercells chosen in real-space, which are larger than their respective primitive unit cells by factors of 2 (hexagonal) and 6 (rhombohedral). The density-of-states distributions were resolved with a tetrahedron integration technique [37] using a Monkhorst-Pack grid of (51x51x1: films, 51x51x51: bulk). For the thin films, a vacuum layer of 15 Å was included to prevent any interaction between neighboring cells. Experimental lattice constants were used, as has been done previously [17, 46, 55], and the atomic coordinates were relaxed until the forces on the atoms were less than 0.01 eV/ Å. Fixed occupations were used for the electronic states.

When calculating the thermoelectric properties, the scissor operator was used to adjust the DFT calculated band gaps to more accurate values. For the bulk materials, we used experimental band gap values, but for the thin films we used the results of GW calculations [67, 68], as conclusive data on the band gaps of single-QL materials is still lacking. The lattice thermal conductivity values were set to 1.5 W/m-K, in accordance with rigorous scattering calculations performed on quintuple-layers of Bi_2Te_3 [69]. We set the scattering constants (*i.e.* the parameters λ_0, τ_0 and K_0 that appear in the definitions of the transport distributions) for the valence and conduction states separately, such that the average mean free path for backscattering of electrons was 10 nm when the Fermi level was set to either band edge, *i.e.* $\langle\langle\lambda\rangle\rangle_{\mu=E_v} = \langle\langle\lambda\rangle\rangle_{\mu=E_c} = 10$ nm (see Appendix B for details). All calculations were performed assuming a temperature of 300 K.

4.2 Bulk Rhombohedral Materials

The bulk structures of Bi_2Te_3, Bi_2Se_3 and Sb_2Te_3 are most elegantly expressed using rhombohedral coordinates. The primitive lattice vectors of these rhombohedral systems are given by

$$v_1 = (-\frac{a}{2}, -\frac{a}{2\sqrt{3}}, \frac{c}{3}),$$
$$v_2 = (\frac{a}{2}, -\frac{a}{2\sqrt{3}}, \frac{c}{3}),$$
$$v_3 = (0, \frac{a}{\sqrt{3}}, \frac{c}{3}),$$

where a and c are the traditional hexagonal lattice parameters. The crystal structure of these bulk materials can also be expressed in hexagonal coordinates, but the hexagonal unit cell contains 15 atoms instead of a mere 5 with the primitive cell, making the resulting DFT calculations considerably more intensive. When working with the rhombohedral primitive cell, the 5 basis atoms all lie along the z-axis. There are two equivalent Bi (Sb) sites, two equivalent Te (Se) sites, and a third Te (Se) site that is inequivalent to the previous two. When expressed in relative coordinates (*i.e.* in terms of the primitive lattice vectors), the locations of these sites are given by $(\pm\mu, \pm\mu, \pm\mu)$, $(\pm\nu, \pm\nu, \pm\nu)$, and $(0, 0, 0)$ respectively, as shown in Figure 4.2. The values of the structural parameters used in our DFT calculations are provided in Table 4.1.

Material	a (Å)	c (Å)	ν	μ	DFT Gap (eV)	Exp. Gap (eV)
Bi_2Se_3	4.138	28.64	0.2106	0.4003	0.187	0.30
Bi_2Te_3	4.383	30.49	0.2093	0.3999	0.081	0.21
Sb_2Te_3	4.260	30.35	0.2123	0.3978	0.100	0.21

Table 4.1: Structural parameters used in DFT simulations of bulk rhomohedral materials.

We will limit our discussion of the bulk results to the representative case of Sb_2Te_3, but the general trends outlined hold for all three materials. Figure 4.3 shows the band structure of bulk Sb_2Te_3. These bulk rhombohedral materials have very complex band structures, containing a mixture of ellipsoidal valleys, Kane-like linear branches, and

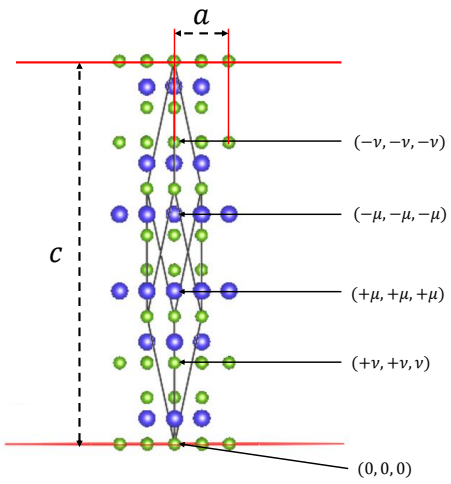

Figure 4.2: Structural diagram of the primitive cell of the bulk rhombohedral materials Sb_2Te_3, Bi_2Te_3 and Bi_2Se_3

regions with especially flat dispersions. This is due in part to the significant role that spin-orbit coupling plays in these materials. Despite these complex dispersion features, however, the density-of-states and distribution-of-modes are relatively well behaved, resembling those of more typical semiconductors, as shown in Figure 4.4. The resulting transport distributions are shown in Figure 4.5.

The features observed in the transport distribution plots are qualitatively very similar to the 3D Kane model presented in Chapter 3. For such a dispersion, the MFP and TAU transport distributions both increase super-linearly with energy, while the DOS transport distribution 'rolls over' and approaches a constant value (see Appendix E.2, where analytic expressions for the quantities defining Σ_{DOS} are provided). Because of the very similar shape of the distribution-of-modes and density-of-states distributions (as shown in Figure 4.4), the benefits provided by the increasing number of states available for transport are almost exactly cancelled out by the corresponding increasing in scattering that results, and the end result is a transport distribution that is nearly flat. This roughly-constant transport distribution is not desirable for thermoelectric performance for two reasons, firstly because its magnitude is relatively small, and secondly because flat transport distributions result in very small Seebeck coefficients due to the anti-symmetric nature of the first-order Fermi window function, W_1. The resulting figures-of-merit are shown in Figure 4.6. Predictably, in light

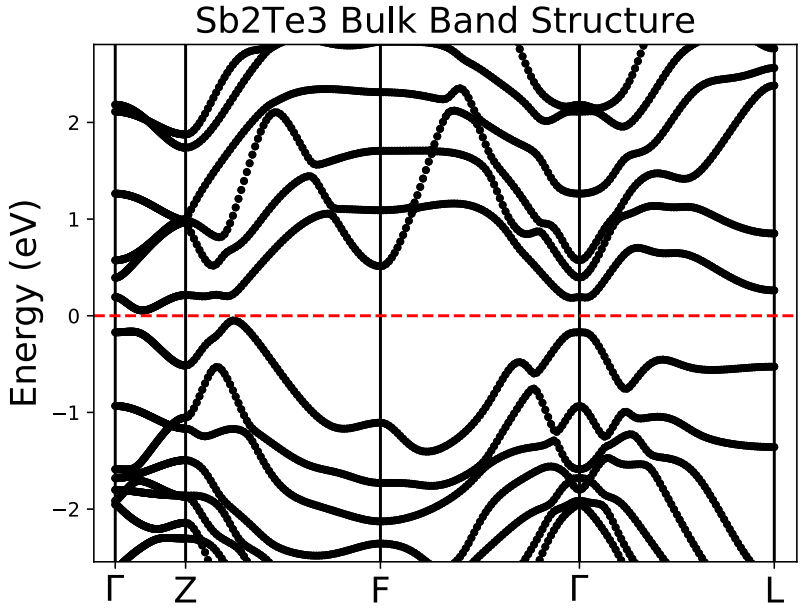

Figure 4.3: Band structure of bulk Sb_2Te_3, plotted along the high-symmetry points of the 3D rhombohedral Brillouin zone. $E = 0$ corresponds to the valence band edge, and the band gap shown is the un-adjusted PBE band gap obtained via DFT.

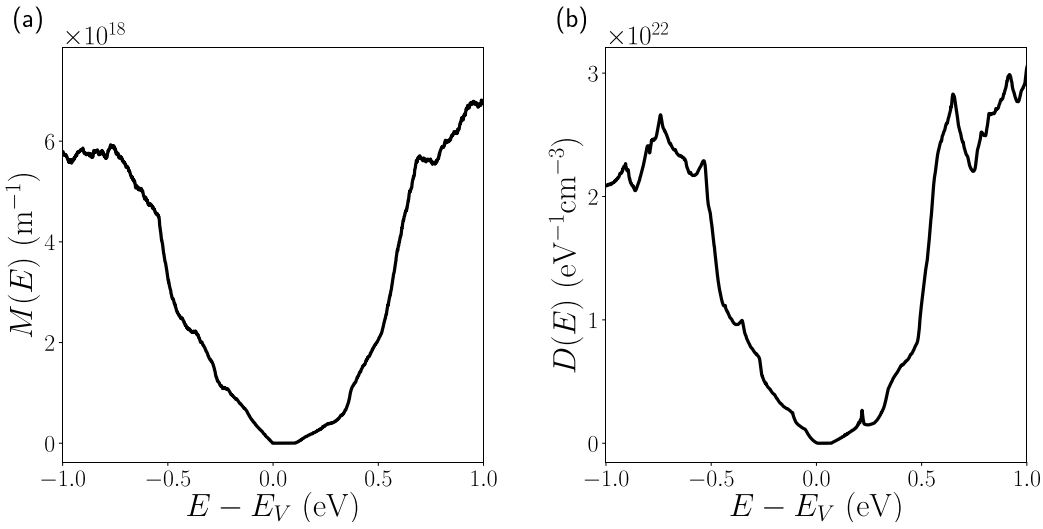

Figure 4.4: Plots of (a) distribution-of-modes and (b) density-of-states vs. energy level for bulk Sb_2Te_3. The band gap shown is the un-adjusted PBE band gap.

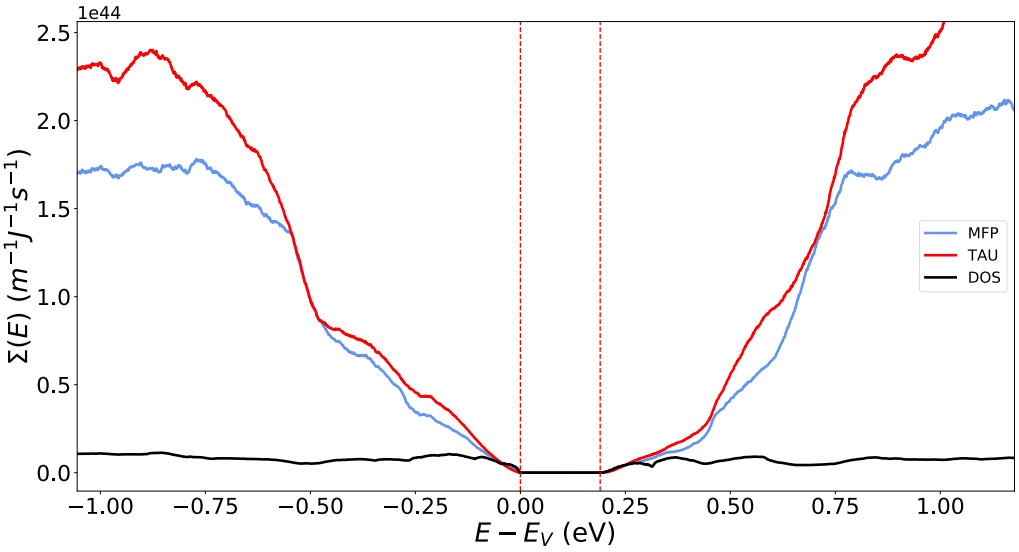

Figure 4.5: Transport distributions vs. energy level (relative to the valence band edge) of bulk Sb_2Te_3, for the constant-MFP, constant-TAU and DOS-scattering models. The scattering constants for the conduction and valence states are set separately such that $\langle\langle\lambda\rangle\rangle_{\mu=E_v} = \langle\langle\lambda\rangle\rangle_{\mu=E_c} = 10$ nm. The band gap shown has been adjusted to the experimental value of 0.21 eV.

of the transport distributions shown above, the DOS-scattering model predicts the lowest ZT values of the three scattering models considered.

While these bulk materials are still the default choice for most room temperature thermoelectric applications, the complex, yet effectively 'Kane-like' nature of their dispersions makes significant further enhancements of their electronic properties unlikely. If these materials are to be superseded by some new and superior class of thermoelectrics, which is the ultimate goal of many researchers, the new class of materials will likely need to possess a significantly different kind of electronic dispersion. Quintuple-layered systems of Bi_2Te_3, Bi_2Se_3 and Sb_2Te_3 have been proposed as candidates for this new class of thermoelectric materials, as their combination of low lattice thermal conductivity values and exotic band structures have made them promising candidates for highly-efficient thermoelectric conversion. However, all theoretical studies of their thermoelectric properties have (to date) only made use of either the constant-relaxation-time or constant-mean-free path approximations. In light of our findings from the previous chapter, we now perform the first study of the

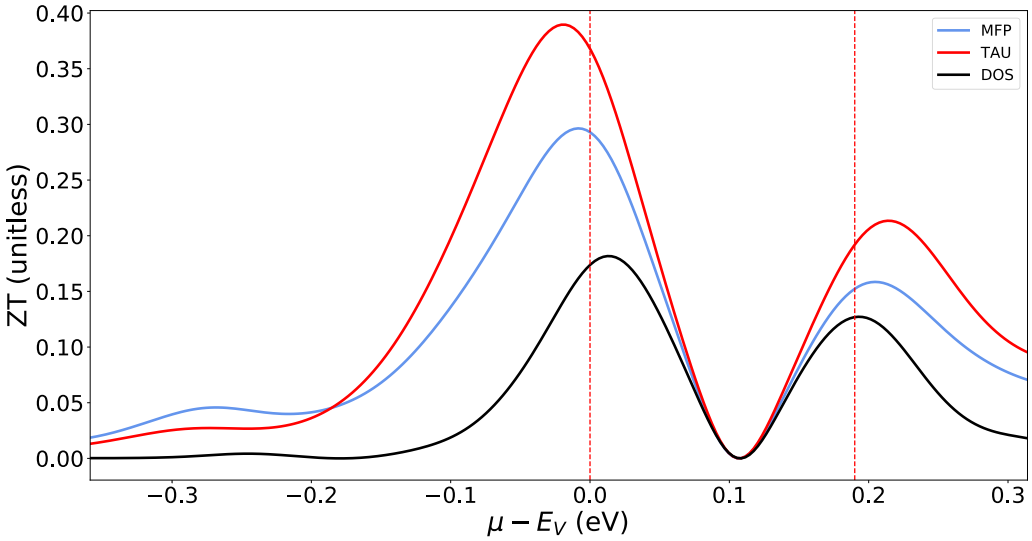

Figure 4.6: Figures-of-merit predicted by the constant-MFP, constant-TAU, and DOS-scattering models when applied to bulk Sb_2Te_3. The band gap shown has been adjusted to match the experimental value of 0.21 eV.

thermoelectric properties of these quintuple-layered systems making use of the DOS-scattering approximation, which should provide new insight into the impact that the scattering physics has on the properties of these exotic materials.

4.3 Single Quintuple-layers

We now proceed to our analysis of the single-QL systems of Sb_2Te_3, Bi_2Te_3 and Bi_2Se_3. The natural choice of coordinates for such systems is the hexagonal basis, the primitive lattice vectors of which are given by

$$\begin{aligned} v_1 &= (a, 0, 0), \\ v_2 &= (-\frac{a}{2}, \frac{\sqrt{3}}{2}a, 0), \\ v_3 &= (0, 0, c), \end{aligned}$$

where a and c are the standard hexagonal lattice parameters. As in the case of the bulk materials, the unit cell contains five atoms: two equivalent Bi (Sb) sites, two equivalent Te (Se) sites, and a third, inequivalent Te (Se) site. The x and y

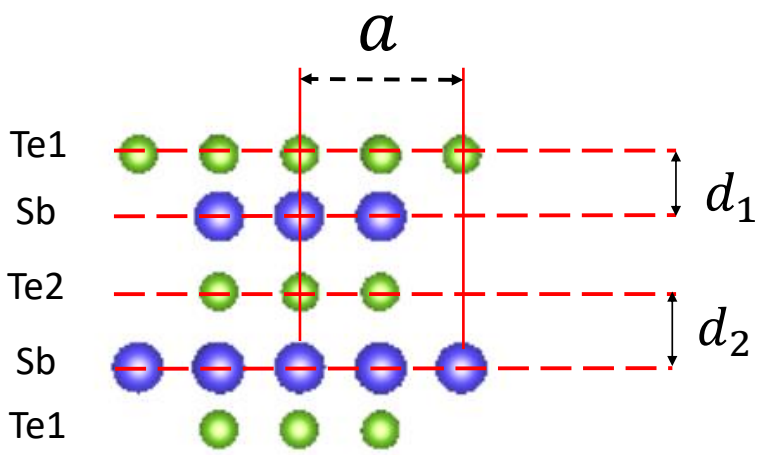

Figure 4.7: Structural diagram of the primitive cell of a single-QL material.

coordinates of the QL basis atoms are dictated by the ABC hexagonal-stacking of the atomic layers, while the z-coordinates are expressed in terms of the inter-layer spacings d_1 and d_2, which correspond to the Te1-Sb and Sb-Te2 spacings, as illustrated in Figure 4.7. We note that the atomic coordinates of every atom in the quintuple-layer system are completely determined by the bulk structure. The values of the structural parameters used in our DFT calculations are provided in Table 4.2.

Material	a (Å)	d_1 (Å)	d_2 (Å)	DFT Gap (eV)	GW Gap (eV)
Bi_2Se_3	4.138	1.600	1.903	0.45	0.90
Bi_2Te_3	4.383	1.755	2.047	0.23	0.64
Sb_2Te_3	4.260	1.734	1.999	0.46	0.82

Table 4.2: Structural parameters used in DFT simulations of hexagonal single-QL materials.

4.3.1 Bi_2Te_3 QL

We begin our analysis of these quintuple-layer systems with the case of a single QL of Bi_2Te_3. A band structure plot for this material is shown in Figure 4.8. The most significant feature is the presence of not one, but two ring-like features at the valence band edge. The resulting electronic properties (namely $M(E)$, $V_\lambda(E)$ and $D(E)$) are

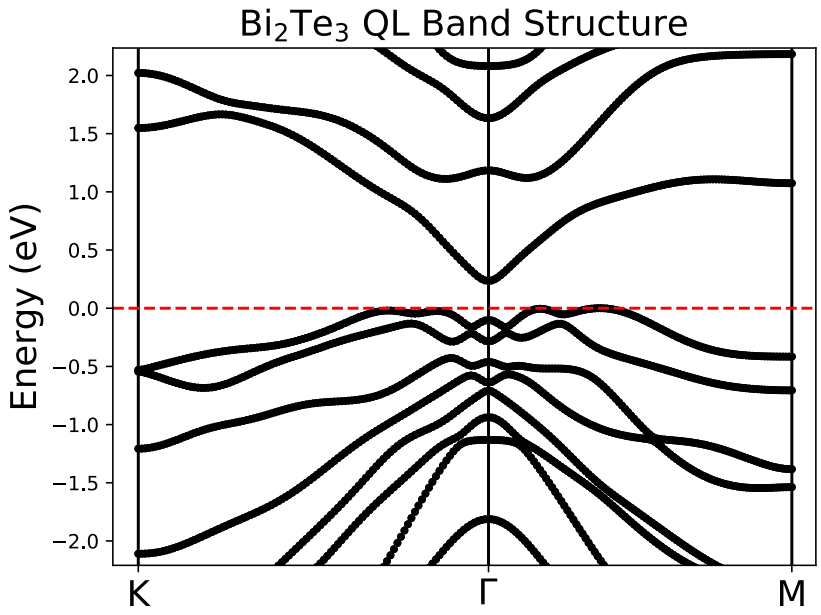

Figure 4.8: Band structure of a single quintuple-layer of Bi_2Te_3, along the high-symmetry points of the 2D hexagonal Brillouin zone. $E = 0$ corresponds to the valence band edge, and the band gap shown is the un-adjusted PBE band gap obtained via DFT.

shown in Figure 4.9. We note firstly that there is large step-like feature in the DOM at the valence band edge. This occurs for the same reason as the step feature observed in the analytic quartic-band model, namely the presence of ring-like constant-energy surfaces at the band-edge (although in this there are two such features). However, we also observe abrupt changes in the magnitude of all three quantities roughly 0.05 eV below the valence band edge. While the quartic-band model does predict a discontinuity in the DOS distribution, it predicts $M(E)$ and $V_\lambda(E)$ to be continuous for energies below the band edge. Clearly, the electronic dispersion feature responsible for the observed discontinuities cannot be the simple "parabolic band turn-off" described by the quartic model. To gain further insight into the nature of this dispersion feature, in Figure 4.10 we plot the constant energy contours of the electronic dispersion of the Bi_2Te_3 quintuple-layer for energies near the valence band edge.

The two ring-like local maxima at the valence band edge are labeled as the inner and outer rings. The more interesting feature, however, is the third ring-like constant

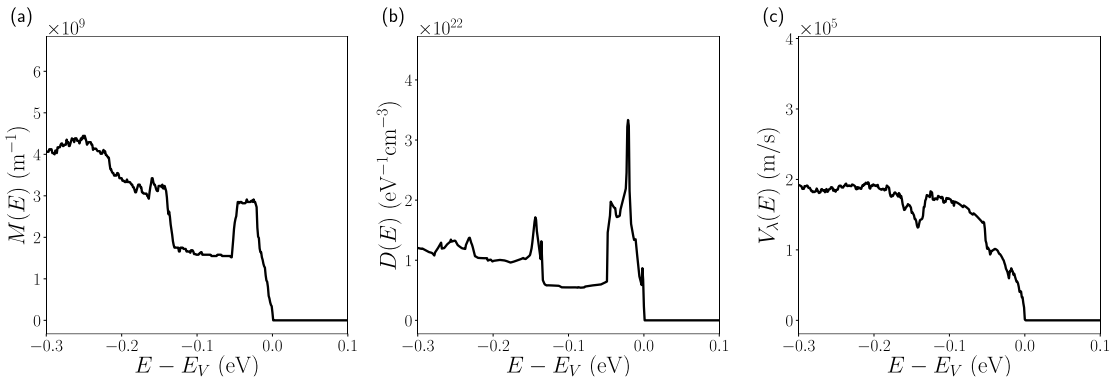

Figure 4.9: Electronic properties of a double quintuple-layer of Bi_2Te_3. Plotted are the (a) distribution-of-modes, (b) density-of-states and (c) average velocity distributions, all vs. energy level (relative to the valence band edge).

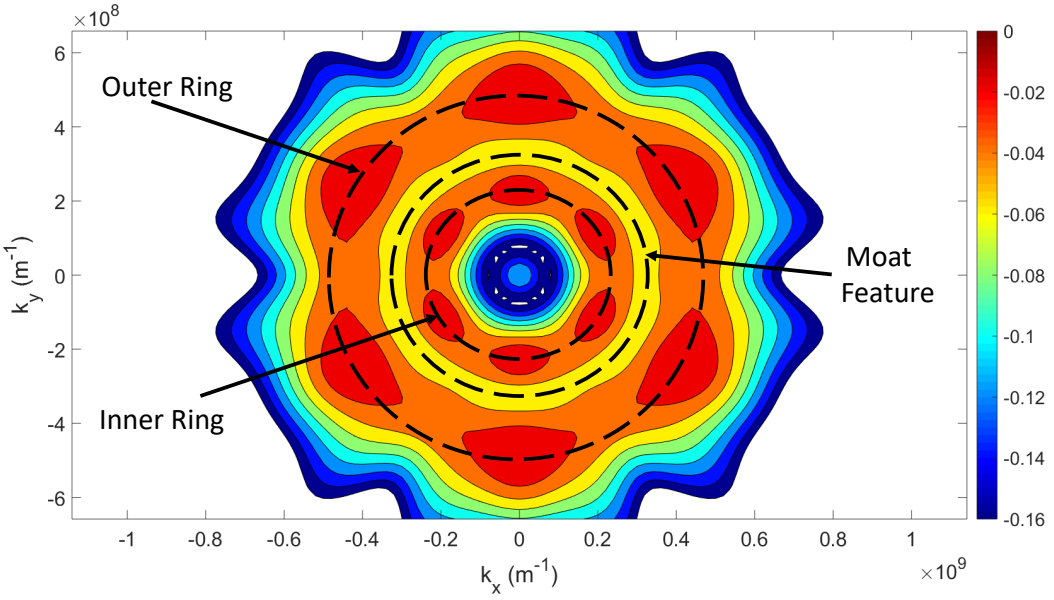

Figure 4.10: Constant energy contours for the uppermost valence band of a single quintuple-layer of Bi_2Te_3. Energies are given in units of eV, and $E = 0$ corresponds to the valence band edge.

energy surface nested in between these two band-edge features. This particular feature corresponds to a local *minimum* in the electronic dispersion (unlike the inner and outer rings), and occurs at the same energy level as the observed discontinuities in $M(E)$ and $V_\lambda(E)$. The circular nature of this constant energy surface indicates that this particular constant energy surface is nearly isotropic.

While the quartic-band model is commonly used to describe the impact of ring-like local maxima at the band-edge, it cannot readily offer insight into the consequences of ring-like local *minima* at energies below the band edge. To this end, we introduce a new analytic model of electronic dispersion that can, which we will henceforth refer to as the 'octic model', as it is an eighth-order polynomial in k:

$$\epsilon(k) = -\frac{\epsilon_0}{a^4 b^4}(k^2 - a^2)^2(k^2 - b^2)^2. \tag{4.1}$$

This analytic dispersion model possesses three separate critical surfaces (as well as a single critical point at Γ), which are illustrated in Figure 4.11. The critical surface corresponding to a local minimum in the electronic dispersion bears a topographic resemblance to a moat, and so we shall henceforth refer to it as the moat of the electronic dispersion. We will refer to the critical surfaces at the band-edge with radii a and b as the inner and outer ring features, respectively. The parameter ϵ_0 determines the energy at the Γ point: $\epsilon(k_x = 0, k_y = 0) = -\epsilon_0$.

The presence of a ring-like critical surface at an energy *below* the band-edge has a significant impact on the functional form of the quantities of interest. Sketches of the resulting $M(E)$, $V_\lambda(E)$ and $D(E)$ distributions for the octic model are shown in Figure 4.12, with the full analytic expressions provided in Appendix C. As was previously shown with the quartic model, the presence of ring-like critical surfaces at the band edge results in a DOM distribution that turns on like a step function. The DOM distribution for the octic model, however, also contains a second discontinuity at the location of the moat. This second step-like feature occurs because one abruptly 'loses' the large number of transport channels provided by the moat feature. Since these states have vanishingly small velocities as one approaches the bottom of the moat, their 'turning-off' also causes the average velocity to discontinuously increase,

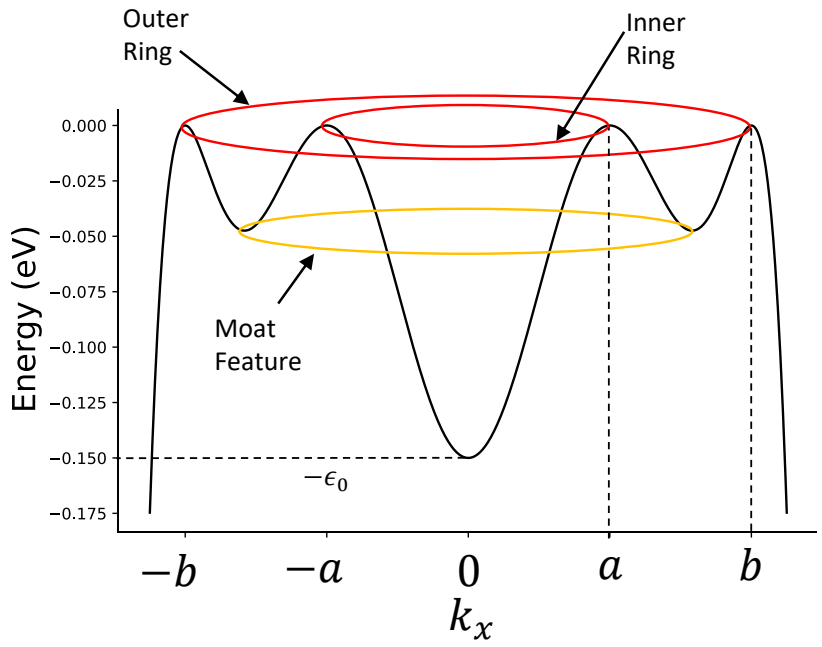

Figure 4.11: Diagram illustrating the critical constant energy surfaces of the analytic octic dispersion model.

as the average no longer includes a large number of zero-velocity states. The second singularity in the DOS occurs for the same reason as the singularity observed at the band edge: any constant energy surface containing a continuum of critical points will cause the density-of states to blow up (for 2D materials).

The features observed at $E = -\epsilon_0$, namely a discontinuity in the DOS and slope-discontinuities in the both DOM and average velocity, are essentially the same as those observed previously in the quartic band, *i.e.* they are due to the *single* critical point at Γ. We emphasize here that the features produced by the critical moat are 'stronger' than those produced by a single critical point, in that they produce discontinuities in quantities that are continuous in the quartic model, namely $M(E)$ and $V_\lambda(E)$. They are therefore more robust to small deviations from the analytic model. For example, we do not expect any DOS distribution obtained via density-functional theory to possess a true singularity, as real dispersions will inevitably possess at least some small degree of anistropy. Nevertheless, for sufficiently small deviations from

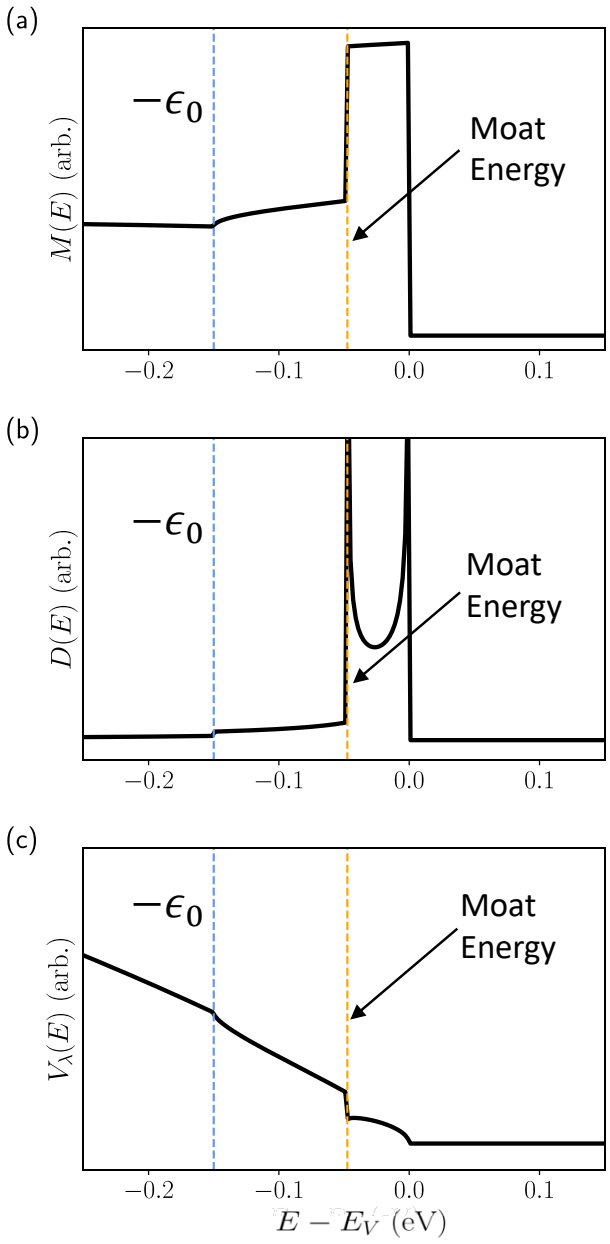

Figure 4.12: Sketches of the electronic properties of single octic band with $a = 1$, $b = 2$ and $\epsilon_0 = 0.15$ eV. Plotted are the (a) distribution-of-modes, (b) density-of-states and (c) average velocity distributions, all vs. energy level (relative to the valence band edge).

isotropicity, one would still expect to see an abrupt decrease (if not an outright discontinuity) in the magnitude of the DOS distribution near the moat. Similarly, the magnitude of the $M(E)$ and $V_\lambda(E)$ distributions obtained from density functional theory calculations may still exhibit large changes in magnitude over very small energy ranges, even if these features are not truly discontinuous, strictly speaking.This is essentially what we observe in our Bi_2Te_3 distributions, which possess a nearly-isotropic moat feature.

In Figure 4.13, we compare the distributions obtained from first-principles calculations of a single quintuple-layer of Bi_2Te_3 to those predicted by the analytic octic model. This figure does not contain any new information, and serves only to highlight the similarities between our new analytic model and the numerical data. We can see that the discontinuities predicted by our octic model are all present in the corresponding Bi_2Te_3 QL distributions obtained from first-principles, confirming our claim that it is the moat feature at $E = -0.05$ eV that is responsible for the observed features in the transport distributions. We note here that while the octic model is a useful tool for understanding the impact of moat-like critical surfaces, it does not accurately reproduce the curvature of real electronic dispersions. As we are only seeking a qualitative description of the impact of the moat feature, we set the ring radii to the arbitrary values of $a = 1$ and $b = 2$, and set the value of ϵ_0 such that the moat feature of our simple model occurs at the same energy as the corresponding feature in Bi_2Te_3 ($\epsilon_0 = 0.16$ eV).

With our newfound understanding of the origin of the observed discontinuities in $M(E)$ and $V_\lambda(E)$, we are now in a position to examine the resulting transport distributions, which are shown in Figure 4.14. We can see that the DOS-scattering transport distribution steps up abruptly at the energy of the moat feature (-0.05 eV), and has the largest magnitude of the three transport distributions over most of the relevant energy range (as only states within a few k_BT of the Fermi level will contribute appreciably to transport). This is similar to the discontinuity observed in the DOS-scattering transport distribution of the quartic-band model, for which the DOS-scattering model was found to predict improved thermoelectric performance. As such, we would expect the DOS scattering model to predict the largest ZT value

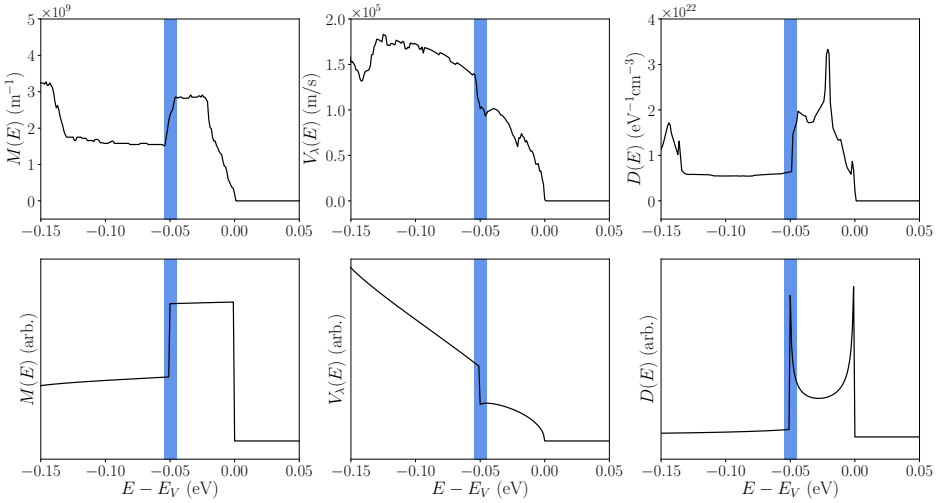

Figure 4.13: Comparison of the electronic properties of a single quintuple-layer of Bi_2Te_3 to the predictions of the analytic octic dispersion model. For the latter, we have chosen as parameter values $a = 1$, $b = 2$ and $\epsilon_0 = 0.16$ eV.

of the three scattering approximations for the Bi_2Te_3 QL system as well, a hypothesis which is confirmed by plotting the resulting figures-of-merit, shown in Figure 4.15.

We note that the material performs considerably better when p-doped than when it is n-doped. This is due to the large number of conduction channels provided by the ring-like valence bands, compared to the more typical Kane-like conduction band. This trend will hold for all the quintuple-layer systems analyzed, and as such, our analysis will focus solely on the thermoelectic properties of the valence states. More importantly, we have found that the presence of a moat-like dispersion feature can lead to abrupt decreases in $D(E)$ and increases in V_λ, both of which are desirable for efficient thermoelectric conversion. As such, quintuple-layered Bi_2Te_3 may be an even better thermoelectric material than previous studies (which have limited themselves to less accurate scattering models) have suggested.

4.3.2 Bi_2Se_3 QL

Next, we analyze the thermoelectric performance of a single quintuple-layer of Bi_2Se_3. The band structure of this material is shown in Figure 4.16, while the resulting electronic properties are shown in Figure 4.17. We note that the uppermost valence band

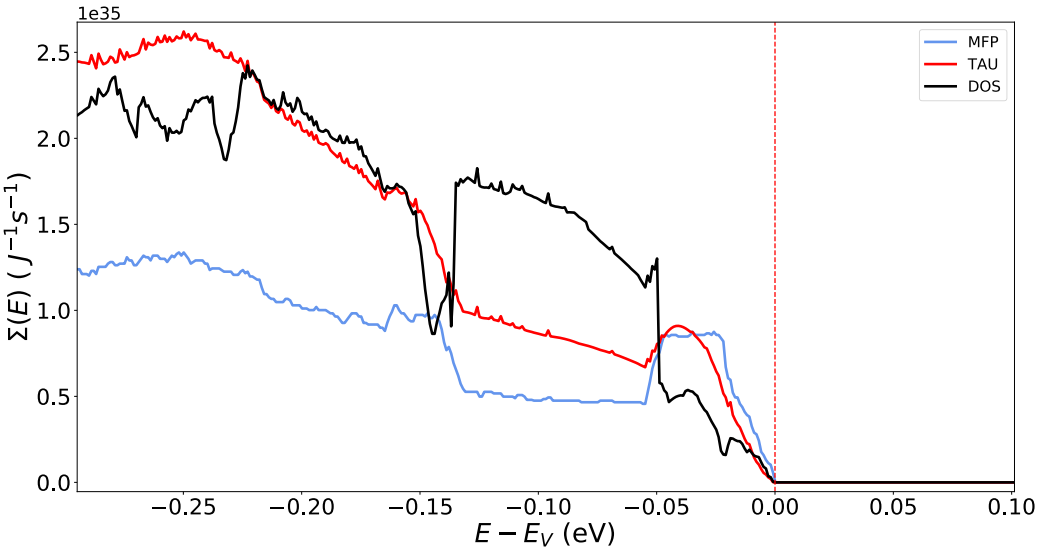

Figure 4.14: Transport distributions vs. energy level (relative to the valence band edge) of a single-QL of Bi_2Te_3, for the constant-MFP, constant-TAU and DOS-scattering models. The scattering constants for the conduction and valence states are set separately such that $\langle\langle\lambda\rangle\rangle_{\mu=E_v} = \langle\langle\lambda\rangle\rangle_{\mu=E_c} = 10$ nm.

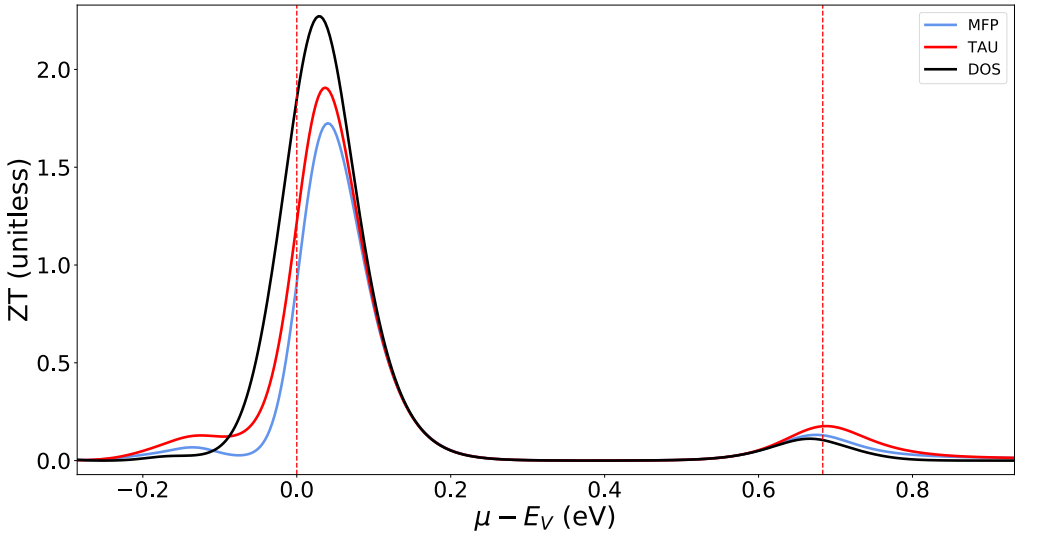

Figure 4.15: Figures-of-merit predicted by the constant-MFP, constant-TAU, and DOS-scattering models when applied to a single quintuple-layer of Bi_2Te_3. The band gap shown has been adjusted to match the GW value.

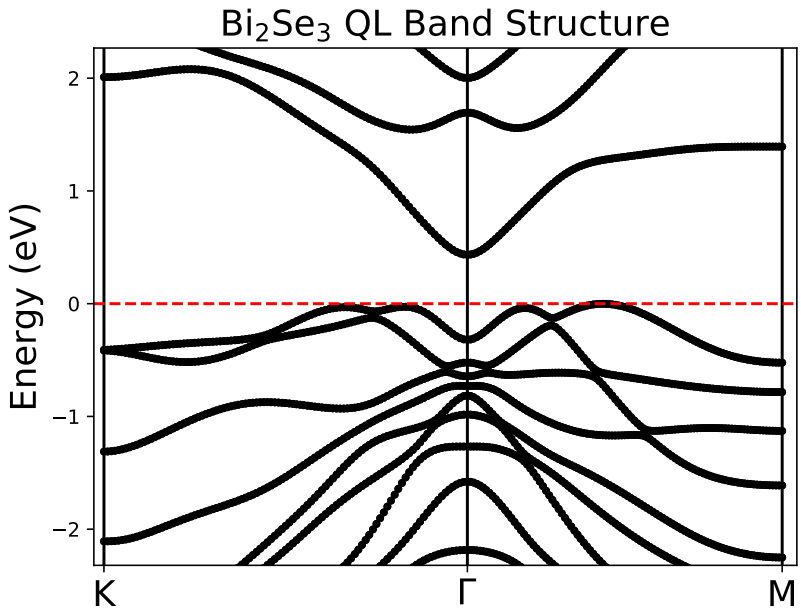

Figure 4.16: Band structure of a single quintuple-layer of Bi_2Se_3, along the high-symmetry points of the 2D hexagonal Brillouin zone. $E = 0$ corresponds to the valence band edge, and the band gap shown is the un-adjusted PBE band gap obtained via DFT.

of this material possesses two ring-like features at the band-edge, analogous to the Bi_2Te_3 case just discussed. As before, this results in a step-like increase in $M(E)$ at the band-edge. However, unlike the previous case, we do not observe discontinuities in $M(E)$ and $V_\lambda(E)$ at energies below the band-edge. To understand why these features are absent, we plot the constant energy contours for energies near the valence band edge in Figure 4.18.

While we still see two ring-like features near the band edge, with a moat feature nested between them, this particular moat feature is highly anisotropic, as indicated by the presence of multiple lower-energy valleys within the main ring feature. This anisotropy results in a 'washing out' of the sharp features that would have resulted from a more isotropic moat feature. The resulting transport distributions are shown in Figure 4.19. We can see that there is a distinct lack of sharp features in any of the transport distributions, as a consequence of the observed anisotropy. Nevertheless, the DOS-scattering transport distribution still takes on the largest value over a significant portion of the relevant energy range. The corresponding figures-of-merit

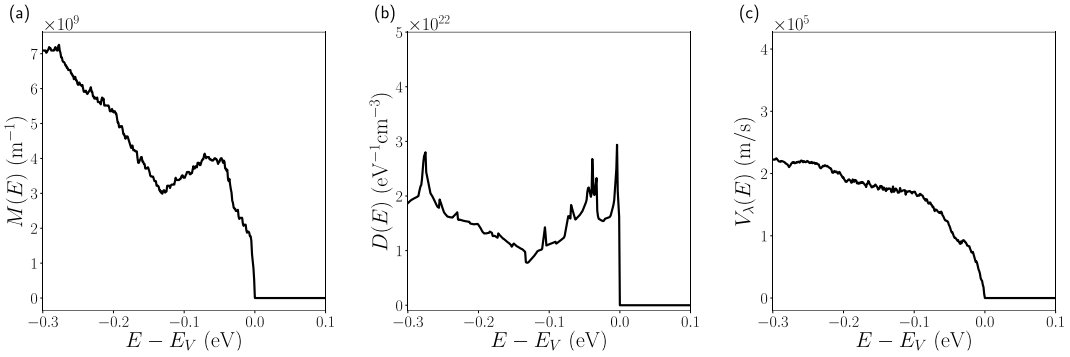

Figure 4.17: Electronic properties of a single quintuple-layer of Bi_2Se_3. Plotted are the (a) distribution-of-modes, (b) density-of-states and (c) average velocity distributions, all vs. energy level (relative to the valence band edge).

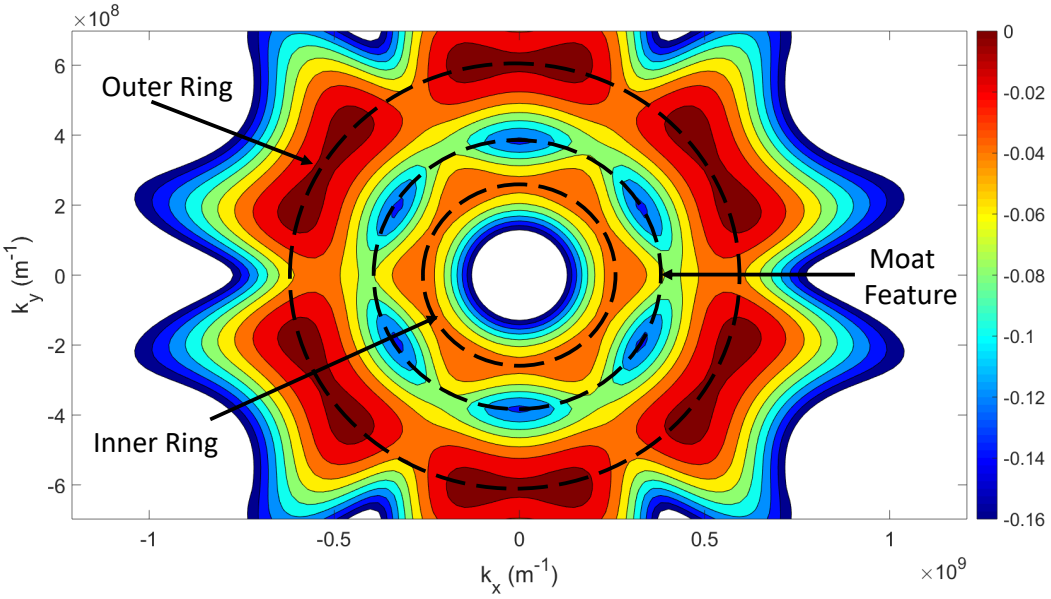

Figure 4.18: Constant energy contours for the uppermost valence band of a single quintuple-layer of of Bi_2Se_3. Energies are given in units of eV, and $E = 0$ corresponds to the valence band edge.

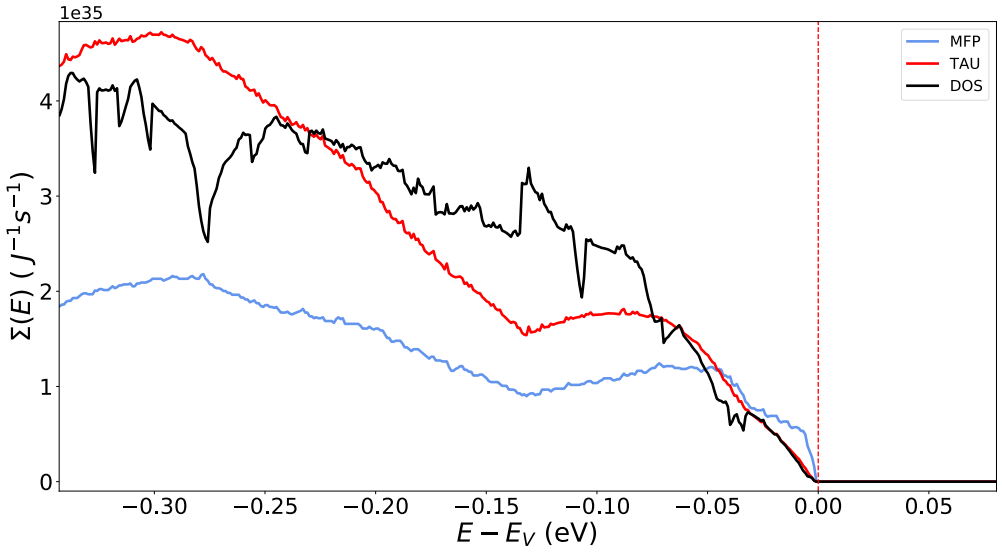

Figure 4.19: Transport distributions vs. energy level (relative to the valence band edge) of a single-QL of Bi_2Se_3, for the constant-MFP, constant-TAU and DOS-scattering models. The scattering constants for the conduction and valence states are set separately such that $\langle\langle\lambda\rangle\rangle_{\mu=E_v} = \langle\langle\lambda\rangle\rangle_{\mu=E_c} = 10$ nm.

are shown in Figure 4.20.

As was found for the Bi_2Te_3 QL system, the DOS scattering model predicted the largest figure-of-merit of the three scattering models considered. However, the relative improvement is not nearly as significant in this case, indicating that the performance enhancements that arise from moat-like dispersion features are highly sensitive to the degree of anisotropy.

4.3.3 Sb_2Te_3 QL

Next, we analyze the last of our single quintuple-layer systems, that of Sb_2Te_3. The band structure plot of a single quintuple-layer of this material is shown in Figure 4.21, while the resulting electronic properties are shown in Figure 4.22. While we still observe two ring-like features near the valence band edge, as was found for the two previous quintuple-layer systems, the $M(E)$, $D(E)$ and $V_\lambda(E)$ distributions display sharp features not found in the previous two cases. Namely, we observe large increases in the distribution-of-modes and density-of states roughly 0.03 eV below

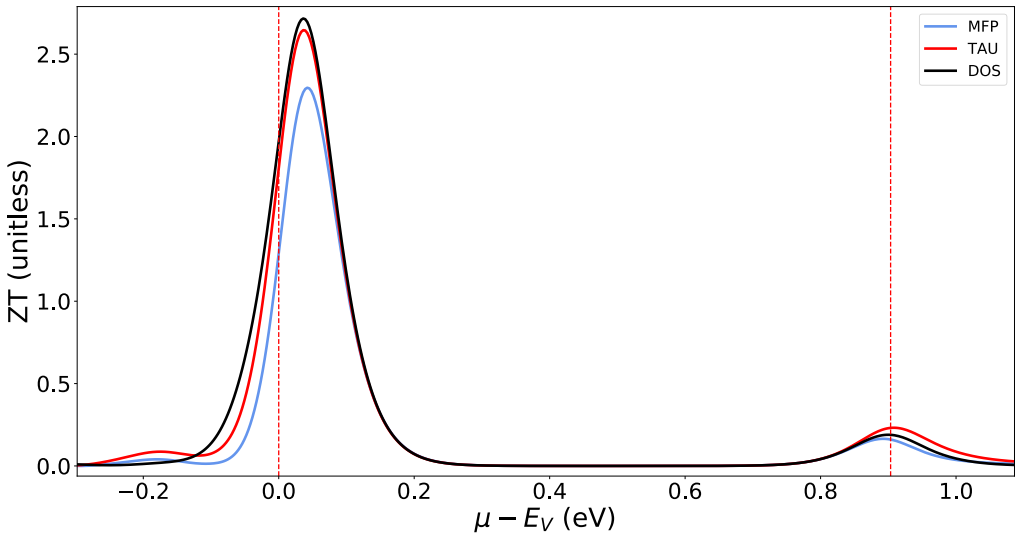

Figure 4.20: Figures-of-merit predicted by the constant-MFP, constant-TAU, and DOS-scattering models when applied to a single quintuple-layer of Bi_2Se_3. The band gap shown has been adjusted to match the GW value.

the band-edge, and a sharp decrease in $V_\lambda(E)$ at the same point. To understand the origin of these features, we plot the constant energy contours for energies near the valence band edge in Figure 4.23.

Unlike the case of Bi_2Te_3, wherein the inner and outer rings turned on at very nearly the same energy (*i.e.* the band edge), we can see that in Sb_2Te_3 the outer ring turns on at a slightly lower energy. The sudden 'turn-on' of this ring feature results in a large increase in the number of available states, causing the abrupt increases in $M(E)$ and $D(E)$ shown in Figure 4.22. Because the states near the top of the outer ring feature have very small velocities, their sudden 'turn-on' also drags down the average velocity of states at that energy, causing the abrupt decrease in $V_\lambda(E)$. As such, this offset outer ring feature has essentially the exact opposite impact of the moat feature in Bi_2Te_3. In the latter case, the abrupt turn-*off* of a ring-like dispersion feature caused sharp decreases in $M(E)$ and $D(E)$, and a sharp increase in $V_\lambda(E)$, whereas in this case the abrupt turn-*on* of a ring like feature has the exact opposite effect. The resulting transport distributions are shown in Figure 4.24.

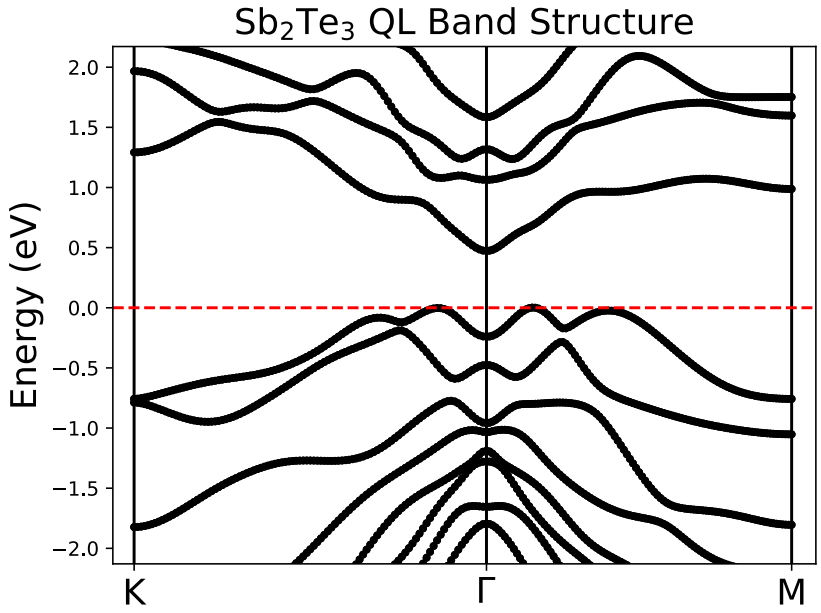

Figure 4.21: Band structure of a single quintuple-layer of Sb_2Te_3, along the high-symmetry points of the 2D hexagonal Brillouin zone. $E = 0$ corresponds to the valence band edge, and the band gap shown is the un-adjusted PBE band gap obtained via DFT.

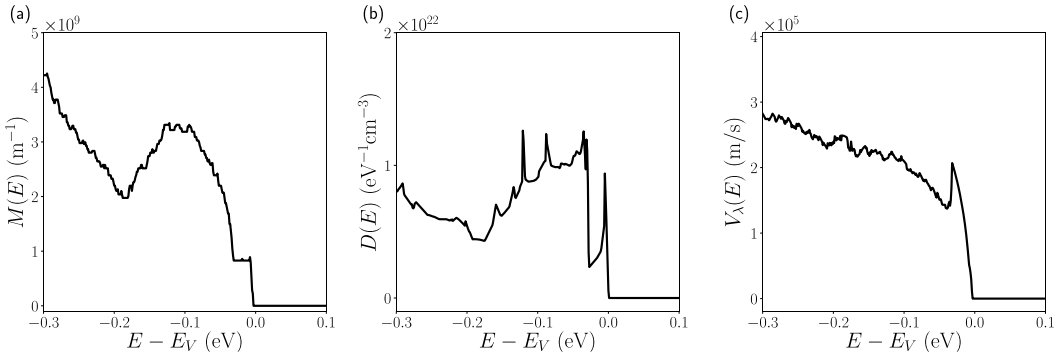

Figure 4.22: Electronic properties of a single quintuple-layer of Sb_2Te_3. Plotted are the (a) distribution-of-modes, (b) density-of-states and (c) average velocity distributions, all vs. energy level (relative to the valence band edge).

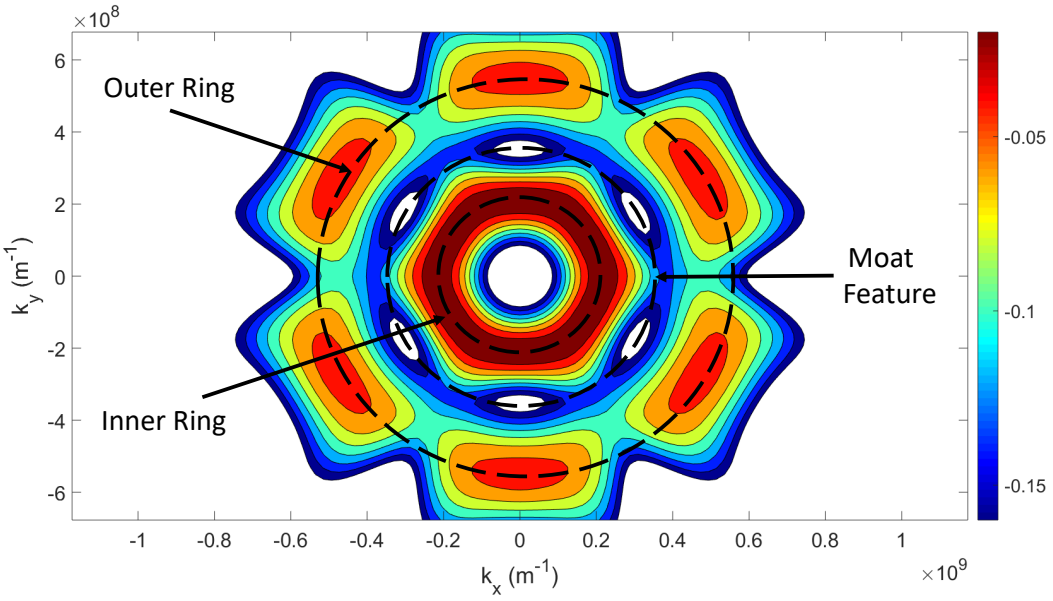

Figure 4.23: Constant energy contours for the uppermost valence band of a single quintuple-layer of Sb_2Te_3. Energies are given in units of eV, and $E = 0$ corresponds to the valence band edge.

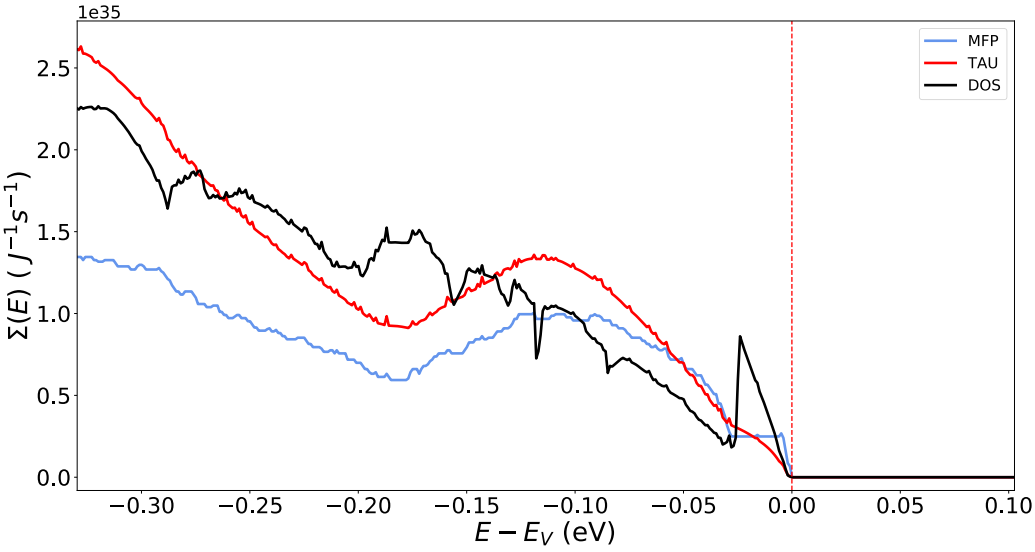

Figure 4.24: Transport distributions vs. energy level (relative to the valence band edge) of a single-QL of Sb_2Te_3, for the constant-MFP, constant-TAU and DOS-scattering models. The scattering constants for the conduction and valence states are set separately such that $\langle\langle\lambda\rangle\rangle_{\mu=E_v} = \langle\langle\lambda\rangle\rangle_{\mu=E_c} = 10$ nm.

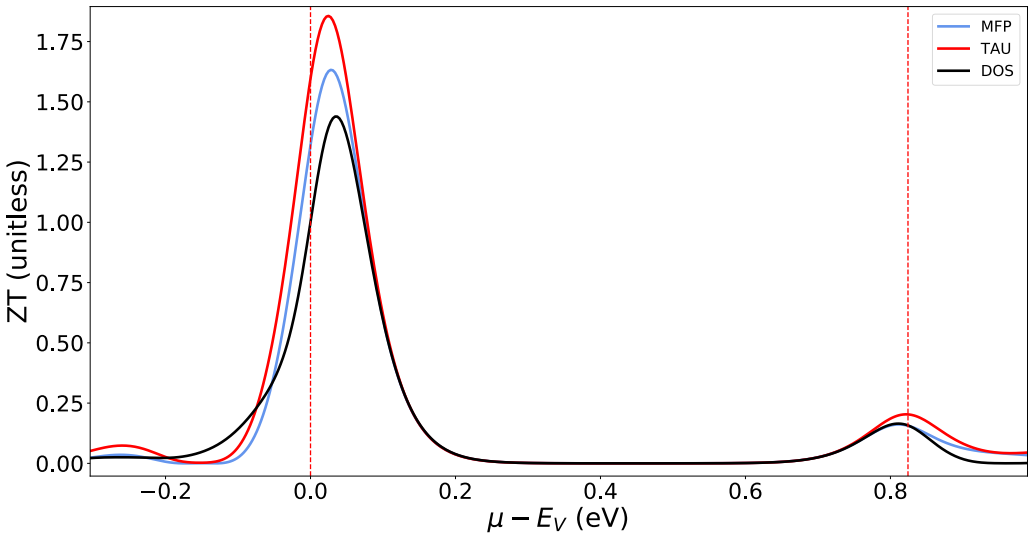

Figure 4.25: Figures-of-merit predicted by the constant-MFP, constant-TAU, and DOS-scattering models when applied to a single quintuple-layer of Sb_2Te_3. The band gap shown has been adjusted to match the GW value.

While the DOS-scattering transport distribution takes on the largest values for energies very near the band-edge, the increased scattering and decreased average velocity that result from the turn-on of the outer ring feature cause the transport distribution to abruptly step downwards at $E = -0.03$ eV. As a result, it takes on the smallest value of the three transport distributions over a significant portion of the relevant energy range. The corresponding figures-of-merit are shown in Figure 4.25.

We can see that in this case DOS-scattering predicts the worst performance of the three scattering approximations. This shows that the thermoelectric performance of these quintuple-layered systems is sensitive not just to the anisotropy of the moat feature (as was found in the Bi_2Se_3 case), but also to the relative alignment of the inner and outer ring features.

4.4 Double Quintuple-layers

In this section, we investigate the thermoelectric properties of double-quintuple-layer systems, *i.e.* the 2D systems obtained from cleaving ten atomic layers from the bulk rhomohedral structures instead of just five. As such, the primitive cell contains ten atoms. The crystal structures of these systems are extremely similar to those of the

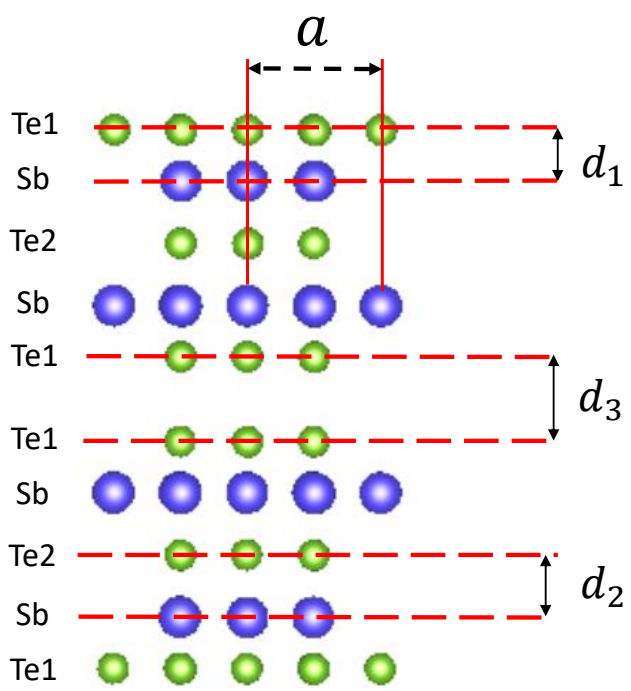

Figure 4.26: Structural diagram of the primitive cell of a double-QL material.

corresponding single-QL systems: the main difference is that one must introduce a third inter-layer spacing variable, d_3, that describes the (relatively large) separation between Te1 layers, *i.e.* between the two single-QLs making up the double-QL, as illustrated in Figure 4.26. Again, the atomic coordinates are entirely determined by the bulk structure. The values of the structural parameters used in our DFT calculations are provided in Table 4.3.

Material	a (Å)	d_1 (Å)	d_2 (Å)	d_3 (Å)	DFT Gap (eV)	GW Gap (eV)
Bi_2Se_3	4.138	1.596	1.895	2.523	0.09	0.24
Bi_2Te_3	4.383	1.751	2.053	2.702	0.046	0.06
Sb_2Te_3	4.260	1.714	1.983	2.916	0.16	0.25

Table 4.3: Structural parameters used in DFT simulations of hexagonal double-QL materials.

4.4.1 Bi_2Se_3 2QL

We begin our analysis of the double quintuple-layer systems with the case of Bi_2Se_3. The band structure of this material is shown in Figure 4.27. Since only states within

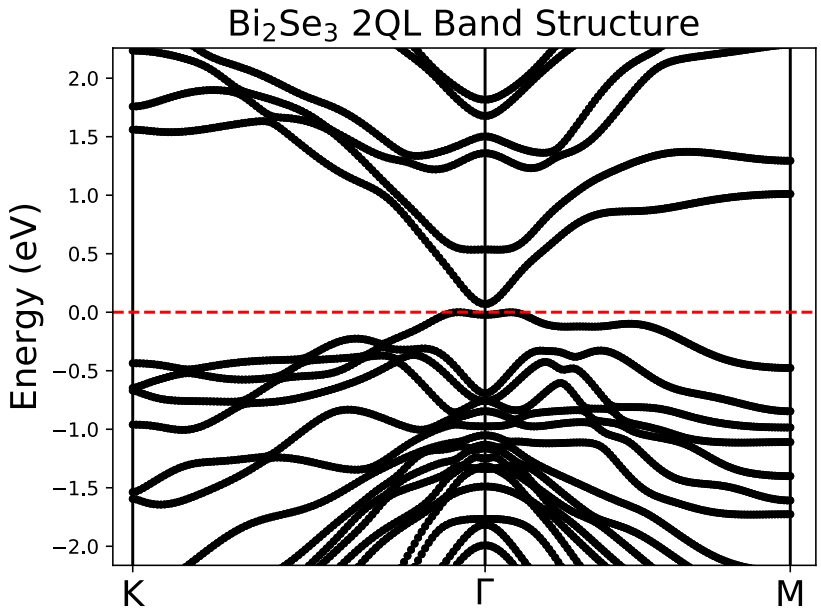

Figure 4.27: Band structure of a double quintuple-layer of Bi_2Se_3, along the high-symmetry points of the 2D hexagonal Brillouin zone. $E = 0$ corresponds to the valence band edge, and the band gap shown is the un-adjusted PBE band gap obtained via DFT.

roughly 0.25 eV of the band edge will make a significant contribution to transport, we can see that the uppermost valence band will dominate the transport properties of this material. We plot the constant energy contours of this band in Figure 4.28. Whereas the single QL systems have been characterized by the presence of two ring-like features near the band edge, this system has only a single such ring, and its diameter is considerably reduced from the single QL cases. In place of an outer ring feature, this double-QL system instead has a set of six identical valleys that turn on roughly 0.10 eV below the band-edge. The resulting electronic properties are shown in Figure 4.29.

While we still see a step-like feature in the DOM at the band-edge, the magnitude of this step is considerably smaller than in any of the single-QL cases, due to the reduced diameter of the ring feature. The turn-on of the six identical valleys at $E = -0.10$ eV causes large increases in the magnitude of $M(E)$ and $D(E)$ as well as a large decrease in the magnitude of $V_\lambda(E)$. As such, the impact of these valleys is qualitatively similar to that of the offset outer ring in Sb_2Te_3. Nevertheless, the resulting features in the electronic distributions of this double-QL system are somewhat

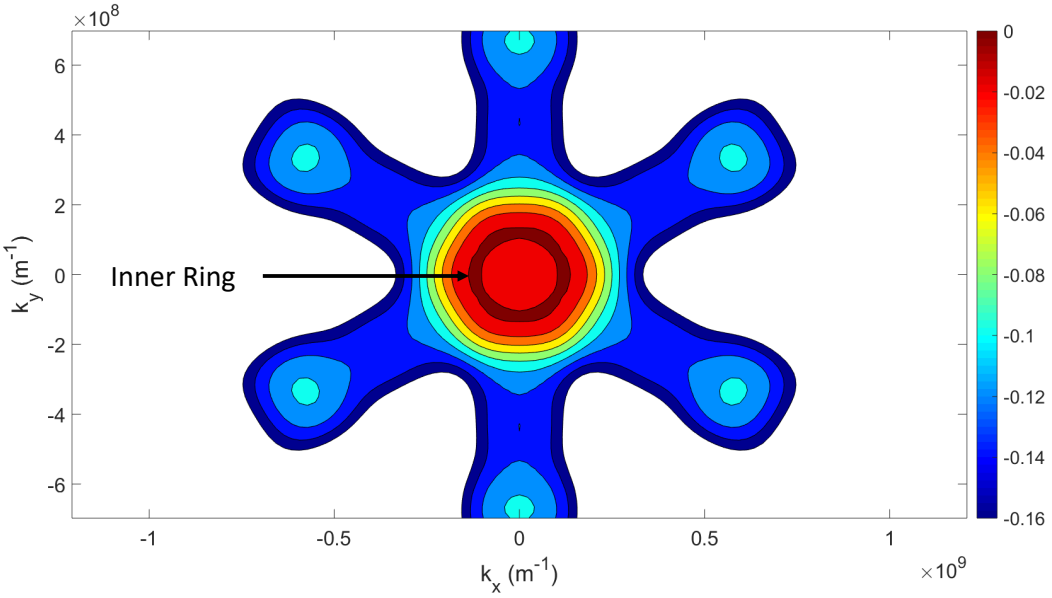

Figure 4.28: Constant energy contours for the uppermost valence band of a double quintuple-layer of Bi_2Se_3. Energies are given in units of eV, and $E = 0$ corresponds to the valence band edge.

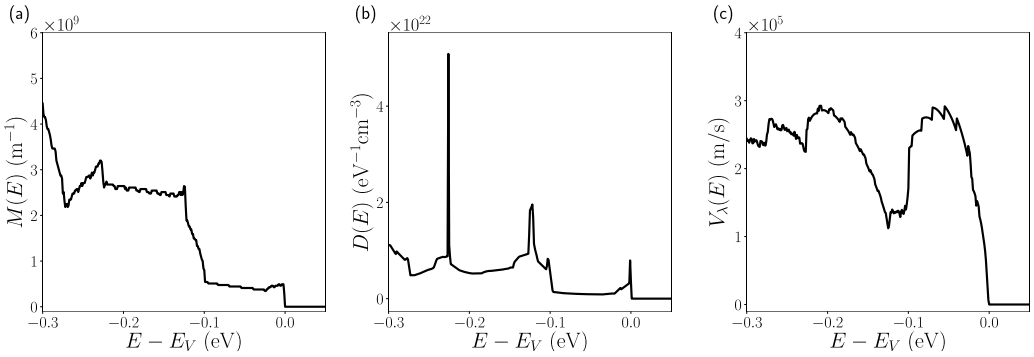

Figure 4.29: Electronic properties of a double quintuple-layer of Bi_2Se_3. Plotted are the (a) distribution-of-modes, (b) density-of-states and (c) average velocity distributions, all vs. energy level (relative to the valence band edge).

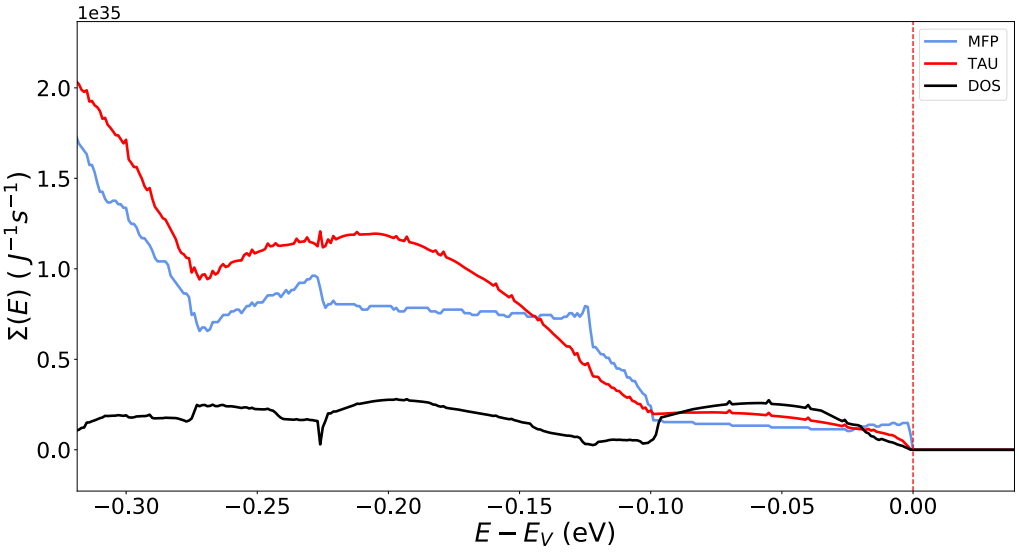

Figure 4.30: Transport distributions vs. energy level (relative to the valence band edge) of a double-QL of Bi_2Se_3, for the constant-MFP, constant-TAU and DOS-scattering models. The scattering constants for the conduction and valence states are set separately such that $\langle\langle\lambda\rangle\rangle_{\mu=E_v} = \langle\langle\lambda\rangle\rangle_{\mu=E_c} = 10$ nm.

less abrupt than those observed in the Sb_2Te_3 QL case. This is because the feature 'turning on' in this case is highly anisotropic, and thus the electronic features it gives rise to will be less sharp than those arising from more ring-like dispersion features. The resulting transport distributions are shown in Figure 4.30.

The resulting DOS scattering transport distribution is qualitatively similar to that of the Sb_2Te_3 QL case, in that the turn-on of a large dispersion feature causes the magnitude of the transport distribution to decrease, albeit less abruptly than in the previous case. The resulting figures-of-merit are shown in Figure 4.31.

We note that both the TAU and MFP models predict the existence of secondary ZT peaks of appreciable magnitude at energies below the valence band-edge. These are the result of large increases in the magnitude of the DOM distribution. However, as these large increases in DOM are accompanied by similarily large increases in the density-of-states (and hence large increases in scattering), the DOS scattering model predicts relatively poor thermoelectric performance when the Fermi level lies below

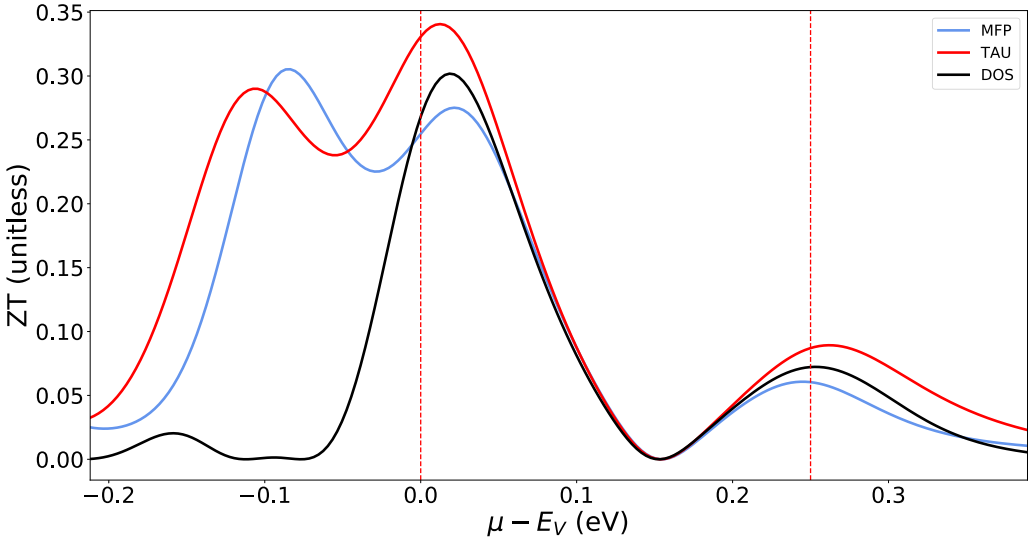

Figure 4.31: Figures-of-merit predicted by the constant-MFP, constant-TAU, and DOS-scattering models when applied to a double quintuple-layer of Bi_2Se_3. The band gap shown has been adjusted to match the GW value.

the valence band edge. For the ZT peaks that occurs for Fermi levels lying within the band gap, DOS-scattering predicts worse performance than the TAU model, but better performance than the MFP model. Nevertheless, the ZT values obtained are considerably smaller than those obtained for the corresponding single-QL system.

4.4.2 Sb_2Te_3 2QL

The features of a double quintuple-layer system of Sb_2Te_3 are qualitatively quite similar to those just discussed for double quintuple-layers of Bi_2Se_3. A band structure plot for this material is shown in Figure 4.32, while the constant energy contours of the uppermost valence band are shown in Figure 4.33. As with the Bi_2Se_3 2QL system, Sb_2Te_3 2QL is characterized by a small ring-like feature at the band-edge, and six identical valleys that turn on below the band-edge, this time at roughly $E = -0.08$ eV. The resulting electronic properties are shown in Figure 4.34, and the corresponding transport distributions and figures-of-merit are shown in Figures 4.35 and 4.36 respectively. In this case, DOS-scattering predicts the lowest peak-ZT value, which is due to the slightly earlier 'roll-off' of the DOS-scattering transport distribution, as compared to the Bi_2Se_3 2QL case. Again, we see large ZT values

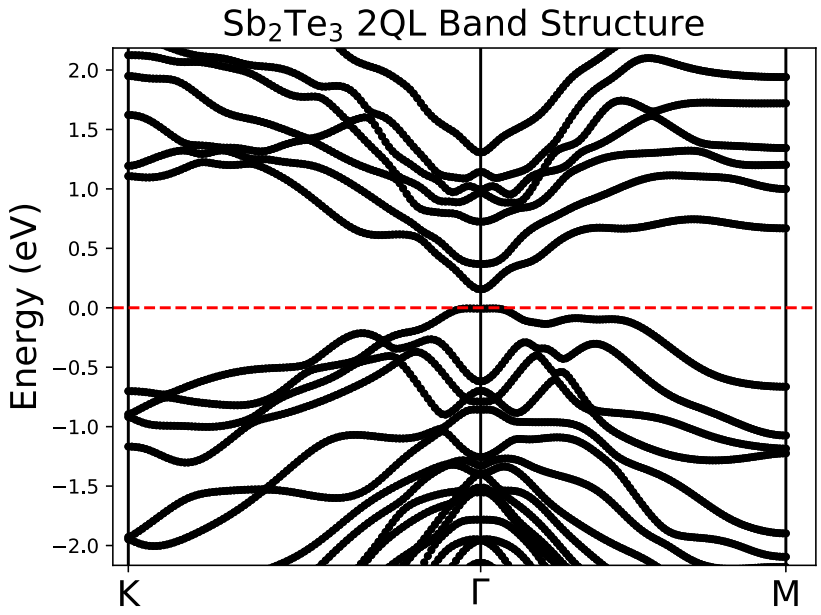

Figure 4.32: Band structure of a double quintuple-layer of Sb_2Te_3, along the high-symmetry points of the 2D hexagonal Brillouin zone. $E = 0$ corresponds to the valence band edge, and the band gap shown is the un-adjusted PBE band gap obtained via DFT.

at Fermi levels below the VBM for both the MFP and TAU models, but not for the DOS-scattering model, due to the increased scattering that results from the larger number of available states.

4.4.3 Bi_2Te_3 2QL

Lastly, we analyze the thermoelectric properties of our final double-QL system, that of Bi_2Te_3. The band structure of this material is shown in Figure 4.37. We again find that the uppermost valence band will dominate transport properties, but the electronic structure of this band is qualitatively different from that of the uppermost valence bands of the two previous systems, as shown in Figure 4.38. In this case, the constant energy surfaces take on a distinctive 'starfish' shape (albeit one with six arms instead of five). Furthermore, the secondary feature that 'turns-on' here is a single ring-like feature, not multiple isolated valleys, and it does so at a lower energy (roughly $E = -0.18$ eV) than in either of the Bi_2Se_3 2QL or Sb_2Te_3 2QL cases. The resulting electronic properties are shown in Figure 4.39.

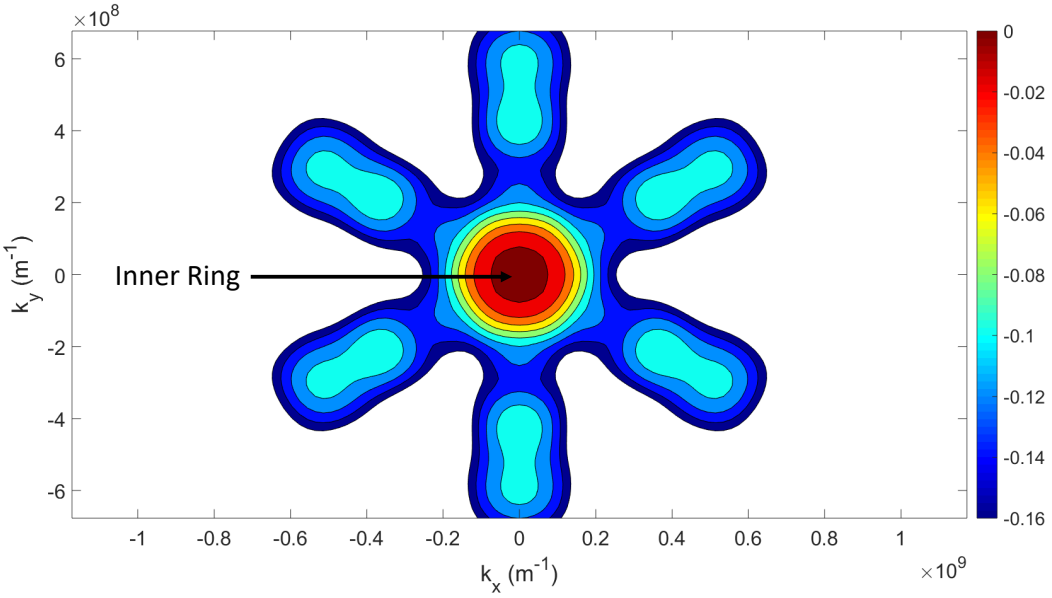

Figure 4.33: Constant energy contours for the uppermost valence band of a double quintuple-layer of Sb_2Te_3. Energies are given in units of eV, and $E = 0$ corresponds to the valence band edge.

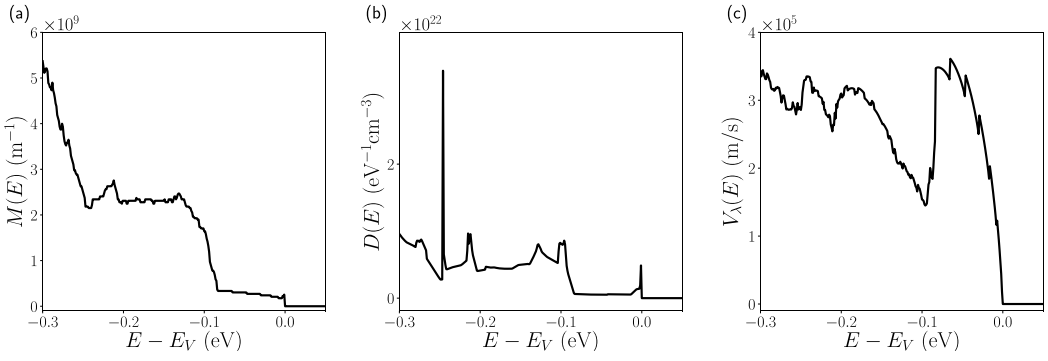

Figure 4.34: Electronic properties of a double quintuple-layer of Sb_2Te_3. Plotted are the (a) distribution-of-modes, (b) density-of-states and (c) average velocity distributions, all vs. energy level (relative to the valence band edge).

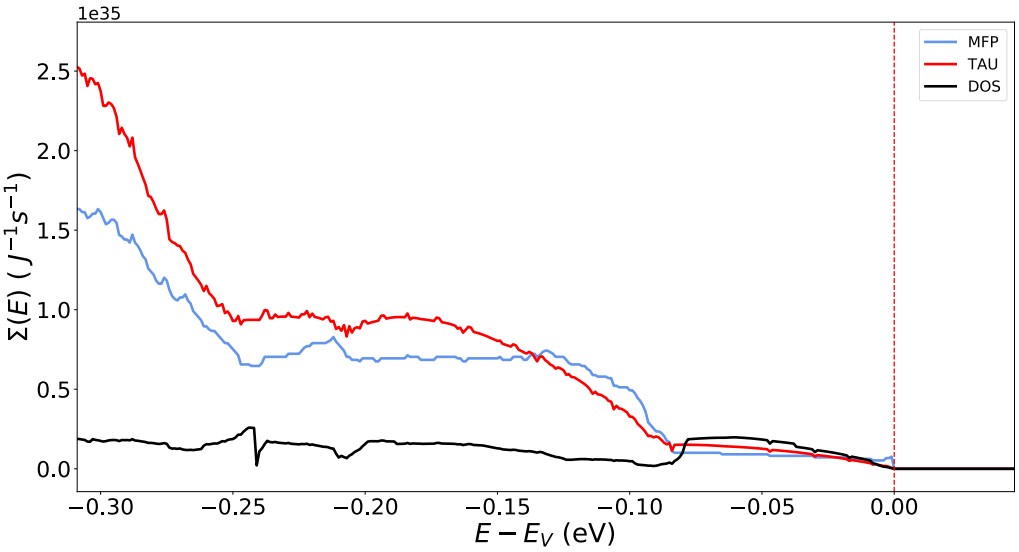

Figure 4.35: Transport distributions vs. energy level (relative to the valence band edge) of a double-QL of Sb_2Te_3, for the constant-MFP, constant-TAU and DOS-scattering models. The scattering constants for the conduction and valence states are set separately such that $\langle\langle\lambda\rangle\rangle_{\mu=E_v} = \langle\langle\lambda\rangle\rangle_{\mu=E_c} = 10$ nm.

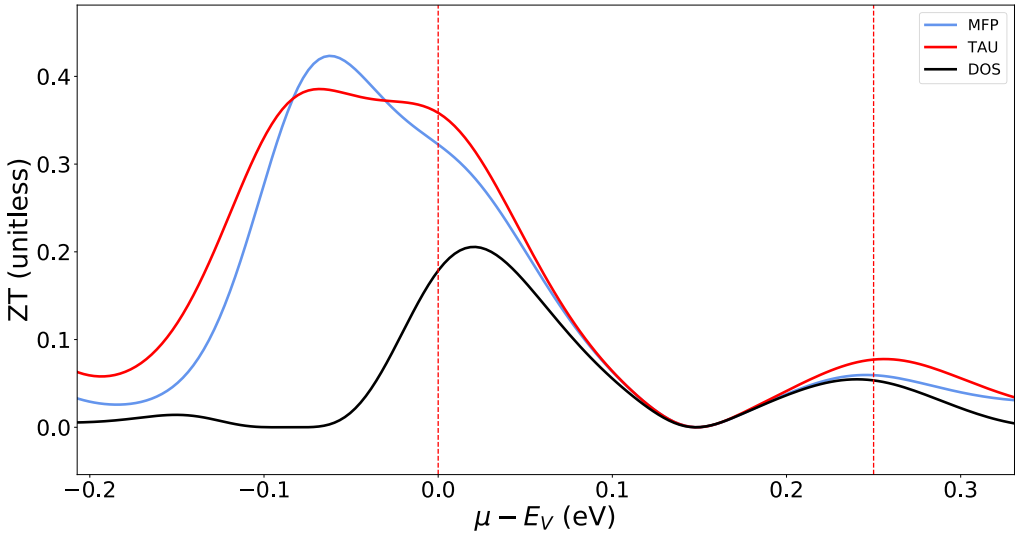

Figure 4.36: Figures-of-merit predicted by the constant-MFP, constant-TAU, and DOS-scattering models when applied to a double quintuple-layer of Sb_2Te_3. The band gap shown has been adjusted to match the GW value.

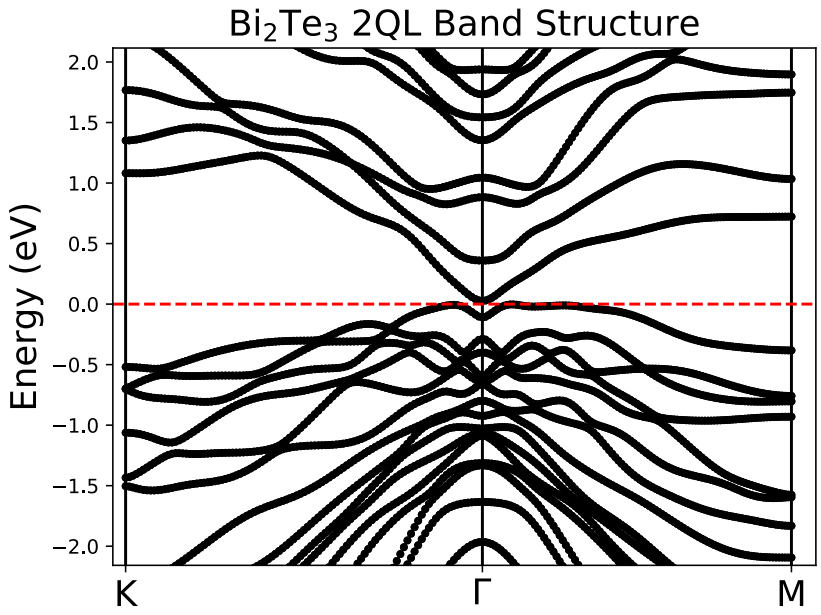

Figure 4.37: Band structure of a double quintuple-layer of Bi_2Te_3, along the high-symmetry points of the 2D hexagonal Brillouin zone. $E = 0$ corresponds to the valence band edge, and the band gap shown is the un-adjusted PBE band gap obtained via DFT.

The resulting transport distributions are shown in Figure 4.40, and the corresponding figures-of-merit are shown in Figure 4.41. In this case, DOS scattering predicts the greatest TE performance of the three models, which we attribute to the fact that the 'roll-off' of the DOS-scattering transport distribution occurs deeper into the valence band than in either of the two previous cases. As a result, the DOS-scattering transport distribution has the largest magnitude over the majority of the relevant energy range. The secondary ZT peaks below the valence band edge that occur for the constant-MFP and constant-TAU models considerably weaker in this case, as the dispersion features that produce them turn on at lower energies for double-QL Bi_2Te_3 than for either of the previous two systems. We note that due to the small band gap of this material, there are no ZT peaks near the conduction band edge, due to the detrimental effects of bipolar conduction. When the band gap is small, valence states make a non-negligible contribution to transport even when the Fermi level lies near the conduction band edge. This lowers the magnitude of the Seebeck coefficient, as the positive contributions to the I_1 integral made by the conduction

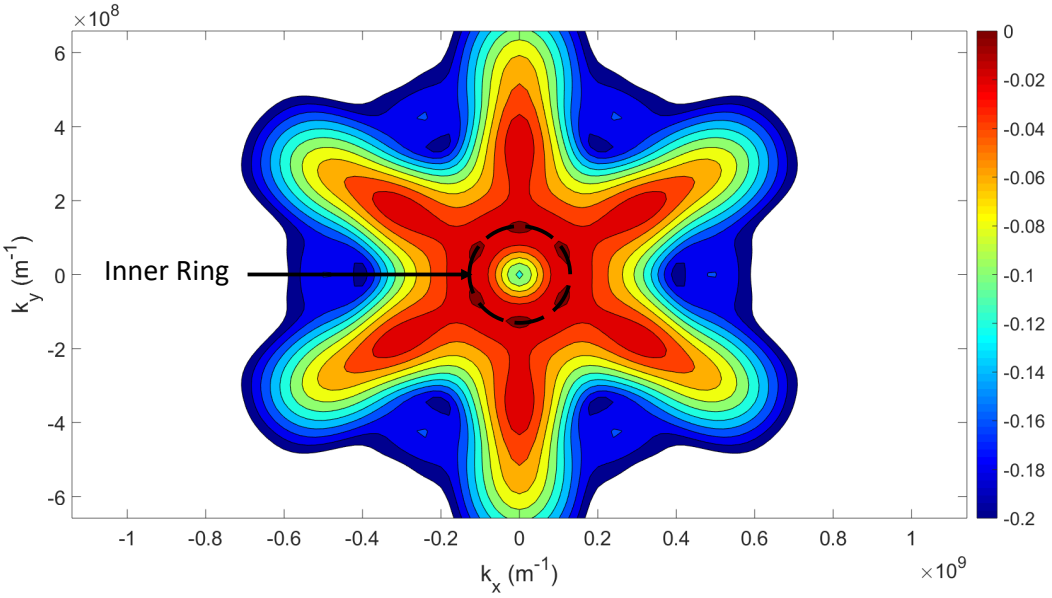

Figure 4.38: Constant energy contours for the uppermost valence band of a double quintuple-layer of Bi_2Te_3. Energies are given in units of eV, and $E = 0$ corresponds to the valence band edge.

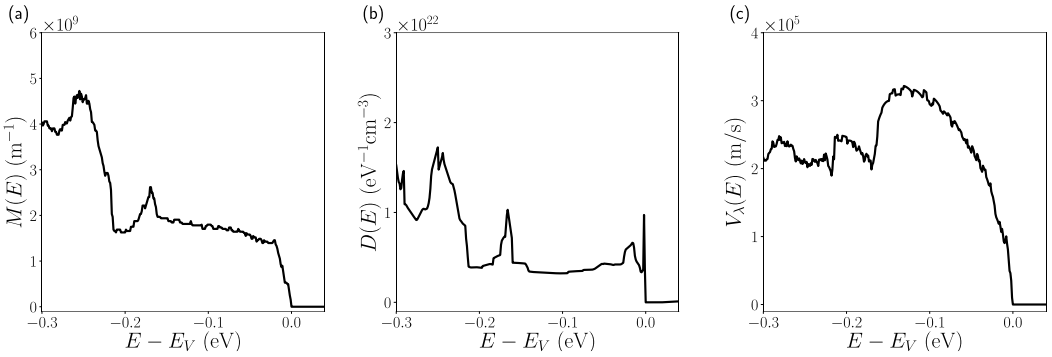

Figure 4.39: Electronic properties of a double quintuple-layer of Bi_2Te_3. Plotted are the (a) distribution-of-modes, (b) density-of-states and (c) average velocity distributions, all vs. energy level (relative to the valence band edge).

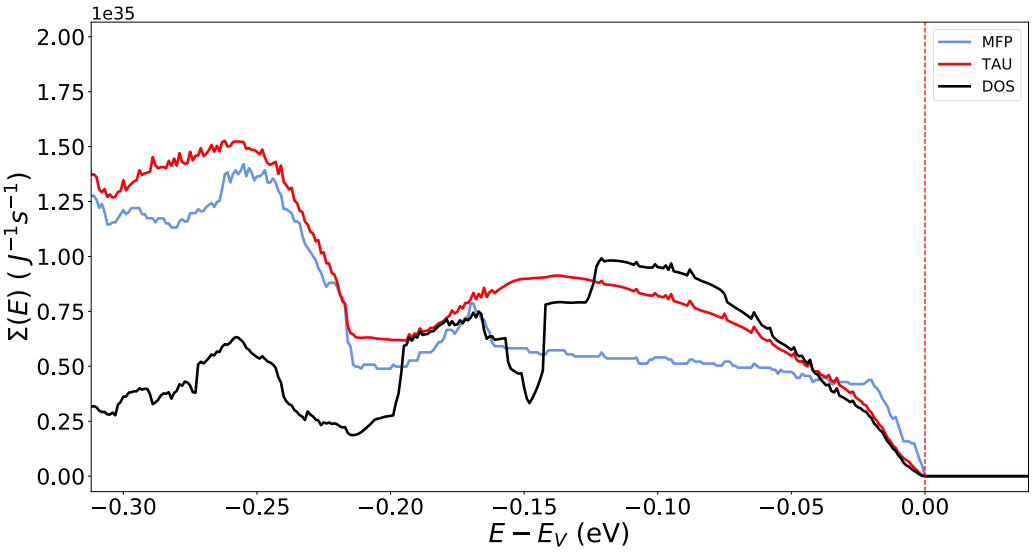

Figure 4.40: Transport distributions vs. energy level (relative to the valence band edge) of a double-QL of Bi_2Te_3, for the constant-MFP, constant-TAU and DOS-scattering models. The scattering constants for the conduction and valence states are set separately such that $\langle\langle\lambda\rangle\rangle_{\mu=E_v} = \langle\langle\lambda\rangle\rangle_{\mu=E_c} = 10$ nm.

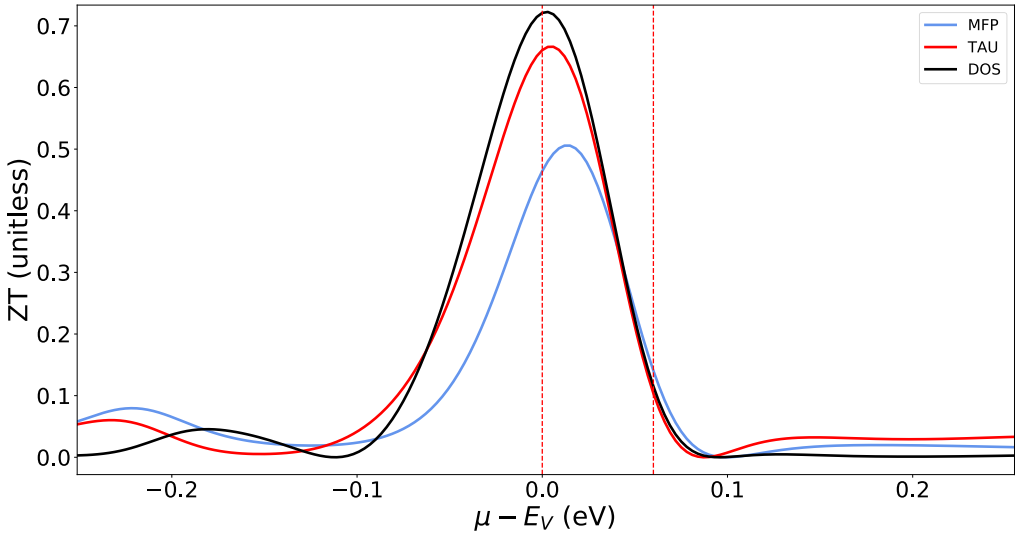

Figure 4.41: Figures-of-merit predicted by the constant-MFP, constant-TAU, and DOS-scattering models when applied to a double quintuple-layer of Bi_2Te_3. The band gap shown has been adjusted to match the GW value.

states are partially canceled out by the negative contribution from the valence states.

In this chapter, we have calculated the electronic dispersions of single and double quintuple-layered systems of Bi_2Te_3, Bi_2Se_3 and Sb_2Te_3 from first-principles, and determined their resultant thermoelectric properties using the constant-TAU, constant-MFP and DOS-scattering approximations. These materials are of interest due to the ring-like features in their valence bands, which have significant and interesting effects on their electronic properties. For single-QL Bi_2Te_3, we find that the presence of a nearly isotropic moat-like feature in the electronic dispersion results in the DOS scattering model predicting significantly enhanced thermoelectric performance. These enhancements are due to the sharp increases in $V_\lambda(E)$ and decreases in scattering rates that result from this feature, as shown by our new analytic octic model of electronic dispersion. Single-QL Bi_2Se_3 possesses a similar, but more anisotropic moat feature, and as a consequence the DOS-scattering model predicts only minor improvements. In the case of Sb_2Te_3, a slight energetic offset between the inner and outer ring features was found to have the opposite effect of the Bi_2Te_3 moat feature, and resulted in the DOS-scattering model predicting the worst thermoelectric performance of all three scattering approximations. Double-QL systems of these materials were also investigated, but were found to be inferior to their single-QL counterparts in all cases due to energetic offsets between their main dispersion features, as well as the reduced magnitude of their $M(E)$ dispersions near the valence band edge.

Our results show that materials possessing an isotropic moat feature similar to that of single-QL Bi_2Te_3 may be significantly better thermoelectrics than previous studies (which have made use of cruder scattering approximations) have found. This motivates a revisitation of previous studies on similar warped band materials, as a more accurate treatment of carrier scattering may significantly change the predicted performance. However, the resulting performance benefits we have found are highly sensitive to the degree of anistropy in the moat feature, as well as to the energetic alignment of the other ring-like dispersion features. This motivates future work focused on quantifying the impact that deviations from isotropicity have on the thermoelectric properties, *e.g.* via a generalization of our isotropic octic model.

Another avenue for future work would be a benchmarking of the accuracy of the DOS-scattering approximation vs. rigorous scattering approximations when applied to materials with warped valence bands, as such studies have primarily focused on materials with less exotic band structures [22, 27, 28].

Chapter 5

Conclusion

In this work, we have investigated the extent to which the predictions of the constant-mean-free path and constant-relaxation time approximations differ from those of the more physical DOS scattering model. In Chapter 2, after an overview of the Landauer theory of thermoelectric transport, we provide the definitions of the transport distributions of these scattering models, which take on different functional forms depending on the scattering approximation being implemented. No matter which of the three approximations is chosen, the resulting transport distributions are (up to a constant scaling factor) functions only of quantities that can be calculated directly from the electronic dispersion, namely $M(E)$, $D(E)$ and $V_\lambda(E)$. We outline the methods used for calculating these quantities from of analytic models of electronic dispersion, as well as from numerically resolved electronic dispersions, such as those obtained from first-principles DFT calculations.

In Chapter 3, we have investigated the predictions of these three scattering models when applied to common analytic models of electronic band structure. It is found that not only can the predicted magnitudes of thermoelectric quantities such as the electronic power factor differ significantly between models, the models can even disagree about whether a particular electronic dispersion feature should lead to improved thermoelectric performance. While such disagreements can occur in dispersions as simple as the Kane model, wherein the models were found to disagree about the impact of 'linearizing' the band structure, the most pronounced differences between models occur for warped electronic dispersions, such as those described by the so-called 'quartic-band' model of electronic dispersion. In the quartic-band model, arguably the most widely used analytic model for describing warped bands, it was found the DOS scattering model predicted the existence of a second peak in the electronic power factor, as a consequence of a discontinuity in the density-of-states distribution.

Within the DOS-scattering model, this abrupt change in the electronic DOS leads to an abrupt decrease in the electronic scattering rates, an effect that both the MFP and TAU models fail to describe. This decrease in scattering results in an abrupt increase in the magnitude of the transport distribution, a feature that is highly desirable for thermoelectric performance, and which results in larger thermoelectric power-factor values than previous studies (making use of simpler scattering models) have found.

In light of this finding, in Chapter 4 we have investigated the predictions of these three scattering models when applied to the electronic dispersions of single and double quintuple-layered systems of Bi_2Te_3, Sb_2Te_3 and Bi_2Se_3, which have been obtained via first-principles DFT calculations. The valence bands in these materials have been shown to display a considerable degree of warping, but to date have only been investigated using the simplified constant-mean-free-path or constant-relaxation-time approximations. Our analysis represents the first investigation of these materials using the more physical DOS scattering approximation. We find that in addition to two ring-like critical energy surfaces near the band edges (similar to the single ring feature described by the quartic-band model), these materials also possess a third 'moat-like' critical energy surface that significantly impacts their thermoelectric properties. To provide insight into the consequences of this moat, we have introduced a new simple model of electronic dispersion capable of qualitatively describing the impact of such dispersion features, which are shown to lead to abrupt decreases in scattering rate, and sharp increases in average velocity, both of which are desirable for efficient thermoelectric conversion.

It is found that when the scattering rates of these quintuple-layered materials are approximated using the more physical DOS-scattering model, they can exhibit ZT values greater than those predicted by either the constant-mean-free-path or constant-relaxation-time approximations, suggesting that these materials may be even better thermoelectrics than was previously suggested. However, we also find that these performance enhancements are highly sensitive to the anisotropy of the critical surfaces, as well as to their relative energetic alignments. While the Bi_2Te_3 1QL system demonstrated significantly enhanced performance due to its nearly isotropic moat

feature, the Bi_2Se_3 1QL system exhibited only minor improvements due to its highly anisotropic moat. For the Sb_2Te_3 1QL system, the fact that the outer ring-like feature turned on at an energy slightly below the band edge caused a significant increase in scattering rate for states within the transport window, resulting in decreased performance when compared to the predictions of the simpler scattering models. As such, an extension of our new analytic model to allow for a quantitative description of the impact of critical surface anisotropy/alignment would be of immediate use to researchers, and thus represents a obvious avenue for future work. A rigorous calculation of the electron-phonon scattering rates for the single-QL materials would also be a worthwhile venture, as the true scattering rate distribution is unlikely to possess features as sharp as those predicted by the DOS-scattering model, and therefore our results should be thought of as an upper bound on potential performance. A quantitative description of the extent to which the predictions of the DOS scattering model differ from more rigorous scattering calculations when applied to materials with warped electronic dispersions is an important piece of information that has yet to be determined.

This work has shown that despite the omnipresence of the constant-relaxation-time and constant-mean-free-path approximations in the thermoelectric literature, their predictions can nevertheless differ significantly from those obtained from models implementing more accurate descriptions of the energy-dependence of the electronic scattering rates (*e.g.* the DOS-scattering approximation). Although a great deal of effort is often put into accurately resolving the band structure of candidate thermoelectric materials, we find that an oversimplified treatment of scattering can have a major effect on the predicted performance, drowning out the effects of any minor changes in electronic structure. These findings highlight the need for a more careful treatment of scattering in future studies, particularly when investigating materials with warped electronic bands, wherein the electronic DOS (and hence scattering rates) can exhibit large changes in magnitude over very small energy ranges. The abrupt decreases in DOS observed in these materials are found to be highly desirable features for thermoelectric performance, a fact which is overlooked by simpler scattering models. This suggests the possibility of a new strategy for engineering band

structures that exhibit similar features (namely large decreases in DOS while maintaining large values of $M(E)$ and $V_\lambda(E)$). This new design strategy runs contrary to that of some previous studies that focused on increasing $D(E)$ as much as possible, an approach that we find does not lead to enhanced performance *per se* once the resulting increase in scattering rates is taken into account.

Bibliography

[1] Jan-Hendrick Pohls. *Ultralow Thermal Conductivity and Novel Thermoelectric Materials*. PhD thesis, Dalhousie University, 2017.

[2] Lawrence Livermore National Laboratories. Estimated u.s. energy consumption in 2018. `https://flowcharts.llnl.gov/content/assets/docs/2018_United-States_Energy.pdf`. Accessed: 2019-11-21.

[3] G. J. Snyder and E. S. Toberer. Complex thermoelectric materials. *Nature Materials*, **7**, 105, (2008).

[4] C. Shao and H. Bao. Ueber die magnetische polarisation der metalle und erze durch temperatur-differenz. *Annalen der Physick*, **82**, 133-160, (1826).

[5] Lars Onsager. Reciprocal relations in irreversible processes. i. *Physical Review*, **37**, 4, (1931).

[6] Lars Onsager. Reciprocal relations in irreversible processes. ii. *Physical Review*, **38**, 12, (1931).

[7] Mark Lundstrom and Changwook Jeong. *Near-equilibrium Transport: Fundamentals and Applications*. World Scientific, 2012.

[8] A. J. Minnich, H. Lee, X. W. Wang, G. Joshi, M. S. Dresselhaus, Z. F. Ren, G. Chen, and D. Vashaee. Modeling study of thermoelectric SiGe nanocomposites. *Physical Review B*, **80**, 155327, (2009).

[9] Y. Pei, X. Shi, A. LaLonde, H. Wang, L. Chen, and G. J. Snyder. Convergence of electronic bands for high performance bulk thermoelectrics. *Nature*, **473**, 66, (2011).

[10] Y. Tang, Z. M. Gibbs, G. Li, H. S. Kim, M. B. Nardelli, S. Curtarolo, and G. J. Snyder. Convergence of multi-valley bands as the electronic origin of high thermoelectric performance in CoSb3 skutterudites. *Nature Materials*, **14**, 1223, (2015).

[11] S. Lin, Z. Chen, J. Shen, Ge. B, and Y. Pei. Tellurium as a high-performance elemental thermoelectric. *Nature Communications*, **7**, 10287, (2016).

[12] W. Chen, J. Pohls, G. Hautier, D. Broberg, S. Bajaj, U. Aydemir, Z. M. Gibbs, H. Zhu, M. Asta, G. J. Synder, B. Meredig, M. A. White, K. Persson, and A. Jain. Understanding thermoelectric properties from high-throughput calculations: Trends, insights, and comparisons with experiment. *Journal of Materials Chemistry C*, **4**, 4414, (2016).

[13] Q. Song, T.-H Liu, J. Zhou, Z. Ding, and G. Chen. Ab initio study of electron mean free paths and thermoelectric properties of lead telluride. *Materials Today Physics*, **2**, 69, (2017).

[14] T. J. Scheidemantel, C. Ambrosch-Draxl, T. Thonhauser, J.V. Badding, and J.O. Sofo. Transport coefficients from first-principles calculations. *Physical Review B*, **68**, 125210, (2003).

[15] G. Xing, J. Sun, Y. Li, X. Fan, W. Zheng, and D. J. Singh. Thermoelectric properties of p-type cubic and rhombohedral GeTe. *Journal of Applied Physics*, **123**, 195105, (2018).

[16] F. Zahid and R. Lake. Thermoelectric properties of Bi2Te3 atomic quintuple thin films. *Applied Physics Letters*, **97**, 212102, (2010).

[17] J. Maassen and M. Lundstrom. A computational study of the thermoelectric performance of ultrathin Bi2Te3 films. *Applied Physics Letters*, **102**, 093103, (2013).

[18] N. T. Hung, A. R. T. Nugraha, and R. Saito. Two-dimensional InSe as a potential thermoelectric material. *Applied Physics Letters*, **111**, 092107, (2017).

[19] J. Zhou, H. Zhu, T.-H. Lui, Q. Song, and et. al. Large thermoelectric power factor from crystal symmetry-protected non-bonding orbital in half-heuslers. *Nature Communications*, **9**, 1721, (2018).

[20] J. Ma, Y. Chen, and W. Li. Intrinsic phonon-limited charge carrier mobilities in thermoelectric SnSe. *Physical Review B*, **97**, 205207, (2018).

[21] J. Park, Y. Xia, and V. Ozolins. First-principles assessment of thermoelectric properties of CuFeS2. *Journal of Applied Physics*, **11**, 014058, (2019).

[22] V. Askarpour and J. Maassen. Unusual thermoelectric transport anisotropy in quasi-two-dimensional rhombohedral GeTe. *Physical Review B*, **100**, 075201, (2019).

[23] F. Giustino, M. L. Cohen, and S. G. Louie. Electron-phonon interaction using Wannier functions. *Physical Review B*, **76**, 165108, (2007).

[24] B. Qiu, Z. Tian, A. Vallabhaneni, B. Liao, J. M. Mendoza, O. D. Restrepo, X. Ruan, and G. Chen. First-principles simulation of electron mean-free-path spectra and thermoelectric properties in silicon. *European Physics Letters*, **109**, 57006, (2015).

[25] S. Ponce, E. R. Margine, C. Verdi, and F. Giustino. EPW: Electron-phonon coupling, transport and superconducting properties using maximally localized Wannier functions. *Computer Physics Communications*, **209**, 116-133, (2016).

[26]

[27] Evan Witkoske, Xufeng Wang, Mark S. Lundstromg, Vahid Askarpour, and Jesse Maassen. Thermoelectric band engineering: The role of carrier scattering. *Journal of Applied Physics*, **122**, 175102, (2017).

[28] Xufeng Wang, Vahid Askarpour, Jesse Maassen, and Mark S. Lundstrom. On the calculation of Lorenz numbers for complex thermoelectric materials. *Journal of Applied Physics*, **123**, 055104, (2018).

[29] J. Zhou, R. Yang, G. Chen, and M. S. Dresselhaus. Optimal bandwidth for high efficiency thermoelectrics. *Physical Review Letters*, **107** ,226601 , (2011).

[30] F. Bloch. Uber die Quantenmechanik der Elektronen in Kristallgittern. *Physik*, **52**, 555, (1928).

[31] Steven H. Simon. *The Oxford Solid State Basics*. Oxford, 2013.

[32] Jeong Changwook, Raseong Kim, Mathieu Luisier, Supriyo Datta, and Mark S. Lundstrom. On Landauer versus Boltzmann and full band versus effective mass evaluation of thermoelectric transport coefficients. *Journal of Applied Physics*, **107**, 023707, (2010).

[33] Jeong Changwook, Raseong Kim, and Mark S. Lundstrom. On the best bandstructure for thermoelectric performance: A Landauer perspective. *Journal of Applied Physics*, **111**, 113707, (2012).

[34] Mark Lundstrom. *Fundamentals of carrier transport*. Cambridge University Press, 2000.

[35] Pierre Hohenberg and Walter Kohn. Inhomogeneous electron gas. *Physical Review*, **136**, 3B, (1964).

[36] Walter Kohn and Lu Jeu Sham. Self-consistent equations including exchange and correlation effects. *Physical Review*, **1340**, 4A, (1965).

[37] Peter E. Blöchl, Ove Jepsen, and Ole Krogh Andersen. Improved tetrahedron method for Brillouin-zone integrations. *Physical Review B*, **49**, 23, (1994).

[38] Xufeng Wang, Evan Witkoske, Jesse Maassen, and Mark Lundstrom. LanTraP: A code for calculating thermoelectric transport properties with the Landauer formalism. *arXiv e-prints*, Jun 2018.

[39] Raseong Kim, Supriyo Datta, and Mark S. Lundstrom. Influence of dimensionality on thermoelectric device performance. *Journal of Applied Physics*, **105**, 034506, (2009).

[40] M. Markov, X. Hu, H.-C. Liu, N. Liu, S. J Poon, K. Esfarjani, and M. Zebarjadi. Semi-metals as potential thermoelectric materials: Case of HgTe. *Scientific Reports*, **8**, 9876, (2018).

[41] J. Maassen, C. Jeong, A. Baraskar, M. Rodwell, and M. Lundstrom. Full band calculations of the intrinsic lower limit of contact resistivity. *Applied Physics Letters*, **102**, 111605, (2013).

[42] Darshana Wickramaratne, Ferdows Zahid, and Roger K Lake. Electronic and thermoelectric properties of van der Waals materials with ring-shaped valence bands. *Journal of Applied Physics*, **118**, 075101, (2015).

[43] H. Sevincli. Quartic dispersion, strong singularity, magnetic instability, and unique thermoelectric properties in two-dimensional hexagonal lattices of group-VA elements. *Nano Letters*, **17**, 4 , (2017).

[44] P. Das, D. Wickramaratne, B. Debnath, G. Yin, and R. K. Lake. Charged impurity scattering in two-dimensional materials with ring-shaped valence bands: GaS, GaSe, InS, and InSe. *Physical Review B*, **99**, 085409, (2019).

[45] Joseph P. Heremans, Robert J. Cava, and Nitin Samarth. Tetradymites as thermoelectrics and topological insulators. *Nature Reviews: Materials*, **2**, 17049, (2017).

[46] O. V. Yazyev, J. E. Moore, and S. G. Louie. Spin polarization and transport of surface states in the topological insulators Bi2Se3 and Bi2Te3 from first principles. *Physical Review Letters*, **105**, 266806, (2010).

[47] B. Poudel, Q. Hao, Y. Ma, T. Lan, A. Minnich, B. Yu, Y. Xiao, D. Wang, A. Muto, D. Vashaee, X. Chen, J. Liu, M. S. Dresselhaus, G. Chen, and Ren Z. High-thermoelectric performance of nanostructured bismuth antimony telluride bulk alloys. *Science*, **320**, 634, (2008).

[48] O. Hellman and D. A. Broido. Phonon thermal transport in Bi2Te3 from first principles. *Physical Review B*, **90**, 134309, (2014).

[49] H. J. Goldsmid. The thermal conductivity of bismuth telluride. *Proceedings Physics Society*, **69**, 203, (1958).

[50] H. J. Goldsmid, A. R. Sheard, and D. A. Wright. The performance of bismuth telluride thermojunctions. *British Journal of Applied Physics*, **9**, 365, (1958).

[51] W. Kim, J. Zide, A. Gossard, D. Klenov, S. Stemmer, A. Shakouri, and A. Majumdar. Thermal conductivity reduction and thermoelectric figure of merit increase by embedding nanoparticles in crystalline semiconductors. *Physical Review Letters*, **96**, 045901, (2006).

[52] A. I. Hochbaum, R. Chen, R. D. Delgado, W. Liang, E. C. Garnett, M. Najarian, A. Majumdar, and P. Yang. Enhanced thermoelectric performance of rough silicon nanowires. *Nature*, **451**, 163, (2008).

[53] V. Goyal, D. Teweldebrhan, and A. A. Balandin. Mechanically-exfoliated stacks of thin films of topological insulators with enhanced thermoelectric performance. *Applied Physics Letters*, **97**, 133117, (2010).

[54] C.-Z. Chang C.-L. Song L.-L. Wang X. Chen J.-F. Jia Z. Fang X. Dai W.-Y. Shan S.-Q. Shen Q. Niu X.-L. Qi S.-C. Zhang X.-C. Ma Y. Zhang, K. He and Q.-K. Xue. Crossover of the three-dimensional topological insulator Bi2Se3 to the two-dimensional limit. *Nature Physics Letters*, **6**, 584, (2010).

[55] C.-X. Liu, H. Zhang, B. Yan, X.-L. Qi, T. Frauenheim, X. Dai, Z. Fang, and S.-C. Zhang. Oscillatory crossover from two-dimensional to three-dimensional topological insulators. *Physical Review B*, **81**, 041307(R), (2010).

[56] K. S. Novoselov, A. Mishchenko, A. Carvalho, and Castro Neto A. H. 2D materials and van der Waals heterostructures. *Science*, **353**, 6298, (2016).

[57] D. Teweldebrhan, V. Goyal, M. Rahman, and A. A. Balandin. Atomically-thin crystalline films and ribbons of bismuth telluride. *Applied Physics Letters*, **96**, 053107, (2010).

[58] D. Teweldebrhan, V. Goyal, and A. A. Balandin. Exfoliation and characterization of bismuth telluride atomic quintuples and quasi-two-dimensional crystals. *Nano Letters*, **10**, 1209, (2010).

[59] C. I. Fornari, P. H. O. Rappl, S. L. Morelhao, and E. Abramof. Structural properties of Bi2Te3 topological insulator thin films grown by molecular beam epitaxy on (111) BaF2 substrates. *Journal of Applied Physics*, **119**, 165303, (2016).

[60] S. L. Morelhao, C. I. Fornari, P. O. Rappl, and E. Abramof. Nanoscale characterization of bismuth telluride epitaxial layers by advanced X-ray analysis. *Journal of Applied Crystallography*, **5**, 2, (2017).

[61] Darshana Wickramaratne, Ferdows Zahid, and Roger K Lake. Electronic and thermoelectric properties of few-layer transition metal dichalcogenides. *The Journal of Chemical Physics*, **140**, 124710, (2014).

[62] Paolo Giannozzi, Stefano Baroni, Nicola Bonini, Matteo Calandra, Roberto Car, Carlo Cavazzoni, Davide Ceresoli, Guido L Chiarotti, Matteo Cococcioni, Ismaila Dabo, et al. Quantum Espresso: A modular and open-source software project for quantum simulations of materials. *Journal of Physics: Condensed Matter*, **21**, 395502, (2009).

[63] Peter E Blöchl. Projector augmented-wave method. *Physical Review B*, **50**, 24, (1994).

[64] J. P. Perdew, K. Burke, and M. Ernzerhof. Generalized gradient approximation made simple. *Physical Review Letters*, **77**, 3865, (1996).

[65] S. Grimme. Semiempirical GGA-type density functional constructed with a long-range dispersion correction. *Jounal of Computational Chemistry*, **27**, 1787, (2006).

[66] H. J. Monkhorst and J. D. Pack. Special points for Brillouin-zone integrations. *Physical Review B*, **13**, 5188, (1976).

[67] T. Forster, P. Kruger, and M. Rohlfing. Two-dimensional topological phases and electronic spectrum of Bi2Se3 thin films from GW calculations. *Physical Review B*, **92**, 201404(R), (2015).

[68] T. Forster, P. Kruger, and M. Rohlfing. GW calculations for Bi2Te3 and Sb2Te3 thin films: Electronic and topological properties. *Physical Review B*, **93**, 205442, (2016).

[69] T. J. Seebeck. Thermal transport in bismuth telluride quintuple layer: Mode-resolved phonon properties and substrate effects. *Nature Scientific Reports*, **6**, 27492, (2016).

Appendix A

The Band Counting Algorithm

Distribution-of-modes: One Dimension

We denote the dispersion of a single electronic band in a crystalline material as $\epsilon(\vec{k_x})$. The distribution of modes for this band (which is assumed to be spin-degenerate) is defined as:

$$M(E) = \frac{h}{2L} \sum_{k_x} |v_x(\vec{k})| \delta(E - \epsilon(k_x)), \tag{A.1}$$

where $v_x(k) = \frac{1}{\hbar} \frac{\partial \epsilon}{\partial k_x}$ is the group velocity along the transport direction.

In materials with reflection symmetry (which is most of them), each electronic state has a corresponding state with the opposite velocity. This allows us to restrict our sum to positive velocity states if we introduce a factor of 2. To be explicit, we define the one-dimensional positive velocity surface, S^+_{1D}, as

$$S^+_{1D}(E) = \{k_x \mid v_x(k_x) > 0\}, \tag{A.2}$$

and we then have that

$$M(E) = \frac{2\pi\hbar}{L} \sum_{k_x \in S^+_{1D}} \frac{1}{\hbar} \frac{\partial \epsilon}{\partial k_x} \delta(E - \epsilon(k_x)). \tag{A.3}$$

In solid-state materials with a macroscopic number of atoms, the k-points are so dense that the sum over them can be replaced by an integral, via the canonical substitution $\sum_k \rightarrow \frac{L}{2\pi} \int_{-\infty}^{\infty} dk$, where L is the length of the material along the x direction. Making this substitution converts Equation 3 to the following:

$$M(E) = \int_{S^+} \frac{\partial \epsilon}{\partial k_x} \delta(E - \epsilon(k_x)) dk_x \tag{A.4}$$

Note that S^+ is in general not a single continuous domain, but rather the union of multiple continous subspaces of the Brillouin zone. In other words, there may

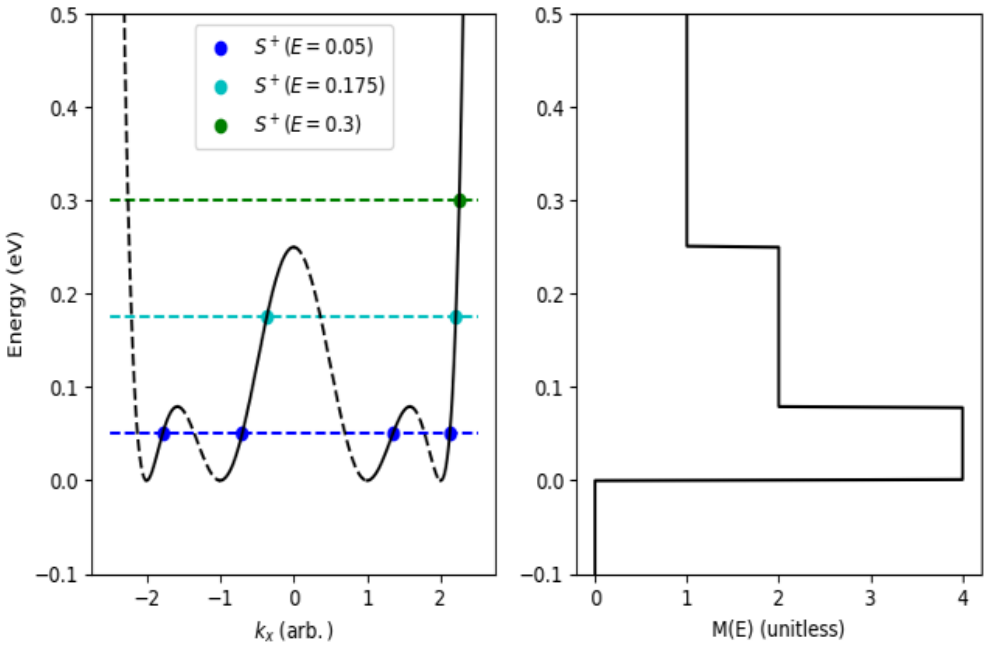

Figure A.1: Illustration of the Landauer band-counting algorithm for a 1D bandstructure. Positive velocity branches are plotted as solid lines, negative velocity brances as dotted lines

be multiple disjoint segments of the 1D band structure that correspond to positive velocity states.

Next, we apply the following delta function identity

$$\int_{-\infty}^{\infty} f(x)\delta(g(x))dx = \sum_{x_0 \in S} \frac{f(x_0)}{|g'(x_0)|}, \tag{A.5}$$

where S is the set of all points x_0 such that $g(x_0) = 0$. In light of this, we define the "crossing set": $S^+_{1D}(E) = \{k_x \in S^+ \mid \epsilon(k_x) = E\}$. This allows us to rewrite Equation 4 in the following manner,:

$$M(E) = \int_{S^+} \frac{\partial \epsilon}{\partial k_x} \delta(E - \epsilon(k_x))dk_x = \sum_{k_0 \in S^+_{1D}(E)} \frac{\frac{\partial \epsilon}{\partial k_x}(k_0)}{|-\frac{\partial \epsilon}{\partial k_x}(k_0)|} = 1 + \cdots + 1 = \dim(S^+_{1D}(E)). \tag{A.6}$$

Thus, we have shown that $M(E)$ for a 1D band is equal to the number of positive velocity states with energy E. This is represented graphically in Figure 1.

Distribution-of-modes: Two Dimensions

For a two-dimensional material, the electronic dispersion is now a function of two variables, *i.e.* $\epsilon = \epsilon(k_x, k_y)$. The two-dimensional distribution-of-modes is then given by

$$M_{2D}(E) = \frac{h}{2A} \sum_{k_x} \sum_{k_y} |v_x(k_x, k_y)| \delta(E - \epsilon(k_x, k_y)). \tag{A.7}$$

The basic idea is to apply our 1D result to each 1D slice of the 2D bandstructure. To do this, we define positive velocity surfaces analogous to those defined in the 1D case, with the caveat that they are now also functions of k_y.

$$S^+_{2D}(k_y) = \{k_x \mid v_x(k_x, k_y) > 0\}, \tag{A.8}$$

$$S^+_{2D}(k_y, E) = \{k_x \in S^+_{2D} \mid \epsilon(k_x, k_y) = E\}, \tag{A.9}$$

In terms of the first set, we have that

$$M_{2D}(E) = \frac{1}{L} \sum_{k_y} \int_{S^+} \delta(E - \epsilon(k_x, k_y)) \frac{\partial \epsilon}{\partial k_x} dk_x \tag{A.10}$$

With this definition, our expression for the 2D distribution of modes is simply

$$M_{2D}(E) = \frac{1}{L} \sum_{k_y} \dim(S^+_{2D}(k_y, E)), \tag{A.11}$$

Distribution-of-modes: Three Dimensions

It is straightforward to see how this generalizes to the three-dimensional case.

$$S^+_{3D}(k_y, k_z) = \{k_x \mid v_x(k_x, k_y, k_z) > 0\}, \tag{A.12}$$

$$S^+_{3D}(k_y, k_z, E) = \{k_x \in S^+_{3D}(k_y, k_z) \mid \epsilon(k_x, k_y, k_z) = E\}. \tag{A.13}$$

$$M_{3D}(E) = \frac{1}{A} \sum_{k_y} \sum_{k_z} \dim(S^+_{3D}(k_y, k_z, E)), \tag{A.14}$$

Calculating V_λ

The average velocity quantity $V_\lambda(E)$ can be calculated using essentially the same band-counting procedure as for $M(E)$, with the added detail that one must also calculate the quantity v_x at each band crossing, rather than just count the number of crossings. The average velocity $V_\lambda(E)$ is defined as

$$V_\lambda(E) = 2\frac{\langle v_x^2(\vec{k})\rangle}{\langle|v_x(\vec{k})|\rangle} = 2\frac{\sum_{\vec{k}} v_x^2(\vec{k})\delta(E-\epsilon(\vec{k}))}{\sum_{\vec{k}}|v_x(\vec{k})|\delta(E-\epsilon(\vec{k}))} \tag{A.15}$$

Using the same sum-to-integral trick from the previous section, and assuming a 3D material, we can rewrite this as

$$\begin{aligned} V_\lambda(E) &= 2\frac{\sum_{k_y}\sum_{k_z}\int v_x^2(k_x,k_y,k_z)\delta(E-\epsilon(k_x,k_y,k_z))dk_x}{\sum_{k_y}\sum_{k_z}\int|v_x(k_x,k_y,k_z)|\delta(E-\epsilon(k_x,k_y,k_z))dk_x} \\ &= 2\frac{\sum_{k_y}\sum_{k_z}\{\sum_{k_0\in S_{3D}^+(E,k_y,k_z)}|v_x(k_0,k_y,k_z)|\}}{\sum_{k_y}\sum_{k_z}\dim(S_{3D}^+(E,k_y,k_z))}, \end{aligned}$$

an expression which allows for an numerical implementation nearly as efficient that of simple band-counting.

Appendix B

Fixing Multiple Scattering Constants

In materials with large band gaps, or when considering systems at very low temperatures, the single band model is often sufficient to describe experiments because the states further from the Fermi level (*e.g.* the conduction states in a p-doped semicondutor) recieve essentially no weighting from the Fermi window function. However, when bipolar effects become significant, *i.e.* when k_BT is on the order of the band gap, E_g, one must consider both valence and conduction states in order to accurately model transport. As in principle there is no reason to expect the scattering constants for the valence and conduction states to have identical values, we must consider the possibilty of having *two* different scattering constants: one for the valence states, and one for the conduction states. This appendix outlines a method for determining the appropriate value for these constants from experimental measurements.

Suppose that we have have used DFT to obtain the electronic dispersion of a semiconducting material, and have calculated the corresponding *unscaled* transport distribution $T(E)$. For example, if we were implementing a DOS scattering approximation, we would have that $T(E) = \frac{2}{h}M(E)V_\lambda(E)\frac{1}{D(E)}$ (note the lack of the usual scattering constant K_0). We denote the values of the valence band maximum and conduction band minimum obtained by DFT as E_V and E_c respectively. In terms of these energy values and our unscaled transport distribution $T(E)$, we define the following sub-distributions:

$$T_v(E) = \begin{cases} T(E + E_v), & E \leq 0 \\ 0, & E > 0 \end{cases} \tag{B.1}$$

$$T_c(E) = \begin{cases} T(E + E_c), & E \geq 0 \\ 0, & E < 0, \end{cases} \tag{B.2}$$

We do the same for the distribution-of-modes, $M(E)$.

$$M_v(E) = \begin{cases} M(E + E_v), & E \leq 0 \\ 0, & E > 0 \end{cases} \tag{B.3}$$

$$M_c(E) = \begin{cases} M(E + E_c), & E \geq 0 \\ 0, & E < 0 \end{cases} \tag{B.4}$$

In terms of these functions, after applying the scissor operator to set the VBM to 0 and the CBM to E_g, the true (*i.e.* properly scaled) transport distribution will be given by

$$\begin{aligned} \Sigma(E) &= K_v T_v(E) + K_c T_c(E - E_g) \\ &= K_v \frac{2}{h} M_v(E) \lambda_v(E) + K_c \frac{2}{h} M_c(E - E_g) \lambda_c(E - E_g) \end{aligned}$$

where K_v and K_c are the scattering constants yet to be determined.

To facilitate our discussion, we introduce two pieces of notation. We define the expression $\langle f \rangle$ as

$$\langle f \rangle = \int f(E) \left(-\frac{\partial f_0}{\partial E} \right) dE, \tag{B.5}$$

wheras the double-angle bracketed expression $\langle\langle f \rangle\rangle$ is taken to mean

$$\langle\langle f \rangle\rangle = \frac{\int f(E) M(E) \left(-\frac{\partial f_0}{\partial E} \right) dE}{\int M(E) \left(-\frac{\partial f_0}{\partial E} \right) dE} = \frac{\langle f M \rangle}{\langle M \rangle}. \tag{B.6}$$

The latter definition is commonly used to define the 'average value' of quantities like $\lambda(E)$ in the Landauer formalism, as it effectively weights the contribution of each energy level by the extent to which it contributes to transport.

As a first step we calculate the thermoelectic electric moment integrals $I_{0,v}$ and $I_{0,c}$,

$$I_{0,v} = \frac{h}{2} \int_{-\infty}^{\infty} T_v(E) \left(-\frac{\partial f_0}{\partial E} \right) dE = \langle M_v \lambda_v \rangle , \tag{B.7}$$

$$I_{0,c} = \frac{h}{2}\int_{-\infty}^{\infty} T_c(E)\left(-\frac{\partial f_0}{\partial E}\right)dE = \langle M_c\lambda_c\rangle\,, \tag{B.8}$$

as well as the functions $\langle M_v\rangle$ and $\langle M_c\rangle$, resolving them as functions of Fermi level μ. Now we are in a position to consider our experimental data. Suppose that experiments had shown our material to have a gap E_g, and that the average MFP for electrons when the Fermi level was at the valence band edge was $\langle\langle\lambda\rangle\rangle_{\mu=E_v} = \lambda_1$. We then have that

$$\begin{aligned}\lambda_1 &= K_v\frac{\langle M_v\lambda_v\rangle_{\mu=0}}{\langle M_v\rangle_{\mu=0}+\langle M_c\rangle_{\mu=-E_g}} + K_c\frac{\langle M_c\lambda_c\rangle_{\mu=-E_g}}{\langle M_v\rangle_{\mu=-E_g}+\langle M_c\rangle_{\mu=0}}\\ &= AK_v + BK_c\end{aligned}$$

Similarily, if for the conduction band states we have that $\langle\langle\lambda\rangle\rangle_{\mu=E_c} = \lambda_2$, then

$$\begin{aligned}\lambda_2 &= K_v\frac{\langle M_v\lambda_v\rangle_{\mu=E_g}}{\langle M_v\rangle_{\mu=E_g}+\langle M_c\rangle_{\mu=0}} + K_c\frac{\langle M_c\lambda_c\rangle_{\mu=0}}{\langle M_v\rangle_{\mu=E_g}+\langle M_c\rangle_{\mu=0}}\\ &= CK_v + DK_c\end{aligned}$$

This can be written as a matrix equation thusly

$$\begin{bmatrix}\lambda_1\\ \lambda_2\end{bmatrix} = \begin{bmatrix}A & B\\ C & D\end{bmatrix}\begin{bmatrix}K_v\\ K_c\end{bmatrix} \tag{B.9}$$

allowing for K_v and K_c to be calculated by solving a simple linear system. Note that the matrix elements need only be recalculated when the band gap is changed.

Appendix C

Octic Band Dispersion Model

In order to investigate the consequences of a band structure possessing a critical surface at energies other than the band-edge, we introduce a new isotropic simple model of electronic dispersion

$$\epsilon(k) = \frac{\epsilon_0}{a^4 b^4}(k^2 - a^2)^2(k^2 - b^2)^2, \tag{C.1}$$

This definition results in two critical constant energy surfaces at the band-edge, and a third critical constant energy surface at $E = \frac{(b^2-a^2)^2}{16a^2b^2}\epsilon_0$.

The first step when calculating energy-resolved quantities from an analytic model of electronic dispersion is to identify the constant energy surfaces as a function of E, *i.e.* to solve for k in the equation $\epsilon(k) = E$. For any 2D isotropic dispersion model, the constant energy surfaces are circles in reciprocal space. As shown in Figure C.1, there are as many as four such circles for our octic band model, and their radii are given by the following formulae:

$$k_1(E) = \frac{1}{\sqrt{2}}\sqrt{a^2 + b^2 - \sqrt{(b^2 - a^2)^2 + 4a^2b^2\sqrt{\frac{E}{\epsilon_0}}}} \tag{C.2}$$

$$k_2(E) = \frac{1}{\sqrt{2}}\sqrt{a^2 + b^2 - \sqrt{(b^2 - a^2)^2 - 4a^2b^2\sqrt{\frac{E}{\epsilon_0}}}} \tag{C.3}$$

$$k_3(E) = \frac{1}{\sqrt{2}}\sqrt{a^2 + b^2 + \sqrt{(b^2 - a^2)^2 - 4a^2b^2\sqrt{\frac{E}{\epsilon_0}}}} \tag{C.4}$$

$$k_4(E) = \frac{1}{\sqrt{2}}\sqrt{a^2 + b^2 + \sqrt{(b^2 - a^2)^2 + 4a^2b^2\sqrt{\frac{E}{\epsilon_0}}}} \tag{C.5}$$

While $k_4(E)$ is defined for all $E > 0$, the $k_1(E)$ branch only exists when $E < \epsilon_0$, and $k_2(E)$ and $k_3(E)$ are only defined when $E < \frac{(b^2-a^2)^2}{16a^2b^2}\epsilon_0$.

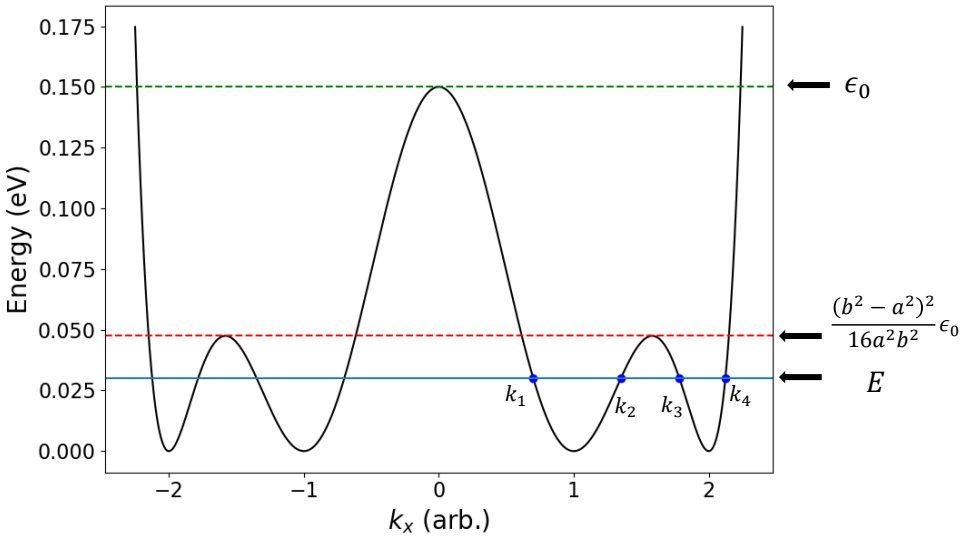

Figure C.1: Plot of a 1D slice of the 2D octic band dispersion model. In this plot, we have chosen the as parameter values $a = 1$, $b = 2$ and $\epsilon_0 = 0.15$ eV.

The radial velocity is given by

$$v(k) = \frac{1}{\hbar}\frac{\partial \epsilon}{\partial k} = \frac{4\epsilon_0}{a^4 b^4 \hbar} k(k^2 - a^2)(k^2 - b^2)(2k^2 - a^2 - b^2) \tag{C.6}$$

Using the standard circular parameterization, with the radius of the $n{-}th$ constant energy surface equal to $k_n(E)$, our Q-functions become

$$Q_1(E) = Q_4(E) = \frac{a^2 b^2}{16\pi^2\sqrt{\epsilon_0 E}} \frac{1}{\sqrt{(b^2 - a^2)^2 + 4a^2 b^2 \sqrt{\frac{E}{\epsilon_0}}}} \tag{C.7}$$

$$Q_2(E) = Q_3(E) = \frac{a^2 b^2}{16\pi^2\sqrt{\epsilon_0 E}} \frac{1}{\sqrt{(b^2 - a^2)^2 - 4a^2 b^2 \sqrt{\frac{E}{\epsilon_0}}}} \tag{C.8}$$

The absence of any ϕ-dependence is a consequence of the isotropicity of the electronic dispersion. Now, using the formulas provided in Chapter 2, one can evaluate the integrals needed to obtain explicit expressions for the three quantities of interest.

$$D(E) = \begin{cases} \frac{4}{\pi\sqrt{\epsilon_0 E}}\left(\frac{1}{\sqrt{(b^2-a^2)^2+4a^2b^2\sqrt{\frac{E}{\epsilon_0}}}} + \frac{1}{\sqrt{(b^2-a^2)^2-4a^2b^2\sqrt{\frac{E}{\epsilon_0}}}}\right), & 0 < E \leq \frac{(a^2-b^2)^4}{16a^4b^4}\epsilon_0 \\ \frac{4}{\pi\sqrt{\epsilon_0 E}}\left(\frac{1}{\sqrt{(b^2-a^2)^2+4a^2b^2\sqrt{\frac{E}{\epsilon_0}}}}\right), & \frac{(a^2-b^2)^4}{16a^4b^4}\epsilon_0 < E \leq \epsilon_0 \\ \frac{2}{\pi\sqrt{\epsilon_0 E}}\left(\frac{1}{\sqrt{(b^2-a^2)^2+4a^2b\sqrt{\frac{E}{\epsilon_0}}}}\right), & \epsilon_0 < E \end{cases}$$

$$M(E) = \begin{cases} \frac{1}{\pi\sqrt{2}}\left(\sqrt{a^2+b^2-\sqrt{(b^2-a^2)^2+4a^2b\sqrt{\frac{E}{\epsilon_0}}}} + \sqrt{a^2+b^2-\sqrt{(b^2-a^2)^2-4a^2b\sqrt{\frac{E}{\epsilon_0}}}} + \right. \\ \qquad \left. \sqrt{a^2+b^2+\sqrt{(b^2-a^2)^2-4a^2b\sqrt{\frac{E}{\epsilon_0}}}} + \sqrt{a^2+b^2+\sqrt{(b^2-a^2)^2+4a^2b\sqrt{\frac{E}{\epsilon_0}}}}\right), \\ \frac{1}{\pi\sqrt{2}}\left(\sqrt{a^2+b^2-\sqrt{(b^2-a^2)^2+4a^2b\sqrt{\frac{E}{\epsilon_0}}}} + \sqrt{a^2+b^2+\sqrt{(b^2-a^2)^2+4a^2b\sqrt{\frac{E}{\epsilon_0}}}}\right), \\ \frac{1}{\pi\sqrt{2}}\sqrt{a^2+b^2+\sqrt{(b^2-a^2)^2+4a^2b^2\sqrt{\frac{E}{\epsilon_0}}}} \end{cases}$$

$$V(E) = \begin{cases} \frac{5\sqrt{\epsilon_0 E}}{2\hbar M(E)}\sqrt{(b^2-a^2)^2+4a^2b^2\sqrt{\frac{E}{\epsilon_0}}} + \sqrt{(b^2-a^2)^2-4a^2b^2\sqrt{\frac{E}{\epsilon_0}}}, \\ \frac{5\pi\sqrt{\epsilon_0 E}}{\hbar\sqrt{2}}\frac{\sqrt{(b^2-a^2)^2+4a^2b^2\sqrt{\frac{E}{\epsilon_0}}}}{\sqrt{a^2+b^2-\sqrt{(b^2-a^2)^2+4a^2b^2\sqrt{\frac{E}{\epsilon_0}}}}+\sqrt{a^2+b^2-\sqrt{(b^2-a^2)^2+4a^2b^2\sqrt{\frac{E}{\epsilon_0}}}}}, \\ \frac{\pi\sqrt{\epsilon_0 E}}{\hbar 2\sqrt{2}}\sqrt{(b^2-a^2)^2+4a^2b^2\sqrt{\frac{E}{\epsilon_0}}}\sqrt{a^2+b^2+\sqrt{(b^2-a^2)^2+4a^2b^2\sqrt{\frac{E}{\epsilon_0}}}} \end{cases}$$

Appendix D

Explicit Transport Direction Dependence in Ellipsoidal Bands

In this appendix, we apply our surface integral formulation to the problem of calculating $M(E)$ for an arbitrarily oriented ellipsoidal band. We begin by providing the 3D analogues of the 2D expressions provided in Chapter 2. In three-dimensional materials, the constant energy surfaces are two-dimensional, requiring the use of two parameters, and three smooth functions thereof to describe them parametrically.

$$\begin{cases} k_x = x(\phi, \theta) \\ k_y = y(\phi, \theta) \\ k_z = z(\phi, \theta) \\ \phi \in [a, b] \\ \theta \in [c, d] \end{cases}$$

Let $S(E)$ be the set of all reciprocal lattice points (k_x, k_y, k_z) for which $\epsilon(k_x, k_y, k_z) = E$. Then integrals over $S(E)$ can be rewritten thusly:

$$\int_{S(E)} \frac{f(k_x, k_y, k_z)}{|\nabla \epsilon(k_x, k_y, k_z)|} dS = \int_{\phi=a}^{b} \int_{\theta=c}^{d} \frac{f(x(\phi,\theta), y(\phi,\theta), z(\phi,\theta))}{|\nabla \epsilon(x(\phi,\theta), y(\phi,\theta), z(\phi,\theta))|} |\vec{r}_\theta \times \vec{r}_\phi| d\phi d\theta \tag{D.1}$$

where

$$\vec{r}(\phi, \theta) = \vec{r}(x(\phi,\theta), y(\phi,\theta), z(\phi,\theta)), \tag{D.2}$$

$$\vec{r}_\theta = (\frac{\partial x}{\partial \theta}, \frac{\partial y}{\partial \theta}, \frac{\partial z}{\partial \theta}), \tag{D.3}$$

$$\vec{r}_\phi = (\frac{\partial x}{\partial \phi}, \frac{\partial y}{\partial \phi}, \frac{\partial z}{\partial \phi}). \tag{D.4}$$

Analogously to our two-dimensional case, we define another density function, this time of two parameters:

$$Z(\phi,\theta) = \frac{1}{8\pi^3}\frac{|r_\theta \times r_\phi|}{|\nabla_k \epsilon(x(\phi,\theta).y(\phi,\theta), z(\phi,\theta))|} \tag{D.5}$$

This allows us to rewrite our sums over k-points as follows:

$$\sum_k f(k)\delta(E-\epsilon(k)) = \int_a^b \int_c^d f(x(\phi,\theta), y(\phi,\theta), z(\phi,\theta))Z(\phi,\theta)d\phi d\theta. \tag{D.6}$$

The total density-of-states is then given by

$$D(E) = 2\int_a^b \int_c^d Z(\phi,\theta)d\phi d\theta, \tag{D.7}$$

whereas the distribution-of-modes is given by

$$M(E) = 2\pi\hbar \int_a^b \int_c^d v_x(\phi,\theta)Z(\phi,\theta)d\phi d\theta, \tag{D.8}$$

and the average velocity by

$$\langle v_x^+(E)\rangle = \frac{\int_a^b \int_c^d v_x(\phi,\theta)Z(\phi,\theta)d\phi d\theta}{\int_a^b \int_c^d Z(\phi,\theta)d\phi d\theta}. \tag{D.9}$$

The dispersion relation of a general ellipsoidal band that is aligned with the standard Cartesian axes in reciprocal space is given by

$$E(k_x,k_y,k_z) = \frac{\hbar^2}{2}\left(\frac{k_x^2}{m_x} + \frac{k_y^2}{m_y} + \frac{k_z^2}{m_z}\right), \tag{D.10}$$

where m_i is the effective mass along the i-th Cartesian direction. If the ellipsoidal band was oriented in some other manner, the formula for the energy would take on a more complicated form. However, no matter what orientation is chosen, there will always exist some orthogonal coordinate system within which the dispersion relation can be expressed in the above simple form. We will call this choice of coordinates the *ellipsoidal coordinate frame* $[x_1, x_2, x_3]$, in terms of which we can write:

$$E = \frac{\hbar^2}{2}\left(\frac{x_1^2}{m_1} + \frac{x_2^2}{m_2} + \frac{x_3^2}{m_3},\right). \tag{D.11}$$

We opt to express the unit vectors of our general ellipsoidal coordinate frame in terms of the Euler angles α, β and γ describing the Euler rotations that map the standard Cartesian coordinate axes into our ellipsoidal cooridnate axes. We have that

$$\hat{x_1} = \begin{bmatrix} \cos\alpha\cos\beta\cos\gamma - \sin\alpha\sin\gamma \\ \sin\alpha\cos\beta\cos\gamma + \cos\alpha\sin\gamma \\ -\sin\beta\cos\gamma \end{bmatrix} \tag{D.12}$$

$$\hat{x_2} = \begin{bmatrix} -\sin\alpha\cos\gamma - \cos\alpha\cos\beta\sin\gamma \\ \cos\alpha\cos\gamma - \sin\alpha\cos\beta\sin\gamma \\ \sin\beta\sin\gamma \end{bmatrix} \tag{D.13}$$

$$\hat{x_3} = \begin{bmatrix} \cos\alpha\sin\beta \\ \sin\alpha\sin\beta \\ \cos\beta \end{bmatrix} \tag{D.14}$$

Without loss of generality, we will assume that we are interested in transport along the Cartesian $\hat{x}$ direction. In order to calculate the x-component of the group velocity, we need to express the components of our ellipsoidal coordinate system in terms of the standard Cartesian components. This is done by projecting the Cartesian coordinate vector onto the unit vectors of the ellipsoidal coordinate system.

$$x_1(k_x, k_y, k_z) = (k_x, k_y, k_z) \cdot \hat{x_1} \tag{D.15}$$

$$x_2(k_x, k_y, k_z) = (k_x, k_y, k_z) \cdot \hat{x_2} \tag{D.16}$$

$$x_3(k_x, k_y, k_z) = (k_x, k_y, k_z) \cdot \hat{x_3} \tag{D.17}$$

Using the above definitions, and after some simplification, we obtain the following definition,

$$v_x(\phi, \theta) = \sqrt{\frac{2E}{m_1}}\Big[(A\cos\phi - B\sin\phi)\sin\theta + C\cos\theta\Big], \tag{D.18}$$

where

$$A = \cos\alpha\cos\beta\cos\gamma - \sin\alpha\sin\gamma, \tag{D.19}$$

$$B = \sqrt{\frac{m_1}{m_2}} \left(\sin\alpha\cos\gamma + \sin\gamma\cos\alpha\cos\beta\right), \tag{D.20}$$

and

$$C = \sqrt{\frac{m_1}{m_3}} \sin\beta\cos\alpha. \tag{D.21}$$

We define our surface parametrization as

$$\vec{k}(\phi,\theta) = a\hat{x_1}\cos\phi\sin\theta + b\hat{x_2}\sin\phi\sin\theta + c\hat{x_3}\cos\theta \tag{D.22}$$

To calculate the distribution-of-modes, we first need to identify which region of our parameter space corresponds to positive velocity states. We can identify the boundaries of this region by setting our $v_x(\phi,\theta)$ expression equal to zero, and inverting it to express θ as a function of ϕ. The expression we obtain will be the upper bound of our θ integration, expressed in terms of ϕ. Doing so, we obtain the following relation,

$$\theta_0(\phi) = \tan^{-1}\left(\frac{C}{B\sin\phi - A\cos\phi}\right) = \tan^{-1}\left(\Phi\right), \tag{D.23}$$

However, as our chosen domain for θ is $[0,\pi]$ care must be taken with the arctangent function, which is typically assigned the range $[-\pi/2,\pi/2]$. To account for this, we must break our ϕ integration up into three regions, shifting our θ bound by π where appropriate.

$$\theta_0(\phi) = \begin{cases} tan^{-1}(\Phi) + \pi, & 0 < \phi < tan^{-1}(A/B) \\ tan^{-1}(\Phi), & tan^{-1}(A/B) < \phi < tan^{-1}(A/B) + \pi \\ tan^{-1}(\Phi) + \pi, & tan^{-1}(A/B) + \pi < \phi < 2\pi \end{cases} \tag{D.24}$$

Using the following integral identities,

$$\int_0^{\tan^{-1}(\Phi)} \sin^2\theta d\theta = \frac{1}{2}\tan^{-1}(\Phi) - \frac{\Phi}{2(\Phi^2+1)}, \tag{D.25}$$

$$\int_0^{\tan^{-1}(\Phi)+\pi} \sin^2\theta d\theta = \frac{\pi}{2} + \frac{1}{2}\tan^{-1}(\Phi) - \frac{\Phi}{2(\Phi^2+1)}, \tag{D.26}$$

$$\int_0^{\tan^{-1}(\Phi)+\pi} \sin\theta\cos\theta d\theta = \int_0^{\tan^{-1}(\Phi)} \sin\theta\cos\theta d\theta = \frac{1}{2}\frac{1}{\Phi^2+1}, \tag{D.27}$$

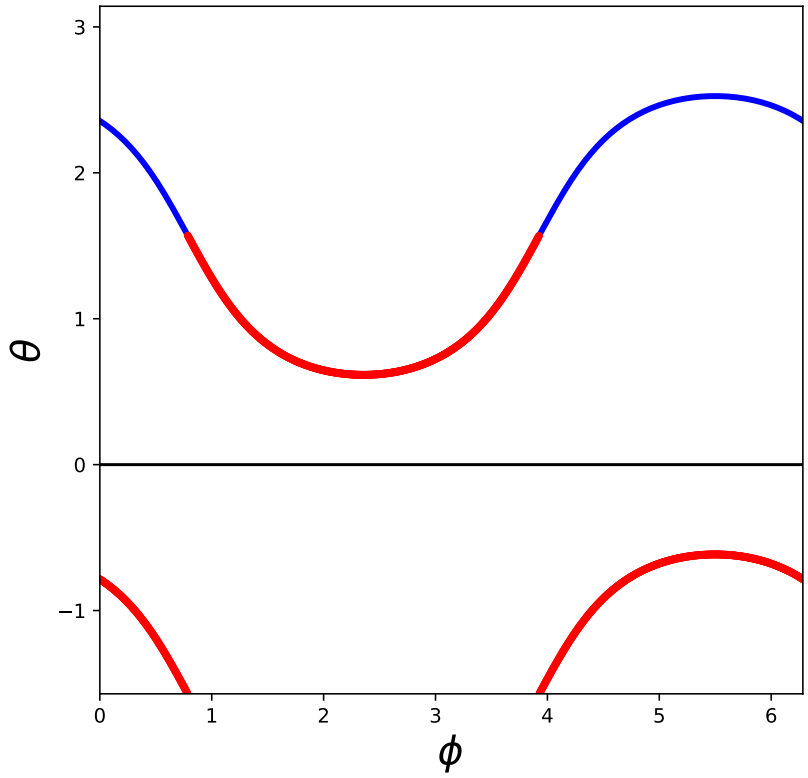

Figure D.1: Sketch of the parameter domain used in calculating the transport-direction resolved distribution-of-modes for a 3D anisotropic parabolic band.

Let M_1 M_2 and M_3 be the contributions to the total distribution-of-modes coming from the first, second and third ϕ regions respectively. We have that

$$\begin{aligned} M_1(E) &= \frac{\sqrt{m_2 m_3}}{2\pi^2\hbar^2} E \int_0^{tan^{-1}(A/B)} (A\cos\phi - B\sin\phi) \int_0^{tan^{-1}\Phi+\pi} \sin^2\theta d\theta \\ &\qquad + C \int_0^{\tan^{-1}\Phi+\pi} \sin\theta\cos\theta d\theta d\phi \\ &= \frac{\sqrt{m_2 m_3}}{2\pi^2\hbar^2} E \int_0^{tan^{-1}(A/B)} (A\cos\phi - B\sin\phi) \left[\frac{\pi}{2} + \frac{1}{2}\tan^{-1}(\Phi) - \frac{\Phi}{2(\Phi^2+1)}\right] \\ &\qquad + C\frac{1}{2(\Phi^2+1)}\, d\phi \end{aligned}$$

$$\begin{aligned} M_2(E) &= \frac{\sqrt{m_2 m_3}}{2\pi^2\hbar^2} E \int_{tan^{-1}(A/B)}^{tan^{-1}(A/B)+\pi} (A\cos\phi - B\sin\phi) \int_0^{tan^{-1}\Phi} \sin^2\theta d\theta \\ &\qquad + C \int_0^{\tan^{-1}\Phi} \sin\theta\cos\theta d\theta d\phi \\ &= \frac{\sqrt{m_2 m_3}}{2\pi^2\hbar^2} E \int_{tan^{-1}(A/B)}^{tan^{-1}(A/B)+\pi} (A\cos\phi - B\sin\phi) \left[\frac{1}{2}\tan^{-1}(\Phi) - \frac{\Phi}{2(\Phi^2+1)}\right] \\ &\qquad + C\frac{1}{2(\Phi^2+1)}\, d\phi \end{aligned}$$

$$\begin{aligned} M_3(E) &= \frac{\sqrt{m_2 m_3}}{2\pi^2\hbar^2} E \int_{tan^{-1}(A/B)+\pi}^{2\pi} (A\cos\phi - B\sin\phi) \int_0^{tan^{-1}\Phi+\pi} \sin^2\theta d\theta \\ &\qquad + C \int_0^{\tan^{-1}\Phi+\pi} \sin\theta\cos\theta d\theta d\phi \\ &= \frac{\sqrt{m_2 m_3}}{2\pi^2\hbar^2} E \int_{tan^{-1}(A/B)+\pi}^{2\pi} (A\cos\phi - B\sin\phi) \left[\frac{\pi}{2} + \frac{1}{2}\tan^{-1}(\Phi) - \frac{\Phi}{2(\Phi^2+1)}\right] \\ &\qquad + C\frac{1}{2(\Phi^2+1)}\, d\phi \end{aligned}$$

Adding these three contributions together, we obtain (after some simplification) the following expression for the total density-of modes.

$$M(E)/\left(\frac{\sqrt{m_2 m_3}}{2\pi^2\hbar^2}E\right) = \frac{1}{2}\int_0^{2\pi} C + (A\cos\phi - B\sin\phi)tan^{-1}\left(\Phi\right)d\phi$$
$$+\frac{\pi}{2}\left[\int_0^{tan^{-1}(A/B)} + \int_{tan^{-1}(A/B)}^{2\pi}\right](A\cos\phi - B\sin\phi)d\phi$$
$$= \pi C + \frac{1}{2}\int_0^{2\pi}(A\cos\phi - B\sin\phi)tan^{-1}\left(\Phi\right)d\phi$$
$$+\frac{\pi}{2}\int_{tan^{-1}(A/B)-\pi}^{tan^{-1}(A/B)}(A\cos\phi - B\sin\phi)d\phi$$

where we have exploited the periodicity of the function $(A\cos\phi - B\sin\phi)$ to shift the integration bounds of the last integral.

We will tackle the two remaining integrals one at a time, making use of the following identity when doing so

$$A\cos\phi - B\sin\phi = \sqrt{A^2+B^2}\cos\left(\phi + \tan^{-1}\left(\frac{B}{A}\right)\right) \tag{D.28}$$

For the first integral, we have that

$$I_1 = \int_0^{2\pi}(A\cos\phi - B\sin\phi)tan^{-1}\left(\Phi\right)d\phi$$
$$= \sqrt{A^2+B^2}\int_0^{2\pi}\cos\left(\phi + \tan^{-1}\left(\frac{B}{A}\right)\right)tan^{-1}\left(\frac{\frac{-C}{\sqrt{A^2+B^2}}}{\cos\left(\phi + \tan^{-1}\left(\frac{B}{A}\right)\right)}\right)d\phi$$

Since this integrand has period π, and we are integrating over an interval of length 2π, we are free to shift the bounds of our integral by any constant amount without changing the value of the integral. In this case, we shift by $\tan^{-1}(B/A)$, obtaining

$$I_1 = -\sqrt{A^2+B^2}\int_0^{2\pi}\cos\phi\ tan^{-1}\left(\frac{\frac{C}{\sqrt{A^2+B^2}}}{\cos\phi}\right)d\phi,$$

where we have exploited the fact that the arctangent function is odd to bring the minus sign outside of the integral. Somewhat surprisingly, this definite integral has a simple solution.

$$I_1 = -2\pi\sqrt{A^2+B^2}\left[1 + \frac{C}{\sqrt{A^2+B^2}} - \sqrt{\frac{C^2}{A^2+B^2}+1}\right]$$
$$= 2\pi\left[\sqrt{A^2+B^2+C^2} - C - \sqrt{A^2+B^2}\right]$$

For the second integral

$$\begin{aligned} I_2 &= \int_{tan^{-1}(A/B)-\pi}^{tan^{-1}(A/B)} (A\cos\phi - B\sin\phi)d\phi \\ &= \sqrt{A^2+B^2}\int_{tan^{-1}(A/B)-\pi}^{tan^{-1}(A/B)} \cos\left(\phi + \tan^{-1}\left(\frac{B}{A}\right)\right)d\phi \\ &= \sqrt{A^2+B^2}\int_{tan^{-1}(A/B)+tan^{-1}(B/A)-\pi}^{tan^{-1}(A/B)+tan^{-1}(B/A)} \cos(\phi)d\phi \\ &= \sqrt{A^2+B^2}\int_{-\pi/2}^{\pi/2} \cos(\phi)d\phi \\ &= 2\sqrt{A^2+B^2} \end{aligned}$$

Putting everything together, we have that

$$\begin{aligned} M(E)/\left(\frac{\sqrt{m_2m_3}}{2\pi^2\hbar^2}E\right) &= \pi C + \pi\left[\sqrt{A^2+B^2+C^2} - C - \sqrt{A^2+B^2}\right] + \pi\sqrt{A^2+B^2} \\ &= \pi\sqrt{A^2+B^2+C^2} \end{aligned}$$

$$\begin{aligned} M(E) &= \frac{\sqrt{m_2m_3}}{2\pi\hbar^2}E\sqrt{A^2+B^2+C^2} \\ &= \frac{\sqrt{m_2m_3}}{2\pi\hbar^2}E\sqrt{\begin{aligned}&(\cos\alpha\cos\beta\cos\gamma - \sin\alpha\sin\gamma)^2 \\ &\quad + \frac{m_1}{m_2}(\sin\alpha\cos\gamma + \sin\gamma\cos\alpha\cos\beta)^2 + \frac{m_1}{m_3}\sin^2\beta\cos^2\alpha\end{aligned}} \end{aligned}$$

Thus, we have derived an expression for the distribution-of-modes along the x-direction for an arbitrarily oriented ellipsoidal band. The formula can be simplified in the special case of spheroidal bands (*i.e.* when two of the effective masses are equal to each other).

Appendix E

Analytic Expressions for Common Electronic Dispersion Models

This appendix provides the full analytic expressions for the quantities of interest that arise from the models of electronic dispersion considered in Chapter 3.

E.1 Anisotropic Parabolic, Effective-Mass Band (3D, 2D, 1D)

For a 1D parabolic band with electronic dispersion given by

$$\epsilon(k_x) = \frac{\hbar^2}{2m_x} k_x^2, \tag{E.1}$$

we have the following definitions:

$$D(E) = \frac{1}{\hbar\pi}\sqrt{\frac{m_x}{2}}\frac{1}{\sqrt{E}} \tag{E.2}$$

$$M(E) = \Theta(E) \tag{E.3}$$

$$\langle v_x^+(E)\rangle = \sqrt{\frac{2E}{m_x}} \tag{E.4}$$

$$\langle v_x^2(E)\rangle = \frac{2E}{m_x} \tag{E.5}$$

$$V_\lambda(E) = 2\frac{\langle v_x^2(E)\rangle}{\langle v_x^+(E)\rangle} = 2\sqrt{\frac{2E}{m_x}} \tag{E.6}$$

For a 2D elliptical band with electronic dispersion given by

$$\epsilon(k_x, k_y) = \frac{\hbar^2}{2}(\frac{k_x^2}{m_x} + \frac{k_y^2}{m_y}), \tag{E.7}$$

we have the following definitions:

$$D(E) = \frac{\sqrt{m_x m_y}}{\pi\hbar^2} \tag{E.8}$$

$$M(E) = \frac{\sqrt{2m_y}}{\pi\hbar}\sqrt{E} \tag{E.9}$$

$$\langle v_x^+(E)\rangle = (\frac{2}{\pi})\sqrt{\frac{2E}{m_x}} \tag{E.10}$$

$$\langle v_x^2(E)\rangle = (\frac{1}{2})\frac{2E}{m_x} \tag{E.11}$$

$$V_\lambda(E) = 2\frac{\langle v_x^2(E)\rangle}{\langle v_x^+(E)\rangle} = (\frac{\pi}{2})\sqrt{\frac{2E}{m_x}} \tag{E.12}$$

For a 3D ellipsoidal band with electronic dispersion given by

$$\epsilon(k_x, k_y, k_z) = \frac{\hbar^2}{2}(\frac{k_x^2}{m_x} + \frac{k_y^2}{m_y} + \frac{k_z^2}{m_z}), \tag{E.13}$$

we have the following definitions:

$$D(E) = \frac{\sqrt{2E}}{\pi^2\hbar^3}\sqrt{m_x m_y m_z} \tag{E.14}$$

$$M(E) = \frac{\sqrt{m_y m_z}}{2\pi\hbar^2}E \tag{E.15}$$

$$\langle v_x^+(E)\rangle = (\frac{1}{2})\sqrt{\frac{2E}{m_x}} \tag{E.16}$$

$$\langle v_x^2(E)\rangle = (\frac{1}{3})\frac{2E}{m_x} \tag{E.17}$$

$$V_\lambda(E) = 2\frac{\langle v_x^2(E)\rangle}{\langle v_x^+(E)\rangle} = (\frac{4}{3})\sqrt{\frac{2E}{m_x}} \tag{E.18}$$

E.2 Kane Bands (3D, 2D, 1D)

For a 1D Kane band with electronic dispersion given by

$$E(1+\alpha E) = \frac{\hbar^2}{2m}k_x^2 \tag{E.19}$$

we have the following definitions:

$$D(E) = \frac{1}{\hbar\pi}\sqrt{\frac{m_x}{2}}\frac{1+2\alpha E}{\sqrt{E(1+\alpha E)}} \tag{E.20}$$

$$M(E) = \Theta(E) \tag{E.21}$$

$$\langle v_x^+(E)\rangle = \sqrt{\frac{2E}{m_x}}\frac{\sqrt{1+\alpha E}}{1+2\alpha E} \tag{E.22}$$

$$\langle v_x^2(E)\rangle = \frac{2E(1+\alpha E)}{m_x(1+2\alpha E)^2} \tag{E.23}$$

$$V_\lambda(E) = 2\frac{\langle v_x^2(E)\rangle}{\langle v_x^+(E)\rangle} = 2\sqrt{\frac{2E}{m_x}}\frac{\sqrt{1+\alpha E}}{1+2\alpha E} \tag{E.24}$$

For a two-dimensional Kane band with electronic dispersion given by

$$E(1+\alpha E) = \frac{\hbar^2}{2m}(k_x^2+k_y^2), \tag{E.25}$$

we have the following definitions:

$$D(E) = \frac{m}{\pi\hbar^2}(1+2\alpha E) \tag{E.26}$$

$$M(E) = \frac{\sqrt{2m}}{\pi\hbar}\sqrt{E(1+\alpha E)} \tag{E.27}$$

$$\langle v_x^+(E)\rangle = (\frac{2}{\pi})\sqrt{\frac{2}{m}}\frac{\sqrt{E(1+\alpha E)}}{1+2\alpha E} \tag{E.28}$$

$$\langle v_x^2(E)\rangle = (\frac{1}{2})\frac{2}{m}\frac{E(1+\alpha E)}{(1+2\alpha E)^2} \tag{E.29}$$

$$V_\lambda(E) = 2\frac{\langle v_x^2(E)\rangle}{\langle v_x^+(E)\rangle} = (\frac{\pi}{2})\sqrt{\frac{2}{m}}\frac{\sqrt{E(1+\alpha E)}}{1+2\alpha E} \tag{E.30}$$

For a three-dimensional Kane band with electronic dispersion given by

$$E(1+\alpha E) = \frac{\hbar^2}{2m}(k_x^2+k_y^2+k_x^2), \tag{E.31}$$

we have the following definitions:

$$D(E) = \frac{\sqrt{2}m^{3/2}}{\pi^2\hbar^3}\sqrt{E(1+\alpha E)}(1+2\alpha E) \tag{E.32}$$

$$M(E) = \frac{m}{2\pi\hbar^2}E(1+\alpha E) \tag{E.33}$$

$$\langle v_x^+(E)\rangle = (\frac{1}{2})\sqrt{\frac{2}{m}}\frac{\sqrt{E(1+\alpha E)}}{1+2\alpha E} \tag{E.34}$$

$$\langle v_x^2(E)\rangle = (\frac{1}{3})\frac{2}{m}\frac{E(1+\alpha E)}{(1+2\alpha E)^2} \tag{E.35}$$

$$V_\lambda(E) = 2\frac{\langle v_x^2(E)\rangle}{\langle v_x^+(E)\rangle} = (\frac{4}{3})\sqrt{\frac{2}{m}}\frac{\sqrt{E(1+\alpha E)}}{1+2\alpha E} \tag{E.36}$$

E.3 Quartic Band (2D)

For a two-dimensional material with electronic dispersion given by

$$\epsilon(k_x, k_y) = \epsilon_0 - \frac{\hbar^2}{2m}(k_x^2 + k_y^2) + \frac{1}{4\epsilon_0}(\frac{\hbar^2}{2m})^2(k_x^2 + k_y^2)^2, \tag{E.37}$$

we have the following definitions:

$$D(E) = \begin{cases} \frac{2m}{\pi\hbar^2}\sqrt{\frac{\epsilon_0}{E}}, & E < \epsilon_0 \\ \frac{m}{\pi\hbar^2}\sqrt{\frac{\epsilon_0}{E}}, & E > \epsilon_0 \end{cases} \tag{E.38}$$

$$M(E) = \begin{cases} \frac{2\sqrt{m\epsilon_0}}{\pi\hbar}\left(\sqrt{1+\sqrt{\frac{E}{\epsilon_0}}} + \sqrt{1-\sqrt{\frac{E}{\epsilon_0}}}\right), & E < \epsilon_0 \\ \frac{2\sqrt{m\epsilon_0}}{\pi\hbar}\sqrt{1+\sqrt{\frac{E}{\epsilon_0}}}, & E > \epsilon_0 \end{cases} \tag{E.39}$$

$$\langle v_x^+(E)\rangle = \begin{cases} \frac{2}{\pi}\sqrt{\frac{E}{m}}\left(\sqrt{1+\sqrt{\frac{E}{\epsilon_0}}} + \sqrt{1-\sqrt{\frac{E}{\epsilon_0}}}\right), & E < \epsilon_0 \\ \frac{4}{\pi}\sqrt{\frac{E}{m}}\sqrt{1+\sqrt{\frac{E}{\epsilon_0}}}, & E > \epsilon_0 \end{cases} \tag{E.40}$$

$$\langle v_x^2(E)\rangle = \begin{cases} 2\frac{E}{m}, & E < \epsilon_0 \\ 2\frac{E}{m}\left(1+\sqrt{\frac{E}{\epsilon_0}}\right), & E > \epsilon_0 \end{cases} \tag{E.41}$$

$$V_\lambda(E) = \begin{cases} 2\pi\sqrt{\frac{E}{m}}\frac{1}{\sqrt{\sqrt{1+\sqrt{\frac{E}{\epsilon_0}}}+\sqrt{1-\sqrt{\frac{E}{\epsilon_0}}}}}, & E < \epsilon_0 \\ \pi\sqrt{\frac{E}{m}}\sqrt{1+\sqrt{\frac{E}{\epsilon_0}}}, & E > \epsilon_0 \end{cases} \tag{E.42}$$

E.4 Rashba Band (2D)

For a two-dimensional material with electronic dispersion given by

$$\epsilon(k_x, k_y) = \epsilon_0 + \frac{\hbar^2}{2m}(k_x^2 + k_y^2) \pm \alpha_R\sqrt{k_x^2 + k_y^2}, \tag{E.43}$$

where

$$\epsilon_0 = \frac{\alpha_R^2 m}{2\hbar^2}, \tag{E.44}$$

we have the following definitions:

$$D(E) = \begin{cases} \frac{m}{\pi\hbar^2}\sqrt{\frac{\epsilon_0}{E}}, & E < \epsilon_0 \\ \frac{m}{\pi\hbar^2}, & E > \epsilon_0 \end{cases} \tag{E.45}$$

$$M(E) = \begin{cases} \frac{\sqrt{2m\epsilon_0}}{\pi\hbar}, & E < \epsilon_0 \\ \frac{\sqrt{2mE}}{\pi\hbar}, & E > \epsilon_0 \end{cases} \tag{E.46}$$

$$\langle v_x^+(E)\rangle = (\frac{2}{\pi})\sqrt{\frac{2E}{m}} \tag{E.47}$$

$$\langle v_x^2(E)\rangle = (\frac{1}{2})\frac{2E}{m} \tag{E.48}$$

$$V_\lambda(E) = (\frac{\pi}{2})\sqrt{\frac{2E}{m}} \tag{E.49}$$